Louisiana State University
LSU Digital Commons

LSU Doctoral Dissertations | Graduate School

2015

The Electronic Structure of Environmentally Persistent Free Radicals Formed on Metal Oxide Surfaces

Chad Allen Thibodeaux
Louisiana State University and Agricultural and Mechanical College, icepilot28@gmail.com

Follow this and additional works at: https://digitalcommons.lsu.edu/gradschool_dissertations

 Part of the Chemistry Commons

Recommended Citation
Thibodeaux, Chad Allen, "The Electronic Structure of Environmentally Persistent Free Radicals Formed on Metal Oxide Surfaces" (2015). *LSU Doctoral Dissertations*. 2151.
https://digitalcommons.lsu.edu/gradschool_dissertations/2151

This Dissertation is brought to you for free and open access by the Graduate School at LSU Digital Commons. It has been accepted for inclusion in LSU Doctoral Dissertations by an authorized graduate school editor of LSU Digital Commons. For more information, please contactgradetd@lsu.edu.

THE ELECTRONIC STRUCTURE OF ENVIRONMENTALLY PERSISTENT FREE RADICALS FORMED ON METAL OXIDE SURFACES

A Dissertation

Submitted to the Graduate Faculty of the
Louisiana State University and
Agricultural and Mechanical College
in partial fulfillment of the
requirements for the degree of
Doctor of Philosophy

in

The Department of Chemistry

by
Chad A. Thibodeaux
B.S., McNeese State University, 2008
August 2015

Acknowledgements

When I graduated from McNeese State University, I had no idea of the adventures ahead. From the highs to the lowest of lows, if I did not have the constant encouragement of so many people I don't think I would have made it through. With that in mind here are a few people I would like to thank that have certainly made me into who I am today and whose friendship I hope will last a lifetime.

Erwin Poliakoff and Phillip Sprunger are some of best mentors anyone could ask for. Physical chemistry can certainly make you want to pull your hair out. However, these two have made it possible to leave LSU with my hair intact (mostly). My other committee member Randy Hall has also given me valuable feed back and expanded my knowledge of the rigors of theoretical work. Other graduate students before me Udaya Rodrigo, David Hardy, Matthew Patterson, Lucy Kiruri, Paul Herring, and William Gehling made my experiences bearable and were more than willing to lend an ear when I had to vent frustrations. That is priceless.

The work done at CAMD could not have been done without such enthusiastic people at the helm especially in the midst of extreme uncertainty. In particular Rich Kurtz, Orhan Kizilkaya, Eizi Morikawa, Amitava Roy, and Greg Merchan taught me valuable lessons and tricks when dealing with synchrotron radiation. Orhan's enthusiasm for the work we were doing assured me that I certainly did not make a mistake coming to graduate school.

Our collaborators with the LSU Superfund Research Center are constantly pushing the scientific envelope and were kind enough to take me along for the ride. They also allowed me to contribute to the impressive work we are doing. Through their continued support it certainly made it worthwhile.

Not only has graduate school been challenging but life outside it as well. Very close family members are now gone including 5 grandparents, 5 uncles, 2 aunts, and a very close family friend. However, I know they will be looking on as I walk and get my Ph.D. I hope and pray they take comfort in knowing that I made it, but I still miss them.

Now to the people I can certainly write more than a few paragraphs about. First and foremost is my parents Keith and Love Joy. You have taught me so many life lessons that I couldn't possibly name them all. Mostly, you taught me never be satisfied with your current situation and always reach for the stars. No matter where I am I know I can always turn to you both and you wouldn't hesitate to be behind me lending your support no matter the cost. To my brother Brian and my sister Jamie. We certainly can say we have been through a lot together. I wouldn't trade a minute of it for the world. The times we have had are priceless and I hope to share them with my kids as both of you have with yours.

Finally, to my wife Nancy. You have certainly changed my life for the better. I no longer am alone when I face my steepest challenges. You are by my side always. I love you more than words can ever express. You have pushed me to the finish line of graduate school and we will cross the finish line of life together. I think I'll keep you.

Table of Contents

Abstract

We have investigated the electronic structure of environmentally persistent free radicals (EPFRs) formed on two different metal oxides: Cu(II)O and ZnO. Cu(II)O is known to be one of the most active metal oxides to form EPFRs. ZnO, however, forms the longest-lived EPFRs.

First, we examined the adsorption of phenol on different crystal faces of ZnO. Ultraviolet photoelectron spectroscopy (UPS) shows direct evidence of charge transfer away from the ZnO to the phenol. This differs from the hypothesized mechanism of EPFR formation that says that an electron is transferred to the metal oxide. UPS difference spectra also shows that the phenol HOMO on the ZnO(10$\underline{1}$0), ZnO(000$\underline{1}$)-Zn, and ZnO(0001)-O differs significantly between each crystal face. The ZnO(10$\underline{1}$0) matches well with a calculated spectrum of a single phenol molecule while the other two surfaces show states either being depopulated or degeneracy being added to the phenol. Electron energy loss spectroscopy shows significant HOMO-LUMO gap narrowing of phenol on ZnO(000$\underline{1}$)-Zn compared to gas phase phenol or physisorbed phenol. Low energy electron diffraction shows that phenol forms a semi-ordered c(2x2) superstructure only on the (10$\underline{1}$0) surface.

Second, we examined the adsorption of phenol and chlorinated EPFR precursors on Cu(II)O nanoparticles. X-ray absorption near edge structure revealed that by heating Cu(II)O nanoparticles without the presence of any EPFR precursors Cu(II)O is reduced to $Cu(I)_2O$. When Cu(II)O nanoparticles were exposed to phenol at 220 °C (minimal reduction by heating) reduction to $Cu(I)_2O$

was observed. This is direct evidence of charge transfer to the metal oxide in agreement with the hypothesized EPFR formation mechanism. The amount of reduction suggests that a significant fraction of metal atoms are on the interior of the nanoparticles and are unavailable for reduction, but the amount of reductions are inconsistent which could also suggests experimental flaws. Chlorinated EPFR precursors were adsorbed to Cu(II)O nanoparticles to observe the reactivity of the surface and measure their 3D structure using x-ray fluorescence spectroscopy. While we show distinct Cu peaks at the appropriate intensities no Cl was observed under any conditions which suggest possible dechlorination from either the spectrometer source or the nanoparticles.

Chapter 1
Introduction

1.1 Introduction to EPFRs: Properties

Environmentally Persistent Free Radicals (EPFRs) are a class of toxic compounds that persist for orders of magnitude longer than other radicals. With typical radicals lasting on the order of a few μs while EPFRs last hours, weeks, or even months. EPFRs are known to arise when aromatic hydrocarbons are chemisorbed to metal oxide powders [1-9]. The composite organic/metal oxide system is the EPFR. To date only a basic mechanism of EPFR formation has been proposed as shown in figure 1.1.

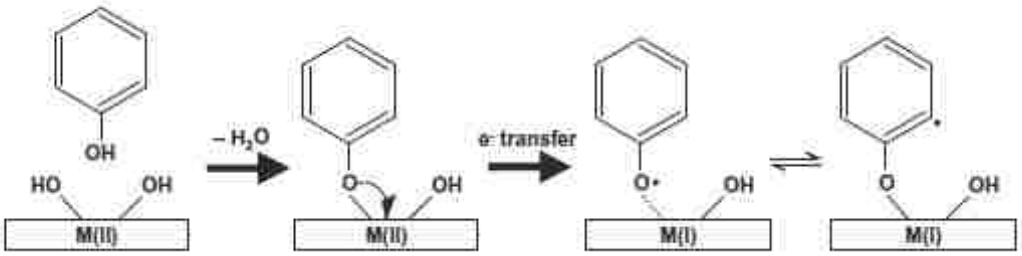

Figure 1.1 A general mechanism of radical formation from phenol adsorbed on a metal oxide surface [6].

There is little direct evidence that tells us about the structure of the adsorbate on the surface. We wish to obtain this type of information. Previous studies have mainly been done using electron paramagnetic resonance (EPR), which provides information regarding radical type and concentration that can be analyzed over time giving kinetics data. The mechanism consists of physisorption of the molecule, typically aromatic systems with alcohols or Cl bonded to the aromatic ring, to the surface followed by elimination of water or HCl (depending

on the precursor used) and chemisorption to the surface. During the chemisorption process electron transfer occurs, reducing the metal and forming the EPFR.

Ab initio calculations have shown that the stability of the EPFR comes from resonance with the phenyl ring and not only can oxygen centered radicals form, but carbon center radicals form as well [5, 10]. The resonance stabilization makes EPFRs resistant to decomposition and reactions with molecules in the air and allows the radicals to persist in an ambient environment, but they are by no means inert.

The lifetime of EPFRs is dependent a variety of factors including the precursor molecule. For instance, when Cu(II)O on silica is exposed to phenol the resultant radical has a 1/e half-life of 74 min. under ambient conditions. When Cu(II)O on silica is exposed to 2-monochlorophenol the resultant radical has a 1/e half-life of approximately 64 min. under the same conditions [4].

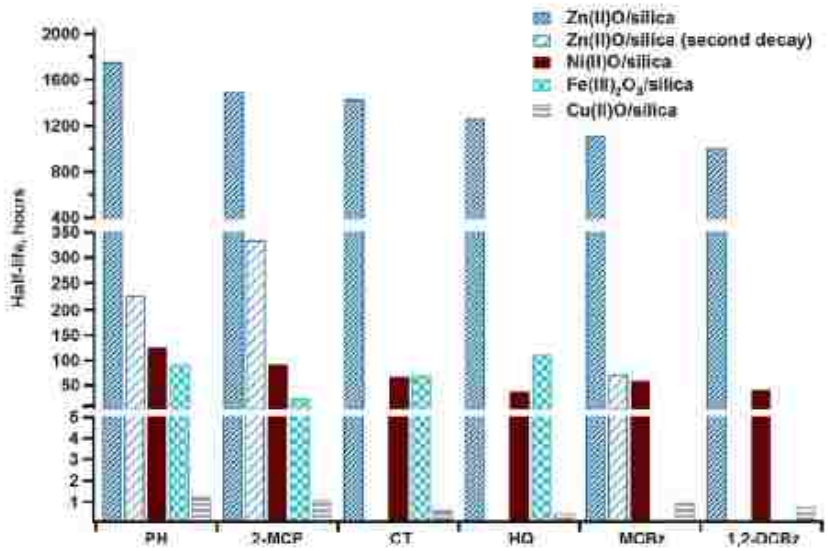

Figure 1.2 Comparison of different half-lives of EPFRs formed on different metal oxide nanoparticles [4].

Another factor governing the stability of radicals are the metal oxides as shown in figure 1.2. For example, when $Fe(III)_2O_3$ on silica is dosed with phenol the radical 1/e half-life is 3.8 days as compared to the 1/e half-life of 74 min. with Cu(II)O [1, 2]. This is not only the case with Cu(II)O and $Fe(III)_2O_3$, but also with a variety of other metal oxides including Zn(II)O, Al_2O_3, Ni(II)O, and TiO_2 [3, 4, 6]. Each forming radicals with different 1/e half-lives with Zn(II)O forming the longest lived radicals (1/e half-life = 73 days) [4]. Not only do different metal oxides produce radicals of different half-lives, they also produce different concentrations of radicals. This illustrates that some metal oxides are more active in forming radicals than others. For example, radicals formed on $Fe(III)_2O_3$ have a concentration that is an order of magnitude less than on Cu(II)O [2]. The same is true when comparing radicals formed on Al_2O_3 and TiO_2. Al_2O_3 radical concentration is an order of magnitude less than TiO_2 [6].

1.2 Sources of EPFRs

Combustion systems have been shown to be a leading source of particulate matter (PM) worldwide, with 70% to 90% of airborne PM originating in combustion processes [10]. Sources range from automobile combustion engines, refineries, biomass in households, and waste incinerators [10-19]. EPFRs form in the cool zone region of combustion reactions. Figure 1.3 is a zone diagram of a combustion system. Each region in the diagram is separated based on the temperatures of that particular region. Each region also is labeled regarding the predominant type of reaction that occurs in that region.

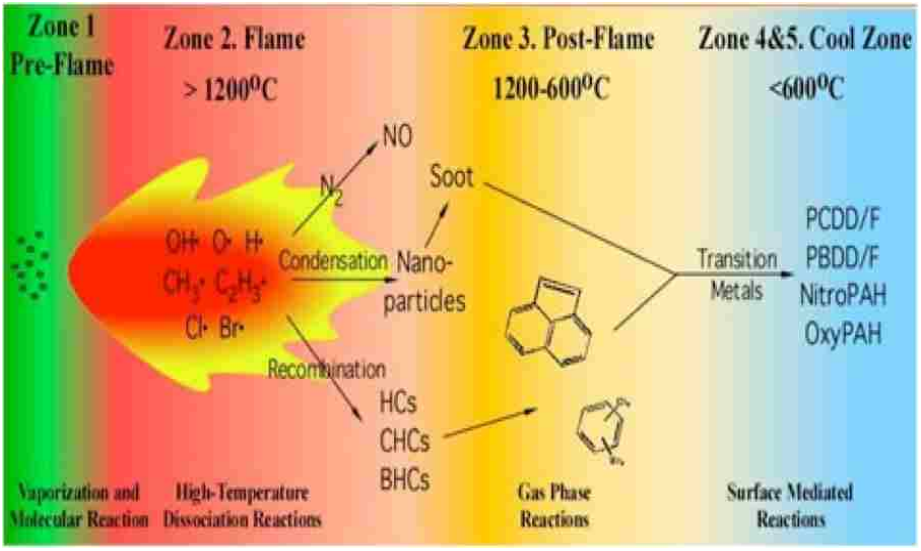

Figure 1.3 A diagram of a combustion system [20].

In the flame region (zone 2) no molecules survive the intense flame conditions. However, immediately after the flame region (zone 3) gas phase reactions take place. The temperatures in this region are still too high for solid matter to condense and interact with gas phase molecules. Between zones 3 and 4 nanoparticles are condensed typically on top of fly ash or airborne PM. Fly ash is a mixture of many different metal oxides. In zones 4&5-labeled cool zone is where surface mediated reactions take place. This zone is where EPFRs are expected to form on the surface of transition metal oxides [1-9]. Not only do EPFRs form in this region, but also other toxic compounds like dioxins and furans, which EPFRs are suspected to be an intermediate [5, 21, 22]. EFPRs are not only found to be associated with airborne PM, but have also been shown to persist in soils at superfund sites. The soil study showed 90% of the EPFR was contained in the mineral/clay/humins fraction [23].

1.3 Toxicity of EPFRs

In recent decades attention has been given to the toxicity of PM. Recent studies have now started to show that EPFRs may play a significant role in the toxicity of PM [24-26]. Initial studies of EPFR containing particles show significant lung and heart damage that go beyond the particles or pollutant alone. Inhalation of EPFR containing PM has been shown to cause pulmonary disease in neonatal rats [27]. Not only are the lungs affected, but a decrease in cardiac function has also been observed in animal models [28, 29]. It has also been observed that EPFRs can produce reactive oxygen species (ROS) in aqueous solutions [29, 30]. ROS are reactive molecules containing oxygen such as superoxide and peroxides. With an increase in ROS, a biological system's ability to detoxify the reactive species eventually is overridden triggering oxidative stress and resulting in tissue damage. Biological studies have demonstrated EPFRs produced ROS and contribute to oxidative stress resulting in damage to the heart and lungs [26-31].

The main contributor to the toxicity of PM for the most part has been unknown [32]. Epidemiological studies have demonstrated a link between PM exposures and chronic pulmonary diseases, cancer, cardiac effects, mortality, and morbidity [33-47]. The emergence of PM and its role in human health has sparked regulatory agencies such as the World Health Organization (WHO) and Environmental Protection Agency (EPA) to launch efforts into understanding the impacts PM has not only on human health but environmental health [47]. Researchers have noticed a trend between the toxicity of PM and the size of the particles. PM is a complex mixture of different materials that range in size and

composition from 10 μm to less than 0.1 μm, also called fine and ultrafine particles respectively. Smaller size PM (<2.5 μm) has been known to travel long distances and penetrate deep into the respiratory tract causing a variety of lung and heart diseases [48-50]. Smaller size particles occasionally have greater toxicity than larger particles. The smaller particles have a higher surface area allowing more organics to condense on the surface compared to larger sized PM [51]. These organics adsorbed on PM, once in the body can begin redox cycling inducing tissue damage [52].

The toxicology of PM is not only associated with its size, but also with its composition [53]. In some cases, researchers have demonstrated that composition can contribute more significantly than particle size [53, 54]. The composition of PM can be subdivided into four parts such as carbonaceous materials (including volatile organics), transition metal oxides, volatile ionic materials, and other non-volatile inorganic materials [55-61]. The transition metal oxides are the components that catalyze EPFR formation as well as dioxins and furans [62]. Transition metals such as iron and copper are abundant in combustion systems and iron(III) oxide and copper(II) oxide can account for up to 2.35% and 0.05% by mass respectively [63]. Not only are copper and iron abundant in combustion systems, but also nickel and zinc. All of these transition metals are present in PM at relatively high concentration [58-61, 64]. However, iron and copper are more active in the formation of dioxins and furans [65-68]. These transition metal oxides allow electron transfer processes to occur at the surface mediating the formation of organic pollutants such as dioxins, furans, and EPFRs. Studies have shown that

a significant amount of EPFRs are formed on the surface of combustion-generated particles [5,24, 69-74]. PM samples from U. S. cities were collected and analyzed for composition. The analysis revealed that semiquinone type radicals were present in the PM fraction and that these particles can damage DNA [24, 25].

1.4 Research Objectives

The objectives to this study are three fold. The first objective is to examine the atomistic and electronic structures of EPFRs formed on metal oxide single crystals and nanoparticles. Second is to use EPFR precursors to probe the nanoparticles themselves, namely, their 3D structure and the reactivity of metals on the surface. Lastly, is to examine the interactions between the EPFR precursors and the metal oxide substrates as a function of temperature (both nanoparticles and single crystals) and crystallographic face (single crystals).

This study focuses mainly on EPFRs formed on ZnO and Cu(II)O. ZnO forms the longest lived radicals regardless of precursor used to form the EPFR (radicals formed from phenol have the longest half-lives) [4]. The general scheme for EPFR formation shown in figure 1.1 shows an electron transfer accompanied by a reduction of the metal by one unit of charge. Zinc only has two known stable oxidation states, which are the +2 and 0 states. This demonstrates the importance of understanding the electronic structure of EPFRs in detail. ZnO also has only a few thermodynamically stable crystallographic faces [75]. This allows us to perform comprehensive experiments to understand how different faces interact with EPFR precursors and we can relate this to what is observed on the nanoparticles. Most of the previous studies on EPFR systems have been with

powder samples. These powder samples that contain metal oxides like silica, alumina, or titania as supports are made to mimic fly ash from waste incinerators. Mimics are synthesized to simplify measurements from combustion products and to learn what each component contributes to the whole system. Since ZnO single crystals have only a few stable crystallographic faces and limited oxidation states it provides a good model system for the powder samples. This allows us to use a more surface science approach to examine the electronic properties of EPFRs. This also allows us to use more unambiguous surface science measurements to obtain useful data that is relatable to the powder samples that have been used previously.

Cu(II)O has been studied in the past, but only at the micro scale [7, 8]. It has also been reported that Cu(II)O is one of the most active materials in EPFR formation [1]. We are extending these studies to the nanoscale to examine Cu(II)O nanoparticle interactions with EPFR precursors. We are also using EPFR precursors to obtain information about the Cu(II)O nanoparticle surface. Our experiments may also be used as guideposts to help theorists who are interested in such systems.

To carry out these objectives on single crystals, ultrahigh vacuum (UHV) systems with a base pressure of 10^{-10} Torr are needed. This is to ensure sample cleanliness and to ensure no interferences from molecules in the air. To examine the electronic structure of EFPRs and the interactions between phenol and ZnO; both ultraviolet photoelectron spectroscopy (UPS) and electron energy loss spectroscopy (EELS) were employed. UPS gives information regarding

occupied states below the Fermi level while EELS measures the energy gap between the occupied and the unoccupied states. By examining the UPS and EELS spectra, phenomena such as charge transfer can be observed along with other features of phenol and ZnO that may change upon adsorption. We also examined the phenol's symmetry after adorption using low energy electron diffraction (LEED). The sample in the UHV chambers can also be heated and cooled allowing us to examine temperature affects.

To examine the electronic structure and interactions between EPFR precursors and Cu(II)O nanoparticles XANES and x-ray fluorescence was used. To monitor the EPFRs with XANES an *in-situ* chamber was constructed to dose the Cu(II)O on site at the Center for Advanced Microstructures and Devices (CAMD). This allowed us to take measurements immediately after exposure to the EPFR precursor. For the x-ray fluorescence measurements, chlorinated precursors such as pentachlorophenol were used as a tag to examine the active sites on the nanoparticles as a function of size and temperature. This could be considered a spectroscopic titration to examine how many radicals occupy metal sites on the nanoparticle surface. This also has bearing in determining the 3D morphology of the nanoparticles themselves.

1.5 References

(1) Lomnicki, S.; Truong, H.; Vejerano, E.; Dellinger, B. Copper Oxide-Based Model of Persistent Free Radical Formation on Combustion-Derived Particulate Matter. *Environ. Sci. Technol.* **2008**, *42*, 4982–4988.

(2) Vejerano, E.; Lomnicki, S.; Dellinger, B. Formation and Stabilization of Combustion-Generated Environmentally Persistent Free Radicals on an $Fe(III)_2O_3$/Silica Surface. *Environ. Sci. Technol.* **2011**, *45*, 589–594.

(3) Vejerano, E.; Lomnicki, S. M.; Dellinger, B. Formation and Stabilization of Combustion-Generated, Environmentally Persistent Radicals on Ni(II)O Supported on a Silica Surface. *Environ. Sci. Technol.* **2012**, *46*, 9406–9411.

(4) Vejerano, E.; Lomnicki, S.; Dellinger, B. Lifetime of Combustion-Generated Environmentally Persistent Free Radicals on Zn(II)O and Other Transition Metal Oxides. *J. Environ. Monit.* **2012**, *14*, 2803–2806.

(5) Dellinger, B.; Lomnicki, S.; Khachatryan, L.; Maskos, Z.; Hall, R. W.; Adounkpe, J.; McFerrin, C.; Truong, H. Formation and Stabilization of Persistent Free Radicals. *P. Combust. Inst.* **2007**, *31*, 521–528.

(6) Patterson, M. C.; Keilbart, N. D.; Kiruri, L. W.; Thibodeaux, C. A.; Lomnicki, S.; Kurtz, R. L.; Poliakoff, E. D.; Dellinger, B.; Sprunger, P. T. EPFR Formation From Phenol Adsorption on Al_2O_3 and TiO_2: EPR and EELS Studies. *J. Chem. Phys.* **2013**, *422*, 277–282.

(7) Farquar, G. R.; Alderman, S. L.; Poliakoff, E. D.; Dellinger, B. X-Ray Spectroscopic Studies of the High Temperature Reduction of Cu(II)O by 2-Chlorophenol on a Simulated Fly Ash Surface. *Environ. Sci. Technol.* **2003**, *37*, 931–935.

(8) Alderman, S. L.; Farquar, G. R.; Poliakoff, E. D.; Dellinger, B. An Infrared and X-Ray Spectroscopic Study of the Reactions of 2-Chlorophenol, 1,2-Dichlorobenzene, and Chlorobenzene with Model CuO/Silica Fly Ash Surfaces. *Environ. Sci. Technol.* **2005**, *39*, 7396–7401.

(9) Kiruri, L. W.; Khachatryan, L.; Dellinger, B.; Lomnicki, S. Effect of Copper Oxide Concentration on the Formation and Persistency of Environmentally Persistent Free Radicals (EPFRs) in Particulates. *Environ. Sci. Technol.* **2014**, *48,* 2212–2217.

(10) Cass, G.R.; Hughes, L.A.; Bhave, P.; Kleeman, M.J.; Allen, J.O.; Salmon, L.G. The Chemical Composition of Atmospheric Ultrafine Particles. *Philos. Trans. R. Soc. London, A.* **2000**, *358(1775)*, 2581–2592.

(11) McFerrin, C. A.; Hall, R. W.; Dellinger, B. *Ab Initio* Study of the Formation and Degradation Reactions of Semiquinone and Phenoxyl Radicals. *J. Mol. Struc.-Theochem.* **2008**, *848*, 16–23.

(12) Chen, Y.Z.; Shah, N.; Huggins, F.E.; Huffman, G.P. Comparison of micron-sized and ultrafine particulate matter from pulverized coal combustion. *Abstr. Pap. Am. Chem. Soc.* **2005**, *229*, U866–U866.

(13) Chen, Y.; Shah, N.; Huggins, F.E.; Huffman, G.P.; Dozier, A. Characterization of Ultrafine Coal Fly Ash Particles by Energy-Filtered TEM. *J. Microsc.-Oxford.* 2005, *217(3)*, 225–234.

(14) Huffman, G.P.; Huggins, F.E.; Shah, N.; Huggins, R.; Linak, W.P.; Miller, C.A.; Pugmire, R.J.; Meuzelaar, H.L.C.; Seehra, M.S.; Manivannan, A. Characterization of Fine Particulate Matter Produced by Combustion of Residual Fuel Oil. *J. Air Waste Manage. Assoc.* **2000**, *50(7)*, 1106–1114.

(15) Chen, Y.; Shah, N.; Huggins, F.E.; Huffmann, G.P., Investigation of the Microcharacteristics of PM2.5 in Residual Oil Fly Ash by Analytical Transmission Electron Microscopy. Vol. 38. **2004**, Washington, DC, ETATS-UNIS: American Chemical Society.

(16) Kleeman, M.J.; Schauer, J.J.; Cass, G.R. Size and Composition Distribution of Fine Particulate Matter Emitted from Motor Vehicles. *Environ. Sci. Technol.* **2000**, *34(7)*, 1132–1142.

(17) Linak, W.P.; Miller, C.A.; Wendt, J.O.L. Comparison of Particle Size Distributions and Elemental Partitioning from the Combustion of Pulverized Coal and Residual Fuel Oil. *J. Air Waste Manage. Assoc.* **2000**, *50(8)*, 1532–1544.

(18) Okeson, C.D.; Riley, M.R.; Fernandez, A.; Wendt, J.O.L. Impact of the Composition of Combustion Generated Fine Particles on Epithelial Cell Toxicity: Influences of Metals on Metabolism. *Chemosphere.* **2003**, *51(10)*, 1121–1128.

(19) Kleeman, M.J.; Schauer, J.J.; Cass, G.R. Size and Composition Distribution of Fine Particulate Matter Emitted from Wood Burning, Meat Charbroiling, and Cigarettes. *Environ. Sci. Technol*. **1999**, *33(20)*, 3516–3523.

(20) LSU CAMD Highlights. http://www.camd.lsu.edu/highlights/environmentaltoxicology.htm (accessed March 30, 2014).

(21) Altwicker, E.R. Some Laboratory Experimental Designs for Obtaining Dynamic Property Data on Dioxins. *Sci. Total Environ.* **1991**, *104(1-2)*, 47-72.

(22) Gullett, B.K.; Lemieux, P.M.; Dunn, J.E. Role of Combustion and Sorbent Parameters In prevention of Polychlorinated Dibenzo-p-dioxin and Polychlorinated Dibenzofuran Formation During Waste Combustion. *Environ. Sci. Technol*. **1994**, *28(1),* 107-118.

(23) Cruz, dela, A. L. N.; Gehling, W.; Lomnicki, S.; Cook, R.; Dellinger, B. Detection of Environmentally Persistent Free Radicals at a Superfund Wood Treating Site. *Environ. Sci. Technol.* **2011**, *45*, 6356–6365.

(24) Dellinger, B.; Pryor, W.A.; Cueto, R.; Squadrito, G.L.; Deutsch, W.A. Combustion Generated Radicals and Their Role in the Toxicity of Fine Particulate. *Organohalogen Compd.* **2000**, *46*, 302–305.

(25) Dellinger, B.; Pryor, W. A.; Cueto, R.; Squadrito, G. L.; Hegde, V.; Deutsch, W. A. Role of Free Radicals in the Toxicity of Airborne Fine Particulate Matter. *Chem. Res. Toxicol.* **2001**, *14*, 1371–1377.

(26) Balakrishna, S.; Lomnicki, S.; McAvey, K. M.; Cole, R. B.; Dellinger, B.; Cormier, S. A. Environmentally Persistent Free Radicals Amplify Ultrafine Particle Mediated Cellular Oxidative Stress and Cytotoxicity. *Part. Fibre Toxicol.* **2009**, *6:11*.

(27) Balakrishna, S.; Saravia, J.; Thevenot, P.; Ahlert, T.; Lominiki, S.; Dellinger, B.; Cormier, S. A. Environmentally Persistent Free Radicals Induce Airway Hyperresponsiveness in Neonatal Rat Lungs. *Part. Fibre Toxicol.* **2011**, *8:11*.

(28) Mahne, S.; Chuang, G. C.; Pankey, E.; Kiruri, L.; Kadowitz, P. J.; Dellinger, B.; Varner, K. J. Environmentally Persistent Free Radicals Decrease Cardiac Function and Increase Pulmonary Artery Pressure. *Am. J. Physiol. Heart Circ. Physiol.* **2012**, *303*, H1135–H1142.

(29) Lord, K.; Moll, D.; Lindsey, J. K.; Mahne, S.; Raman, G.; Dugas, T.; Cormier, S. A.; Troxlair, D.; Lominiki, S.; Dellinger, B.; Varner, K. Environmentally Persistant Free Radicals Decrease Cardiac Function Before and After Ischemia/Reperfusion Injury in Vivo. *J. Recept. Signal Transduct. Res.* **2011**, *31*, 157–167.

(30) Khachatryan, L.; Vejerano, E.;Lomnicki S.;Dellinger, B. Environmentally Persistant Free Radicals (EPFRs). 1. Generation of Reactive Oxygen Species in Aqueous Solutions. *Environ. Sci. Technol*. **2011**, 45, 8559–8566.

(31) Fahmy, B.; Ding, L.; You, D.; Lomnicki, S.; Dellinger, B.; Cormier, S. A. In Vitro and in Vivo Assessment of Pulmonary Risk Associated with Exposure to Combustion Generated Fine Particles. *Environ. Toxicol. Phar.* **2010**, *29*, 173–182.

(32) Nel, A.E.; Diaz-Sanchez, D.; Li, N. The Role of Particulate Pollutants in Pulmonary Inflammation and Asthma: Evidence for the Involvement of Organic Chemicals and Oxidative Stress. *Curr. Opin. Pulm*. *Med.* **2001**, 7(1), 20–26.

(33) Laden, F.; Neas, L. M.; Dockery, D. W.; Schwartz, J. E. Association of Fine Particulate Matter From Different Sources with Daily Mortality in Six U.S. Cities. *Environ. Health Persp.* **2000**, *108(10),* 941–947.

(34) Dockery, D.W.; Pope, C.A.; Xu, X.; Spengler, J.D.; Ware, J.H.; Fay, M.E.; Ferris, B.G.; Speizer, F.E. An Association Between Air Pollution and Mortality in Six US Cities. *N. Engl. J. Med.* **1993**, *329*, 1753–1759.

(35) Pope III, C.A.; Burnett, R.T.; Thun, M.J.; Calle, E.E.; Krewski, D.; Ito, K.; Thurston, G.D. Lung Cancer, Cardiopulmonary Mortality, and Long-Term Exposure to Fine Particulate Air Pollution. JAMA **2002**, *287(9),* 1132–1141.

(36) Ibald-Mulli, A.; Wichmann, H.E.; Kreyling, W.; Peters, A., Epidemiological Evidence on Health Effects of Ultrafine Particles. J. Aerosol. Med**. 2002**, *15,*189–201.

(37) Cormier, S. A.; Lomnicki, S.; Backes, W.; Dellinger, B. Origin and Health Impacts of Emissions of Toxic by-Products and Fine Particles From Combustion and Thermal Treatment of Hazardous Wastes and Materials. *Environ. Health Perspect.* **2006**, *114*, 810–817.

(38) Lighty, J. S.; Veranth, J. M.; Sarofim, A. F. Combustion Aerosols: Factors Governing Their Size and Composition and Implications to Human Health. *J. Air & Waste Manage. Assoc.* **2000**, *50*, 1565–1618.

(39) Fahmy, B.; Ding, L.; You, D.; Lomnicki, S.; Dellinger, B.; Cormier, S. A. In Vitro and in Vivo Assessment of Pulmonary Risk Associated with Exposure to Combustion Generated Fine Particles. *Environ. Toxicol. Phar.* **2010**, *29*, 173–182.

(40) Donaldson, K.; Li, X. Y.; MacNee, W. Ultrafine (Nanometre) Particle Mediated Lung Injury. *J. Aerosol Sci.* **1998**, *29*, 553–560.

(41) Avakian, M. D.; Dellinger, B.; Fielder, H.; Gullet, B.; Koshland, C.; Marklund, S.; Oberdorster, G.; Safe, S.; Sarofim, A. F.; Smith, K. R.; Schwartz, D.; Suk, W.The Origin, Fate, and Health Effects of Combustion by-Products: A Research Framework. *Environ Health Persp* **2002**, *110*, 1155–1162.

(42) Kennedy, I. M. The Health Effects of Combustion-Generated Aerosols. *Proc. Combust. Inst.* **2007**, *31*, 2757–2770.

(43) Peters, A.; Dockery, D. W.; Muller, J. E.; Mittleman, M. A. Increased Particulate Air Pollution and the Triggering of Myocardial Infarction. *Circulation* **2001**, *103*, 2810–2815.

(44) Wichmann, H. E.; Peters, A. Epidemiological Evidence of the Effects of Ultrafine Particle Exposure. *Philos. Trans. R. Soc. London, A.* **2000**, *358*, 2751–2769.

(45) Nel, A. Atmospere: Enhanced: Air Pollution-Related Illness: Effects of Particles. *Science.* **2005**, *308*, 804–808.

(46) Donaldson, K.; Tran, L.; Jimenez, L.; Duffin, R.; Newby, D. E.; Mills, N.; MacNee, W.; Stone, V. Combustion-Derived Nanoparticles: a Review of Their Toxicology Following Inhalation Exposure. *Part. Fibre Toxicol.* **2005**, *2:10*.

(47) Ibald-Mulli, A.; Wichmann, H.E.; Kreyling, W.; Peters, A., Epidemiological Evidence on Health Effects of Ultrafine Particles. *J. Aerosol. Med.* **2002**, *15*,189–201.

(48) Calderon-Garciduenas, L.; Mora-Tiscareno, A.; Fordham, L.A.; Chung, C.J.; Garcia, R.; Osnaya, N.; Hernandez, J.; Acuna, H.; Gambling, T.M.; Villarreal-Calderon, A.; Carson, J.; Koren, H.S.; Devlin, B. Canines as Sentinel Species for Assessing Chronic Exposures to Air Pollutants: Part 1. Respiratory Pathology. *Toxicol. Sci.* **2001**, *61(2),* 342–355.

(49) Calderon-Garciduenas, L.; Gambling, T.M.; Acuna, H.; Garcia, R.; Osnaya, N.; Monroy, S.; Villarreal-Calderon, A.; Carson, J.; Koren, H.S.; Devlin, R.B. Canines as Sentinel Species for Assessing Chronic Exposures to Air Pollutants: Part 2. Cardiac Pathology. *Toxicol. Sci*. **2001**, 61(2), 356–367.

(50) Nemmar, A.; Vanquickenborne, B.; Dinsdale, D.; Thomeer, M.; Hoylaerts, M.F.; Vanbilloen, H.; Mortelmans, L.; Nemery, B. Passage of Inhaled Particles Into the Blood Circulation in Humans. *Circulation.* **2002**, *105(4),* 411–414.

(51) Oberdorster, G. Pulmonary Effects of Inhaled Ultrafine Particles. *Int. Arch. Occup. Environ. Health.* **2001**, *74(1),* 1–8.

(52) Ning, L.; Sioutas, C.; Cho, A.; Schmitz, D.; Misra, C.; Sempf, J.; Meiying, W.; Oberley, T.; Froines, J.; Nel, A. Ultrafine Particulate Pollutants Induce Oxidative Stress and Mitochonrial Damage. *Environ. Health Perspect.* **2003**, *111(4),* 455–460.

(53) Duffin, R.; Tran, C. L.; Clouter, A.; Brown, D. M.; MacNee, W.; Stone, V.; Donaldson, K. The Importance of Surface Area and SpecificReactivity in the Acute Pulmonary InflammatoryResponse to Particles. *Ann. Occup. Hyg.* **2002**, 46, 242–245.

(54) Karlsson, H. L.; Gustafsson, J.; Cronholm, P.; Möller, L. Size-Dependent Toxicity of Metal Oxide Particles—a Comparison Between Nano- and Micrometer Size. *Toxicol. Lett.* **2009**, *188*, 112–118.

(55) Rogge, W. F.; Hlldemann, L. M.; Mazurek, M. A.; Cass, G. R. Sources of Fine Organic Aerosol. 2. Noncatalyst and Catalyst-EquippedAutomobiles and Heavy-Duty Diesel Trucks. *Environ. Sci. Technol.* **1993**, *27*, 636–651.

(56) Fine, P. M.; Cass, G. R.; Simoneit, B. R. T. Chemical Characterization of Fine Particle Emissions From Fireplace Combustion of Woods Grown in the Northeastern United States. *Environ. Sci. Technol.* **2001**, *35*, 2665–2675.

(57) Nelson, P. F. Trace Metal Emissions in Fine Particles From Coal Combustion. *Energy Fuels.* **2007**, *21*, 477–484.

(58) Fine, P. M.; Cass, G. R.; Simoneit, B. R. T. Chemical Characterization of Fine Particle Emissions From the Fireplace Combustion of Woods Grown in the Southern United States. *Environ. Sci. Technol.* **2002**, *36*, 1442–1451.

(59) Murillo, J. H.; Ramos, A. C.; García, F. Á.; Jiménez, S. B.; Cárdenas, B.; Mizohata, A. Chemical Composition of $PM_{2.5}$ Particles in Salamanca, Guanajuato Mexico: Source Apportionment with Receptor Models. *Atmos. Res.* **2012**, *107*, 31–41.

(60) Qureshi, S.; Dutkiewicz, V. A.; Khan, A. R.; Swami, K.; Yang, K. X.; Husain, L.; Schwab, J. J.; Demerjian, K. L. Elemental Composition of PM2.5 Aerosols in Queens, New York: Solubility and Temporal Trends. *Atmos. Environ.* **2006**, *40*, 238–251.

(61) Yongjie, Y.; Yuesi, W.; Tianxue, W.; Wei, L.; Ya'nan, Z.; Liang, L. Elemental composition of $PM_{2.5}$ and PM_{10} at Mount Gongga in China during 2006. *Atmos. Res.* **2009**, *93*, 801–810.

(62) Lomnicki, S.; Dellinger, B. A Detailed Mechanism of the Surface-Mediated Formation of PCDD/F From the Oxidation of 2-Chlorophenol on a CuO/Silica Surface. *J. Phys. Chem. A* **2003**, *107*, 4387–4395.

(63) Ceramics From Incinerator Fly Ashes. Part II. The Influence of the Particle Size and Heat-Treatment on the Properties. *J. Eur. Ceram. Soc*. **2003**, *23(10),* 1609–1615.

(64) Okeson, C.D.; Riley, M.R.; Fernandez, A.; Wendt, J.O.L. Impact of the Composition of Combustion Generated Fine Particles on Epithelial Cell Toxicity: Influences of Metals on Metabolism. *Chemosphere.* **2003**, 51(10), 1121–1128.

(65) Tuppurainen, K.A.; Ruokojaervi, P.H.; Asikainen, A.H.; Aatamila, M.; Ruuskanen, J. Chlorophenols as precursors of PCDD/Fs in incineration processes: Correlations, PLS Modeling, and Reaction Mechanisms. *Environ. Sci. Technol.* **2000**, *34(23),* 4958–4962.

(66) Gullett, B.K.; Bruce, K.R.; Beach, L.O. The Effect of Metal-Catalysts on the Formation of Polychlorinated Dibenzo-para-dioxin and Polychlorinated Dibenzofuran Precursors. *Chemosphere*. **1990**, *20(10-12),* 1945–1952.

(67) Addink, R.; Altwicker, E.R. Formation of Polychlorinated Dibenzo-p-dioxins and Dibenzofurans on Secondary Combustor/Boiler Ash From a Rotary Kiln Burning Hazardous Waste. *J. Hazard. Mater.* **2004,** *114(1-3)*, 53–58.

(68) Nganai, S.; Lomnicki, S.; Dellinger, B. Ferric Oxide Mediated Formation of PCDD/Fs From 2-Monochlorophenol. *Environ. Sci. Technol.* **2009***, 43(2),* 368–373.

(69) Oettinger, R.; Drumm, K.; Knorst, M.; Krinyak, P.; Smolarski, R.; Kienast, K. Production of Reactive Oxygen Intermediates by Human Macrophages Exposed to Soot Particles and Asbestos Fibers and Increase in NF-kappa b p50/p105 mRNA. *Lung.* **1999**, *177(6)*, 343–354.

(70) Sagai, M.; Lim, H.-B.; Ichinose, T. Lung Carcinogenesis by Diesel Exhaust Particles and the Carcinogenic Mechanism via Active Oxygens. *Inhal. Toxicol.* **2000**,*12,* Suppl. 3, 215–223.

(71) Samet, J.M.; Dominici, F.; Curriero, F.C.; Coursac, I.; Zeger, S.L. Fine Particulate Air Pollution and Mortality in 20 U.S. Cities, 1987-1994. *N. Engl. J. Med.* **2000**, *343(24),* 1742–1749.

(72) Maskos, Z.; Khachatryan, L.; Dellinger, B. Precursors of Radicals in Tobacco Smoke and the Role of Particulate Matter in Forming and Stabilizing Radicals. *Energy Fuels.* **2005**, *19*, 2466–247.

(73) Nel, A.E.; Diaz-Sanchez, D.; Li, N. The Role of Particulate Pollutants in Pulmonary Inflammation and Asthma: Evidence for the Involvement of Organic Chemicals and Oxidative Stress. *Curr. Opin. Pulm*. *Med.* **2001**, 7(1), 20–26

(74) Khachatryan, L.; Dellinger, B. Environmentally Persistant Free Radicals (EPFRs)-2. Are Free Hydroxyl Radicals Generated in Aqueous Solutions. *Environ. Sci. Technol*. **2011**, 45, 9232–9239.

(75) Woll, C. The Chemistry and Physics of Zinc Oxide Surfaces. *Progress in Surface Science* **2007**, *82*, 55–120.

Chapter 2
Experimental Methods

2.1 Introduction

The experiments involved in these studies depend heavily on our capacity to prepare and characterize samples with well-defined and extremely clean surfaces. The experiments require conditions where samples are exposed to precise quantities of a particular gas and various measurements are performed. In this chapter, I describe the methods used for probing surface symmetry and morphology (LEED) and spectroscopic methods to examine the electronic structure of surfaces (UPS and EELS). Since combustion systems are very complex, containing many metal oxide nanoparticles, surrogate systems have to be made to simplify experiments. Therefore, also in this chapter is the method we used for nanoparticle synthesis.

2.2 Ultra-High Vacuum (UHV) Systems

Surface science experiments require UHV conditions; otherwise the experiments would be futile to conduct. Two basic principles exist to understand why UHV conditions are vital for surface science measurements. These principles are the mean free path of ideal gas molecules and the rate at which gas molecules impinge on the surface.

When we consider a gas molecule to be a rigid sphere with a diameter d and using kinetic theory we can derive the number of collisions made by one molecule divided by the time interval during which the collisions are counted, also called the collision frequency z yielding the equation:

$$z = \sigma c_{rel} \frac{N}{V} \tag{2.1}$$

where σ is the collision cross section (πd^2), c_{rel} is the relative mean speed, and N is the number density of molecules, and V is volume [1]. The relative mean speed is the average speed with which one molecule approaches another. To calculate the relative mean speed between different molecules, the Maxwell distribution is needed to yield the following expression:

$$c_{rel} = \left(\frac{8k_BT}{\pi\mu}\right)^{1/2} \qquad \mu = \frac{m_A m_B}{m_A + m_B} \tag{2.2}$$

where μ is the reduced mass of the molecules, k_B is Boltzmann's constant, and T is temperature. The relative mean speed can also be written in terms of the mean speed c (also derived from the Maxwell distribution) to derive a more simple expression:

$$c_{rel} = 2^{1/2} c \tag{2.3}$$

for our application it is more meaningful to have the collision frequency in terms of pressure rather than the number of molecules (N) per volume (V). To do that we can we can rewrite N using the following relation:

$$\frac{N}{V} = \frac{nN}{V} = \frac{pN}{V} = \frac{p}{k_BT} \tag{2.4}$$

By using equation 2.4 we can calculate the collision frequency based on more measurable quantities to yield the following:

$$Z = \frac{\sigma c_{rel} p}{k_BT} \tag{2.5}$$

Equation 2.5 shows that at constant temperature the collision frequency is proportional to the pressure of the system. This proportionality makes sense in

that if the pressure increases, the rate at which molecules hit one another becomes greater. This is true even if the molecule's average speed is the same [1].

Using the equation 2.5, we can now calculate the mean free path λ of gas molecules. When molecules collide with a frequency *z,* the time the molecules are travelling between collisions is 1/*z*. The distance the molecules travel then becomes (1/*z*)*c*. We can therefore write the mean free path equation as:

$$\lambda = \frac{c}{z} \tag{2.6}$$

By substituting 2.5 into 2.6 we can rewrite the mean free path equation in terms of quantities that are easily measured to yield equation 2.7.

$$\lambda = \frac{k_B T}{\sigma p 2^{1/2}} \tag{2.7}$$

Equation 2.7 shows that the distance between collisions has little to do with the speed at which molecules are traveling. Rather, it is dependent upon the number of molecules in a given volume. Essentially, if the pressure inside a chamber is doubled then the mean free path is reduced by one half. The typical mean free path of a gas molecule is on the order of nanometers at atmospheric temperature and pressure. If the pressure is lowered to UHV (10^{-10} Torr) the mean free path jumps several orders of magnitude to the scale of kilometers. Effectively, the molecules spend more time apart than colliding with each other [1, 2]. This also has the consequence that gas molecules under UHV conditions are more likely to strike the walls of the chamber than each other. This creates conditions that pumps have to operate under to make UHV pressures obtainable.

The second key concept to understand is the rate at which molecules impinge on a surface. The main purpose of UHV conditions is to limit the interactions of foreign materials with a solid surface. For this we can again turn to the kinetic theory of gases to calculate the rate molecules hit an area, which is given by:

$$F = \frac{p}{\sqrt{2\pi m k_B T}} \tag{2.8}$$

Where p is pressure, m is the molecular mass of the gas, k_B is Boltzmann's constant, and T is temperature [2]. At room temperature and a pressure of 10^{-6} Torr, equation 2.8 gives a rate of 10^{14}-10^{15} molecules/cm^2/s for common atmospheric gases like H_2O, O_2, and CO_2 [2, 3]. This means that at 10^{-6} Torr , 10^{15} molecules/cm^2 will cover the surface. This assumes that when a molecule strikes the surface it will stick (sticking coefficient of 1). To effectively minimize the molecules at the surface, lower pressures are needed. If the system is pumped down four more orders of magnitude to 10^{-10} Torr, then a much longer time is needed for gas molecules to accumulate on the surface, approximately on the order of hours before the sample needs to be cleaned again [2, 3]. This does affect the types of experiments one can choose perform, namely surface science versus powdered samples. High surface area powders would take even longer for molecules to accumulate on their surface especially at the lower pressures required for surface science experiments. Therefore, powder samples are typically done at higher pressures (~10^{-3} Torr).

A potential problem with this is that other molecules can adsorb along with the molecule of interest leading to contamination. Surface science experiments are performed under much “cleaner” conditions. Therefore, the molecules of interest are being measured. If contamination does result, it can easily be measured. While ambient pressure powder studies can identify if radicals are present using techniques like EPR; they cannot reveal if molecules donate charge to the surface or more subtle interactions between the adsorbate and surface.

As mentioned previously, due to the large mean free path of the molecules at lower pressures, molecules collide with the walls more than each other. These gas molecules adsorb to the walls of the chamber and out gas very slowly over time. Effectively, the walls of the chamber have a great impact on the overall pressure of the system. To decrease the amount of time it takes for the chamber to achieve UHV a bake-out is needed. This desorbs molecules from the walls to be pumped out of the system [2, 3]. To do this heating tape is wrapped around the chamber along with either heating blankets or aluminum foil to ensure even heating across the entire system. The system is then heated to 100-150 °C for hours to increase the desorption rate of molecules to be pumped out. The entire process can take, including a cool down period, 24-48 hr. [3]. As an example of the effectiveness of the bake-out, a mass spectrum before and after bake-out is shown in figure 2.1.

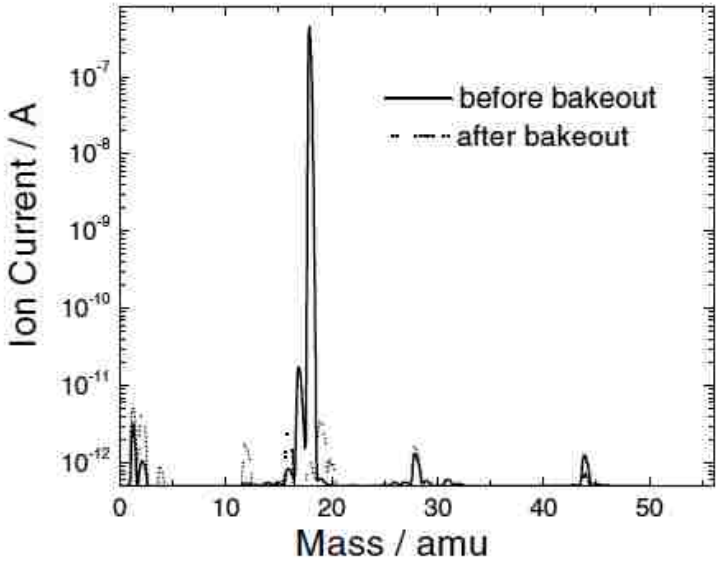

Figure 2.1 Mass spectra of various gases in a UHV chamber before and after bake-out [2].

To achieve UHV conditions complex pumping systems are usually employed. The first type of pump used is called a roughing pump. These pumps are usually rotary pumps that can be either oil lubricated or oil free. Roughing pumps bring the chamber from atmospheric pressure to 10^{-3} Torr. The next pump to be used is a turbo-molecular pump. A cutaway view of a turbo pump is shown in figure 2.2. The turbo pump relies on blades that are angled downward to drive gases through the stack and out the chamber. These blades spin at extremely high speeds (~80,000-90,000 rpm) and are capable of pulling a vacuum of 10^{-9} Torr or lower depending upon the model. Since molecules strike these blades at extremely high speeds friction can become a problem. Excess heat can build up requiring the need for these mechanical pumps to either be air-cooled (fan) or water cooled [2].

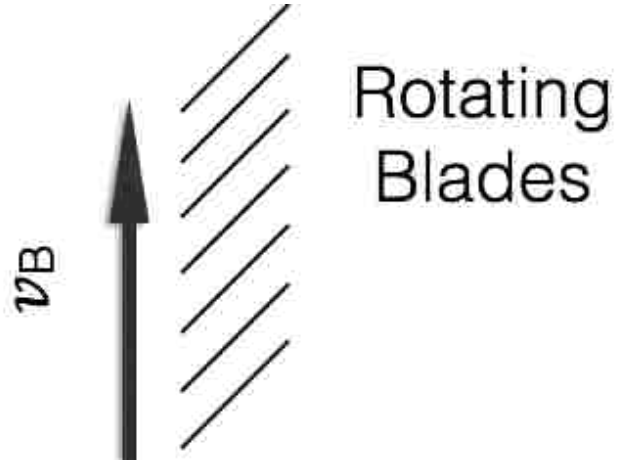

Figure 2.2 A cutaway of a turbo pump. The speed of the blades is given by v_B. The arrows indicate the velocity of gas molecules on either side with respect to the turbine blades.

The last type of pump that can be used to achieve UHV is the ion pump, which is shown in figure 2.3. The ion pump is radically different than the other two pump types in that there is no mechanical mechanism driving the system nor does the ion pump need a roughing pump to work. The ion pump works by applying a large potential difference (5-7 kV) between an anode and a cathode. This field causes electrons to be ejected from the cathode. The magnetic forces guide the electrons on an orbital path. This increases the probability that the electron will collide with gas molecules effectively ionizing them. The ionized gas molecules are then accelerated toward the cathode by the electric field. The cathode is usually coated in titanium because of its good mechanical properties and it readily reacts with residual gases (except the noble gases). When ionized gas molecules collide with the cathode, the titanium is sputtered off and coats the collector. The amount of titanium that makes it to the collector is proportional to the number of gas molecules that struck the cathode, which is also proportional to the pressure in the system. As more and more titanium is added to the

collector the gas molecules become trapped and are unable to be released back into the gas phase. Ion pumps are incapable of working at higher pressures due to plasma discharge. However, they can effectively maintain systems at UHV conditions (10^{-10} Torr) or lower [2].

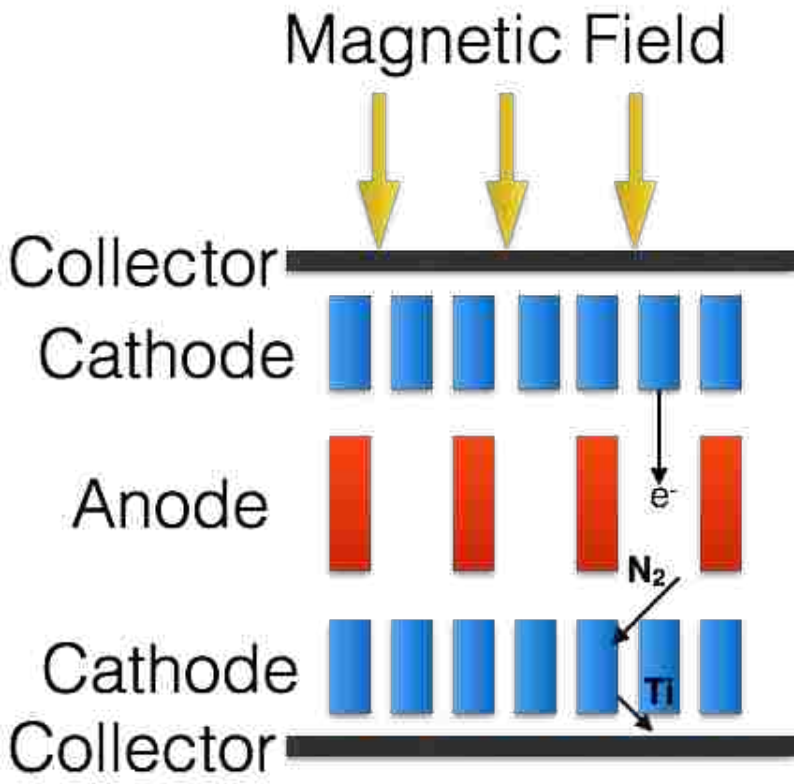

Figure 2.3 A diagram of a triode ion pump.

The single crystal samples we use are purchased from commercial vendors like MTI Corp. The vendors sell them cut and polished along a particular atomic plane to their specifications. However, after loading the samples in a UHV chamber, the samples still require several cycles of cleaning before they are suitable for experiments. The contamination present on the solid surface is sputtered off using cycles of ion sputtering. Typically, the ions of choice are either Ne^+ or Ar^+ at 1.5 kV. After sputtering, we anneal the sample to promote the

diffusion of atoms from the bulk to the surface to make atomically flat surfaces. Each chamber is equipped with a sample manipulator that has a tungsten filament attached behind the sample. This allows us to heat the samples to the appropriate temperature (up to 1200 °C) for various experiments.

2.3 Nanoparticle Synthesis

2.3.1 Materials

$Cu(NO_3)_2$• $2.5H_2O$, 99.99% anhydrous Cu_2(I)O and Cu(II)O powder was used as received from Sigma-Aldrich. The hydrated copper salt might have additional hydration. This makes the synthesis of the nanoparticles more qualitative than quantitative. The Cu_2(I)O and Cu(II)O were used as standards for XANES experiments. Cab-O-Sil high purity silica (SiO_2) with a surface area of 380 m^2/g (EH-5) was purchased from CABOT Corporation. The inert SiO_2 was used as the supporting matrix for the Cu(II)O nanoparticles. Cab-o-sil has been used by Dr. Dellinger's laboratory for years as a supporting matrix for metal oxide nanoparticle surrogates. This matrix is largely amorphous and not crystalline.

2.3.2 Incipient Wetness Impregnation

The incipient wetness impregnation method for nanoparticle synthesis is an easy and inexpensive way to make metal oxide nanoparticles with defined sizes supported on other metal oxides as compared to other methods such as dendrimeric preparations [4, 5]. A series of Cu(II)O nanoparticles were prepared by varying the percent by weight (wt.%) of Cu(II)O.

By varying the wt.%, the size of the nanoparticles can be controlled. $Cu(NO_3)_2 \bullet 2.5H_2O$ is dissolved in methanol and added directly to the support substrate (SiO_2), coating all the dry powder with the solution. The mixture is then allowed to dry for 24 hr. in a desiccator. Finally, the $Cu(NO_3)_2$ coated SiO_2 is calcined in a furnace at 450 °C in air for three hours to evaporate the organics and oxidize the metals. A schematic of this procedure is shown in figure 2.4

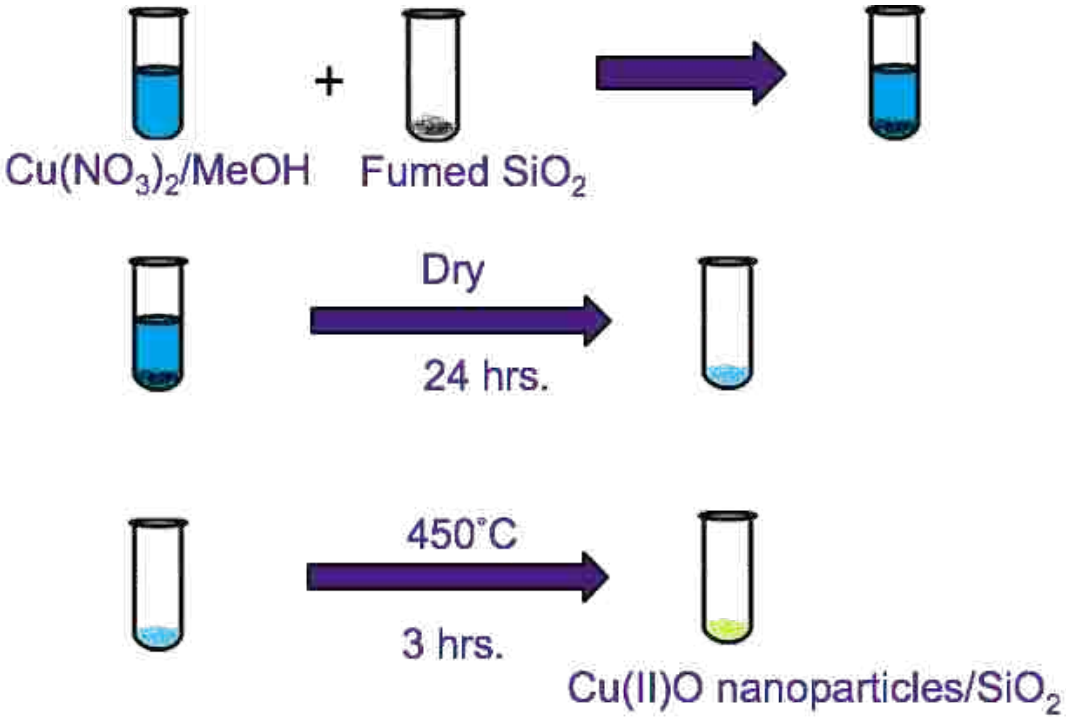

Figure 2.4 Schematic diagram of the incipient wetness impregnation preparation.

The nanoparticles were imaged using the JEOL 1010 high-resolution transmission electron microscope located at the LSU materials characterization center (LSUMCC).

Samples were imaged on Au holey carbon coated grids. To measure nanoparticle size distributions, the software package ImageJ by the National Institute of Health was used.

2.4 Detection and Analysis of EPFRs

EPFRs have been observed using a few choice techniques. One of the most obvious techniques is known as EPR. EPR is a sensitive technique that has the capabilities to identify radical types (g-factor), monitor decay rates, and determine concentration of radicals. The concentration is given in the unit of radicals/g. However, EPR is not the only technique that can identify and determine the properties of radicals. In figure 1.1, the schematic shows the electron being transferred to a metal oxide reducing the metal by one unit of charge. In theory, the oxidation state change of the metal can be used to detect if EPFRs are forming. A technique used to monitor oxidation states is known as x-ray absorption near edge structure (XANES). XANES is an element specific technique that can determine electronic structure changes in the metal oxide. It can also be used to determine percentages of mixed oxidation states.

2.4.1 Electron Paramagnetic Resonance

EPR is a technique designed to study systems with unpaired electrons. Much like nuclear magnetic resonance, EPR applies an external magnetic field to split spin states [6, 7]. Unlike NMR that splits nuclear spin states; EPR splits electron spin states. Shown in figure 2.5 is a diagram showing the energy splitting of a free electron by an external magnetic field.

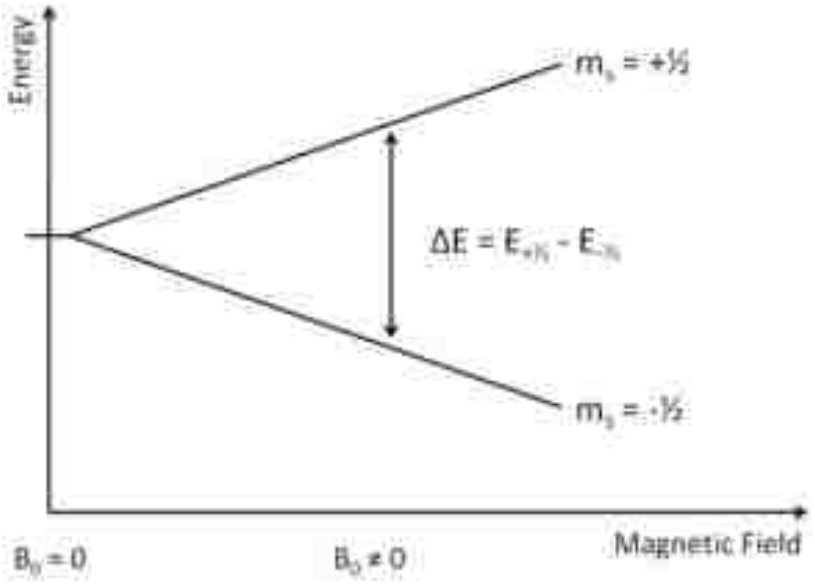

Figure 2.5 Diagram showing the splitting of a free electron [6].

Electrons can either occupy the m_s = ½ state or the m_s = -1/2. Both states initially have the same energy (degenerate) before the magnetic field is applied. Once the spin states are split, microwave radiation is applied, and absorbance spectra are obtained. The overall absorbance can then be used in equation 2.9 to show how the absorbance relates to the applied magnetic field [6].

$$\Delta E = h\nu = \ g_e \beta_B B_0 \qquad (2.9)$$

In equation 2.9, ΔE is the absorbance, h is plank's constant, v is the frequency of radiation, g_e is the g-factor, β_B is the Bohr magneton, and B_0 is the applied magnetic field. EPR experiments can either vary the radiation or vary the magnetic field while keeping one or the other constant. Most experiments vary the magnetic field until the radiation is equal to the difference in energy of the spin states, this is called "tuning" [7]. Like most absorption techniques a spectrum is produced like what is shown in figure 2.6.

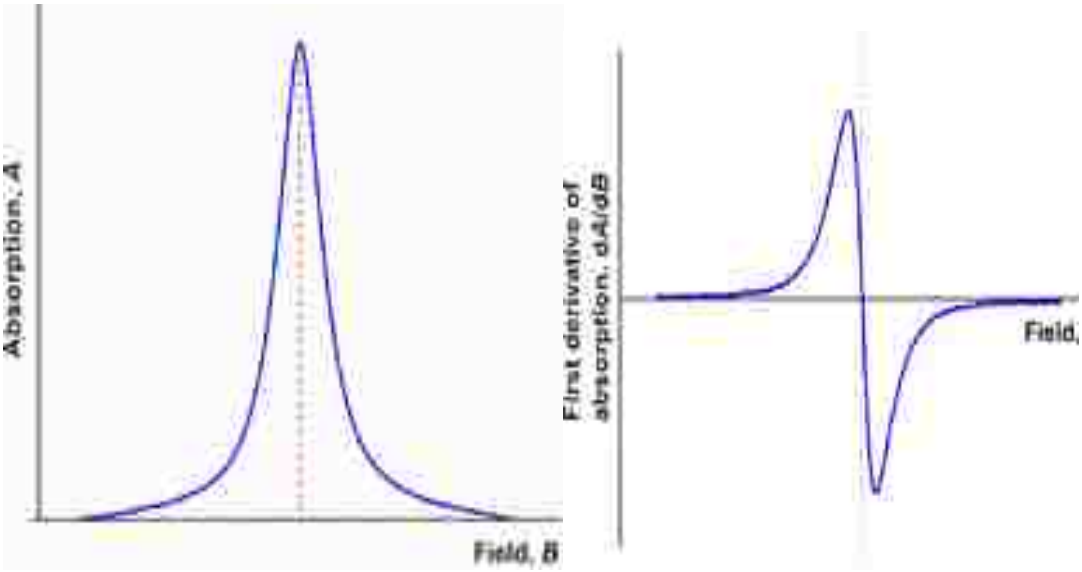

Figure 2.6 A sample absorption spectrum from an EPR experiment (left). The derivative spectrum of the absorbance spectrum (right) [7].

Unlike most spectroscopy techniques, a phase sensitive detector is used. This produces a first derivative spectrum like in figure 2.6 on the right [7]. The peak of the absorbance spectrum in figure 2.6 (left) corresponds to where the spectrum crosses zero in the derivative spectrum. This in essence indicates where the center of the spectrum is located. If equation 2.9 is slightly rearranged yielding equation 2.10, then more useful information can be obtained. This equation solves for the proportionality factor also known as the g-factor.

$$g_e = \frac{h\nu}{\beta_e B_0} \tag{2.10}$$

The g-factor gives information on the electronic structure of the radical. The neighboring atoms influence the radical and hence influence the g-factor [7]. In essence it can be used to identify the type of radical present in a sample. For example, the g-factor for a free electron is 2.00232. Organic radicals do not stray very far from this value. For organic radicals, the g-factor can give information on

where the radical is centered; whether it is carbon or oxygen centered and it can indicate different types of radicals in the same sample. For transition metals, more interactions take place such as spin-orbit coupling and zero-field splitting that causes the g-value to be anywhere between 1.4-3.0 [7].

Another useful parameter for EPFR studies is the radical concentration. With EPR, the radicals/g concentration can be calculated and tracked over a period of time by integrating the area under the absorption curve and comparing it to the standard 2,2-diphenyl-1-picrylhydrazyl (DPPH). The area is then divided by the amount of sample present in the EPR. This allows decay profiles to be created. Decays can have more than one rate yielding strong evidence for the presence of more than one radical type. Figure 2.7 shows the decay rates of various radicals formed on 5% CuO on SiO_2. These decay rates are then used to determine the 1/e half-lives of the radicals. This gives important information as to what their identities and their kinetic properties.

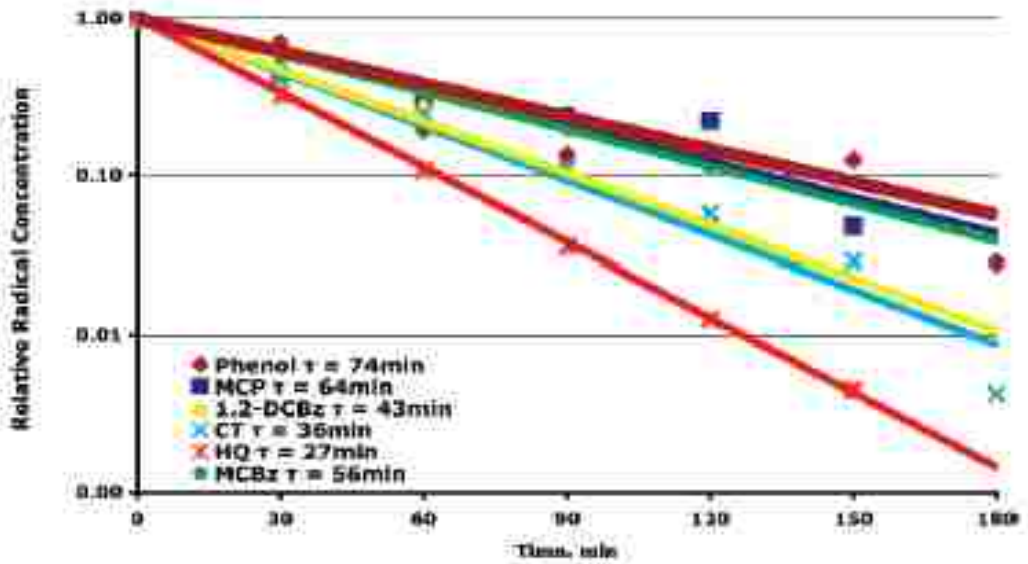

Figure 2.7 Decay rates of radicals formed on 5% CuO/SiO_2 [8].

2.4.2 X-ray Absorption Near Edge Structure

X-ray absorption spectroscopy (XAS) has generally been used to study a number of bulk solid-state materials. It gives information regarding oxidation states and local structure of materials. With high intensity tunable light sources such as synchrotrons now available, small concentrations can be analyzed. This is particularly useful when the elements of interest constitute only a small fraction of a complex system under investigation. Another advantage XAS has is that samples do not have to be crystalline. The material can be amorphous. It can also be in either solid, liquid or gas phases. Mostly XAS is used to study metals with high element specificity; XAS is capable of looking at metals of choice in a sample that may contain numerous other materials [9, 10]. Therefore, XAS is a useful technique to monitor the chemistry that takes place at metal sites in a sample including EPFRs. However, XAS usually refers to both XANES and a complementary measurement known as extended x-ray absorption fine structure (EXAFS). I will focus only on XANES.

With highly tunable x-ray sources, the XANES signal comes from the atoms of a single element in a complex mixture [9, 10]. Tuning the photon energy is usually done using a crystalline-based monochromator in the energy ranges of 0.1-100 keV. X-ray absorption occurs when the impending photon causes a core electron to be excited to some higher energy unoccupied state or the continuum. If the electron transitions to a bound unoccupied state and either it or another electron relaxes filling the vacancy emitting a photon this creates a distinct peak.

The electron being excited to the continuum of states creates the edge signal and the edge is defined as the ionization threshold. The names of the shells are traditionally called K, L-III, L-II, L-I and so on [9, 10].

When the excited electron transitions back to the ground state releasing energy in the form of photons this is known as fluorescence. These photons can then be measured using a variety of different detectors. The excited electrons can only access certain upper level orbitals as dictated by selection rules, which come from quantum mechanics. The selection rule that dictates electronic transitions says that the electron can only be excited to a state that differs in orbital angular momentum (Δl) by ± 1 [10]. Not only can fluorescence occur when the excited electron drops back to the ground state, but other non-radiative processes occur too. Another process that occurs is known as the Auger effect. The Auger effect occurs when the excited electron is ejected from the atom creating a core hole. Another electron then relaxes to fill the vacancy releasing energy causing an outer electron to be ejected, but is not detected in XAS. The Auger effect can be thought of as an electron scattering event and can occur in many different configurations with regard to the shells involved. Since it requires three electrons to occur elements below lithium do not exhibit the Auger effect. The Auger effect is predominant in light elements ($Z<30$) for K level transitions while fluorescence is the preferred emission for heavier elements ($Z>30$) [11]. The reason for this trend is because of the transition probability, which is proportional to the dipole matrix for x-ray fluorescence. The magnitude of the matrix elements is proportional to Z^2. Therefore at low Z, fluorescence has a rather low efficiency

making the Auger process more favorable [11]. The energy level diagram illustrating the Auger process and fluorescence is shown figure 2.8.

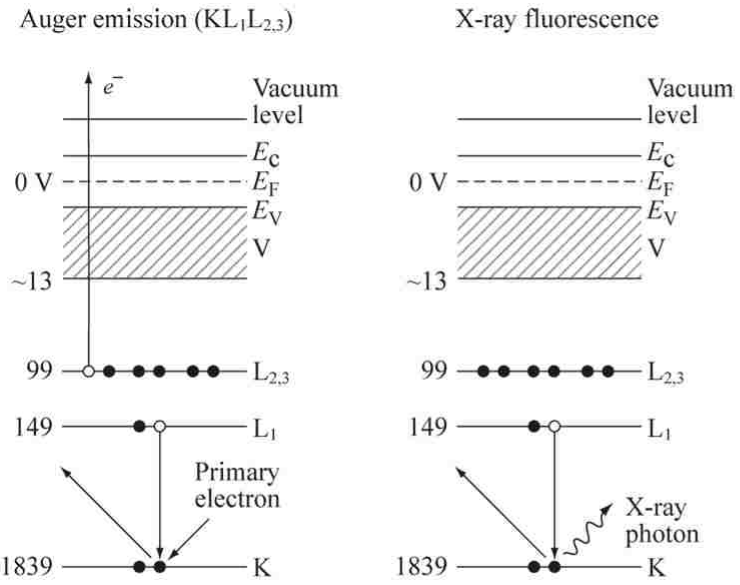

Figure 2.8 An energy level diagram illustrating the Auger process and X-ray fluorescence [12].

A typical XANES spectrum is usually coupled with an EXAFS spectrum. The XANES portion is collected from 200 eV below the edge to approximately 1000 eV above the edge of the element of interest. A general XANES and EXAFS spectrum is shown in figure 2.9.

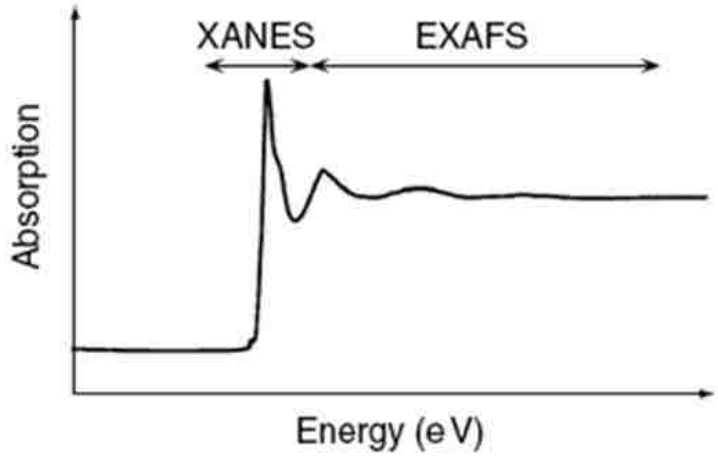

Figure 2.9 Example XANES and EXAFS spectrum [13].

XANES data provides information regarding oxidation states and some data on local environment of a specific element. In K-edge XANES a 1s electron is excited to an upper level p-orbital as dictated by the selection rules (1s ➔ (n)p). Occasionally, a transition occurs to a d-orbital (1s ➔ (n-1)d). The intensity of these transitions are relatively week because the probability of occurrence is very low, however, it is non-zero. These transitions are called quadrupole transitions ($\Delta l = \pm 2$) and are selection rule forbidden [9]. Therefore, the XANES spectrum is a way to probe the density of states of a system.

In a XANES experiment, spectra of standards of a known oxidation state are collected and compared to the spectrum of the sample. Usually, the higher the oxidation state, the higher the energy required to excite the 1s electron. This can be thought of in terms of simple coulombic charges. The higher the positive charge on an atom (oxidation state), the attraction on the remaining electrons of the atom increases. This causes the necessity for higher photon energies to excite the remaining electrons. Figure 2.10 shows example spectra of the different oxidation states of copper with the main peak being a distinct 1s ➔ 4p transition [14]. The peak occurs at lower energy for Cu(0) than for either Cu_2(I)O or Cu(II)O. This type of trend holds true for other elements as well.

Not only can XANES help with identifying oxidation states, but it also help determine if a mixture of oxidation states exist in the same sample. By collecting the spectra of standards, linear combination fitting (LCF) can be performed to help determine the percentages of particular oxidation states present in the sample. LCF is done by multiplying the spectra of standards by a certain

percentage and adding them together to produce a best fit to the experimental spectrum. XANES can therefore be a useful tool to help determine the electronic structure of EPFR precursors as they interact with metal oxides due to its high element specificity, high intensity of the light sources, and its ability to examine powder samples. If the EPFR precursor does affect the oxidation state of the metal by electron transfer, then XANES would be able to measure such processes. A previous study using XANES was done to show the interactions between dioxin precursors and Cu(II)O. Farquar *et al.* demonstrated that when a dioxin precursor (2-monochlorophenol) reacted with Cu(II)O, the oxide was reduced to Cu(I) from a one electron transfer [15].

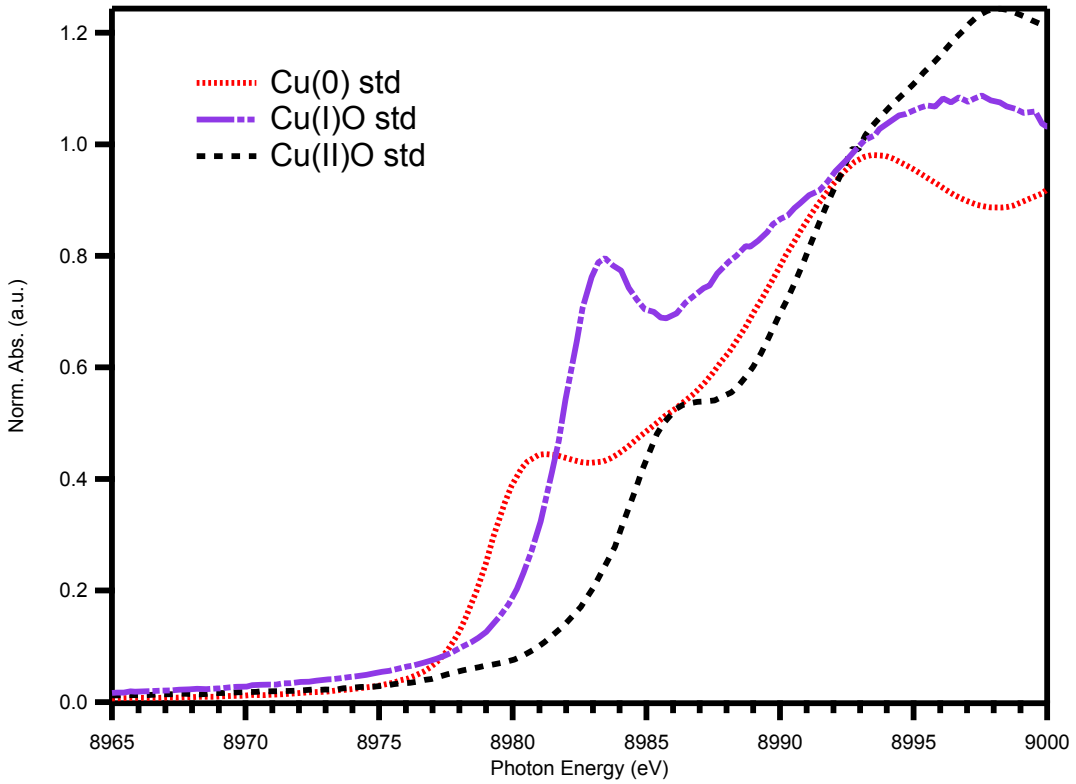

Figure 2.10 Example XANES spectra of copper standards of varying oxidation states.

Principal component analysis (PCA) can be used to determine the minimum number of standards (components) that are needed to regenerate the experimental spectrum within statistical error. PCA assumes the experimental spectrum is a linear sum of individual components that correlate to the species present in the sample. PCA uses linear algebra to output eigenvectors and eigenvalues to reconstruct the experimental spectrum. If a particular standard is not a component of the sample then the spectrum cannot be reproduced [16].

2.5 X-ray Fluorescence Spectroscopy

For our experiments we used a FEI Quanta 3D FEG Dual Beam SEM/FIB microscope with an EDS attachment, which is equipped silicon drift detector located at the LSUMCC. Samples were also submitted to Bruker to be analyzed on the S2 Picofox XRF spectrometer. We used X-ray fluorescence to examine the ratio of Cl to Cu when Cu(II)O nanoparticles were dosed with chlorinated EPFR precursors. This is to measure how many radicals per metal ion formed. This would also give information regarding the nanoparticle's 3D structure and the nature and reactivity of the surface of our nanoparticles.

X-ray fluorescence is one of the most traditional spectroscopic techniques in the x-ray regime [11]. Fluorescence spectra are obtained by photoionization of core shell electrons. This in turn creates an interior hole that can be refilled by recombination with electrons from higher energy levels. This recombination can either radiate photons or be non-radiative by an Auger process [11].

Transitions from the valence shells to the inner shells are dominated by dipole transitions. These transitions are unique to each element, which makes x-

ray fluorescence an excellent tool for chemical analysis. The inner shell hole can be generated with either x-ray photons from a light source or with electrons [11]. Excitation with x-rays gives the advantage of probing greater depths of materials and the irradiation can be done under ambient conditions. Electron excitations need high vacuum to operate; therefore, most systems are attached to high-resolution electron microscopes that use high vacuum and often are called energy dispersive spectroscopy (EDS). Unlike UPS and EELS, x-ray fluorescence can be used to measure powder samples such as our Cu(II)O nanoparticles.

2.6 Surface Science Methods

Most previous studies regarding EPFRs have been done using powder samples. Metal oxides supported on silica, alumina, or titania are synthesized to mimic fly ash (large mixture of different metal oxides). This is because combustion systems are very complex. Each component is studied separately to understand contributions to the whole system and to make experiments simple. Therefore, surrogates are made. EPFR formation occurs at the surface of metal oxides. To study the micro and electronic structures of EPFRs it may be better to apply a surface science approach. Traditional surface science methods, however, work better with single crystals and not powder amorphous samples. In principle, metal oxide single crystals can then be used as a model system for powders. Besides working well with established surface science methods, single crystals offer an advantage to powders in that crystallographic face dependent information can be obtained. For example, ZnO has only three

thermodynamically favorable crystal faces [17]. One is a non-polar surface known as ZnO(10$\underline{1}$0) and the other two are polar ZnO(0001) surfaces. The polar surfaces can have either all oxygen or all zinc atoms at the surface. By observing the different interactions of EPFR precursors with different faces of the same material, more details regarding the micro and electronic structures of EPFRs and can be obtained.

2.6.1 Low Energy Electron Diffraction

After a single crystal sample has been cleaned and gases are adsorbed, it becomes useful to examine the surface symmetry and ordering. This ensures three things: the surface cleanliness, the surface is of the correct symmetry for the experiment, and if an adsorbed gas orders in a particular way. To examine the surface symmetry and adsorption ordering low energy electron diffraction (LEED) is used. Figure 2.11 shows a generic diagram of a typical LEED setup.

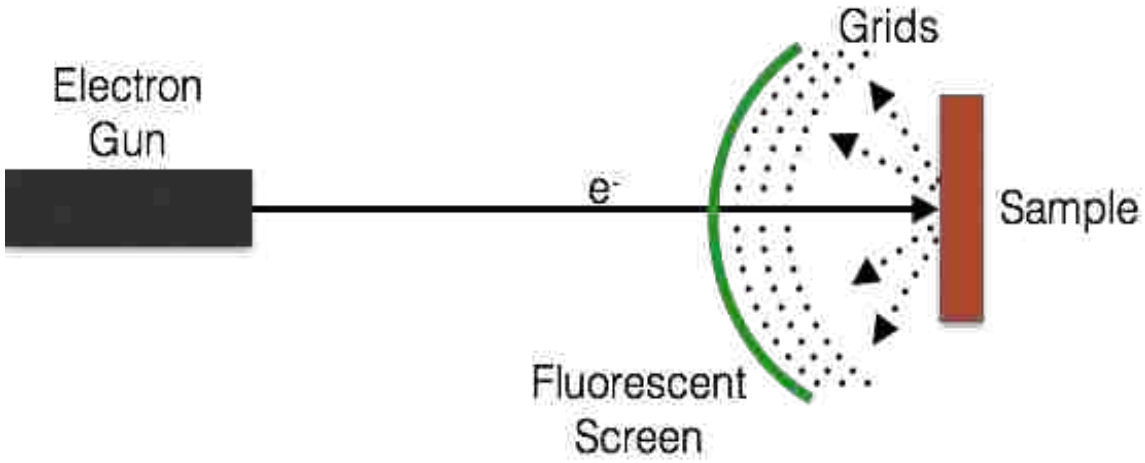

Figure 2.11 A general diagram of a LEED system.

Electrons are emitted from an electron gun and are accelerated by the grids anywhere from 10 – 500 eV kinetic energy before striking the sample at the center. The electrons interact with the topmost surface atoms, which diffract and backscatter hitting a fluorescent screen revealing a pattern of the reciprocal lattice of the surface [2]. Since electrons can be viewed as either particles or waves, LEED is best understood from the wave nature of the electron. If someone wished to calculate the spacing between the atomic planes, one can do so using two equations. The first is using de Broglie's wavelength equation given by:

$$\lambda = \frac{h}{p} = \frac{h}{\sqrt{2mE}} \tag{2.11}$$

where λ is the wavelength, h is Plank's constant, p is the electron momentum, m is the electron mass, and E is the kinetic energy of the electron. LEED owes its surface sensitivity to the large cross section of inelastic scattered electrons. When electrons interact with the surface, they do so mainly with the collective excitations of the valence electrons (i. e. plasmons). The electrons in the correct energy range have a small mean free path. This means that all the elastically scattered electrons come from the first few atomic layers of the crystal [2]. For example, if electrons from 20 - 500 eV are used, this calculates to wavelengths of 0.27- 0.05 nm using equation 2.11. Effectively, this makes the mean free path to be a minimal 5 – 15 Å making LEED very surface sensitive. For our experiments we used a SPECS ErLEED 100 kept at a base pressure of 10^{-10} Torr. The chamber that houses the LEED is also equipped with several standard leak valves that allow us to introduce precise amounts of several different gases after

which a LEED can immediately be recorded. The LEED chamber is also attached to an x-ray photoelectron spectroscopy chamber that was not used in our studies. The second equation needed is for calculating atomic spacing is Bragg's law. Bragg's law is given by the following simple equation:

$$n\lambda = dsin\theta \tag{2.12}$$

where n is an integer, d is the spacing between atomic planes, and θ is the angle between the incident light and the scattering planes. It should be noted that these equations do not always give definitive atomic spacing. Contaminants can create superstructures on a surface making the calculation erroneous [2, 3].

LEED in general is used more qualitatively than quantitatively. Qualitatively, LEED can help determine the symmetry of the surface by simply looking at the diffraction pattern. For example, in figure 2.12 is the LEED of a clean ZnO(10$\bar{1}$0). The cleanliness of the sample can also be determined by simply observing the pattern. In general, if the surface is clean then the diffraction spots should be sharp and well defined with low background intensity [3].

Even though with LEED it is easier to make qualitative determinations, it is not impossible to quantitatively determine the structure. It is however difficult. To determine the structure of a surface by LEED one has to measure the intensity of the spots as a function of beam energy. Then using multiple scattering theory, models can be constructed and compared to the measured results. This task is very intensive and beyond the scope of this work.

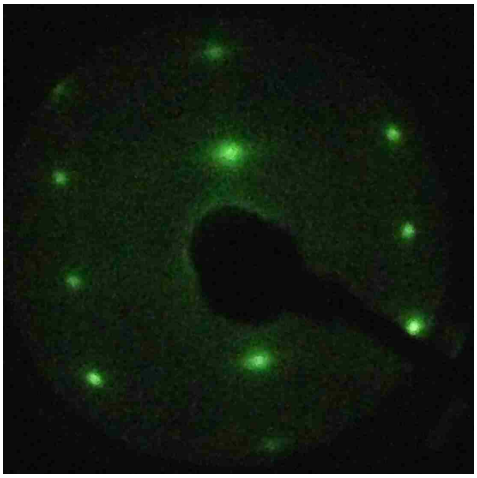

Figure 2.12 A LEED pattern of clean ZnO(10$\bar{1}$0).

2.6.2 Ultraviolet Photoelectron Spectroscopy

Photoelectron spectroscopy in general has become the go to technique to analyze the electronic structure of materials especially single crystals. As the name implies photoelectron spectroscopy relies on the phenomenon known as the photoelectric effect. The photoelectric effect occurs when a material is exposed to light and electrons are emitted. Heinrich Hertz was one of the first to observe this phenomenon in 1887, but it wasn't until Albert Einstein in 1905 that a theoretical basis was established. Einstein used Plank's concept of quantized energy to derive a relationship between the energy of incident light and the emitted electron's kinetic energy.

$$KE = h\nu - \Phi \tag{2.13}$$

In equation 2.13 KE is the kinetic energy, ν is the frequency of light, and Φ is the work function. The work function is the minimum amount of energy required to eject an electron from a particular material. If the light's energy is greater than the work function then electrons are still ejected regardless of the light's intensity.

However, if the light's energy is less than the work function no electrons are ejected regardless of intensity. This simple theoretical framework had a dramatic and profound impact on early quantum theory. Namely, that energy from light cannot have continuous and arbitrary values. Rather, it comes in discrete units on the order of *h* (Plank's constant).

In practice, equation 2.13 is not enough to determine the electronic structure of materials. Rather, the process is a little more complex. Equation 2.13 can be modified to yield a new equation.

$$KE = h\nu - BE - \Phi \tag{2.14}$$

The new term BE in equation 2.14 is simply the binding energy of the electron before the photoemission process. The binding energy is the important term since it contains information regarding the nature or behavior of the electrons in the material that comes from the interactions with nuclei and other electrons. From equation 2.14 it is clear that photoelectron spectroscopy only measures the occupied states (below the Fermi level) [3]. The Fermi level is defined as the most energetic electrons at 0 K. At 0 K they pack the lowest available energy states. This also means they have the lowest binding energy such that the photoelectron spectrum is zeroed to the Fermi level. Experimentally, to measure the binding energy three things become critically important. One is that a source of photons with a known energy is required. Second, the electrons that are ejected have to be measured. Thirdly, the work function has to be determined [3].

The energy of the incident photons determines the type of photoelectron spectroscopy being performed. If higher energy x-rays are used then x-ray photoelectron spectroscopy (XPS) is performed. If lower energy ultraviolet photons are used then ultraviolet photoelectron spectroscopy (UPS) is used. Using higher energy x-rays means that core electrons are ejected for XPS measurements. However, for UPS the valence electrons are the ones ejected. UPS can measure the electronic structure of solids and map out band structure with detailed angle dependence measurements. The other advantage UPS offers, is that it is extremely useful to study adsorbed molecules on surfaces [2]. This is due to its surface sensitivity (discussed below). Theoretical calculations are also employed to examine the participating orbitals by mapping the density of states (DOS). This gives insights as to what orbitals are participating in bonding and to examine charge transfers between molecules and the solid surface. UPS is also a method to examine work function changes that occur when a molecule adsorbs to a surface. The other advantages UPS has over XPS is that the line widths of UPS sources are very narrow and the photon flux of UV sources is also much higher. Therefore with UPS, the electronic structure of surface bound EPFRs can be obtained.

Ultraviolet radiation can be provided by either gas discharge lamps, synchrotrons, or non-linear processes from lasers [2, 18]. Synchrotrons function using high energies on the order of a few GeV.

Synchrotrons operate by accelerating charged particles to relativistic speeds. These particles are forced to orbit in a circular path and are steered using powerful magnets. These magnets bend the particles and at each bend electromagnetic radiation is emitted at all wavelengths. Therefore, each beamline (which are connected to the bending magnets or other insertion devices such as undulators) must be equipped with a monochromator to select the wavelength needed for particular experiments. Synchrotrons offer several advantages over simple discharge lamps. Mainly, the photon flux is orders of magnitude higher than discharge lamps. For synchrotron sources the photon flux can be anywhere from 10^{15} – 10^{17} photons/s compared to discharge lamps, which average roughly 10^{12} photons/s [2, 18]. The other advantage is that synchrotrons have high tunability over large spectral ranges. This means that cross-sections can be maximized for a particular electronic state. With higher photon flux and tunability, resolution increases. Synchrotron light is also polarized allowing other experiments to be performed [2, 3, 18]. The disadvantages of synchrotrons are that they are large, expensive, and have limited user availability.

For this work, UPS was conducted at the 5-meter toroidal grating monochromator (5m-TGM) beamline located at the Center for Advanced Microstructures and Devices (CAMD). Detailed information about the beamline is described elsewhere [19]. A schematic of the beamline with flux curves for each grating are shown in figure 2.13.

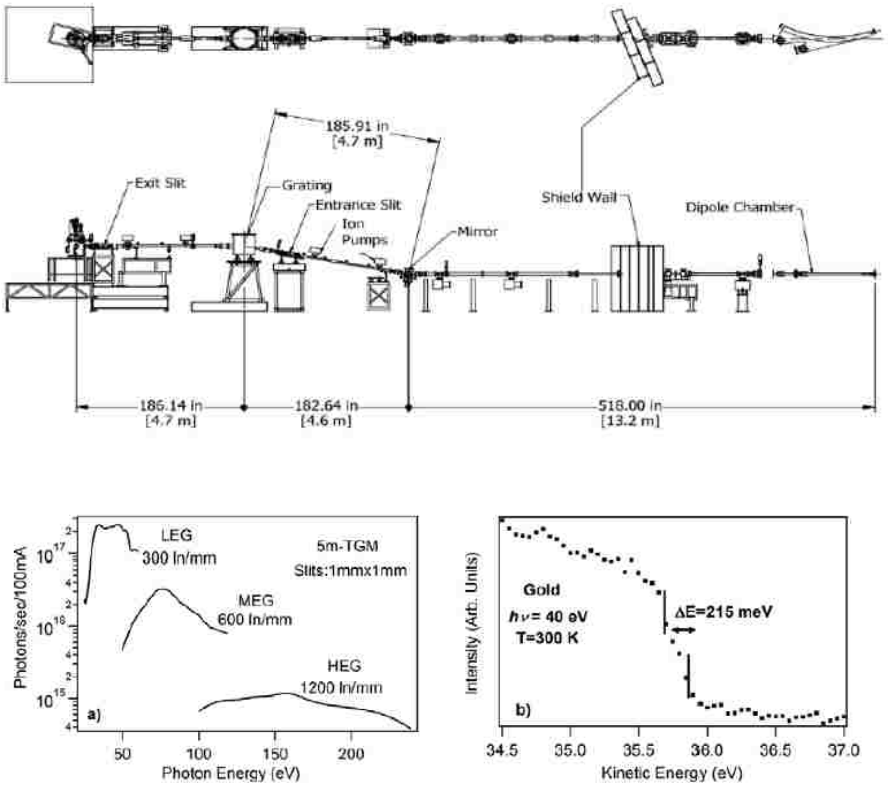

Figure 2.13 A schematic of the 5m-TGM at CAMD with flux curves for each monochromator grating [19].

The next experimental parameter for photoemission is that the kinetic energy of the ejected electrons has to be measured. Typical energy analyzers for UPS are operated in conjunction with a lens system like in figure 2.14. Samples are usually mounted on some sort of manipulator whose angle relative to the analyzer can be adjusted. This is useful in defining the polar and azimuthal angle of electron emission. Also by having the sample rotatable one could take advantage of polarized light sources. Two electrostatic hemispherical deflectors perform the analysis of the electron's kinetic energy. Each hemisphere has a fixed radius and negative potentials are applied to both hemispheres. Electrons with a specific energy will have the correct trajectory to make it all the way to the

multiplier and be detected. Since the radii of the hemispheres are fixed and the negative potentials can be varied to allow electrons with different kinetic energies to pass and be detected. However, changing the potentials of the hemispherical analyzer is not often done because varying the potentials changes the absolute resolution depending on the energy of the incident light. To correct for this problem a lens system is put into place that either accelerates or retards incoming electrons to a fixed energy called the pass energy [19]. This allows the resolution to be maintained independent of the incident light energy that is used for the measurement. A diagram of a hemispherical analyzer with a lens system is shown in figure 2.14.

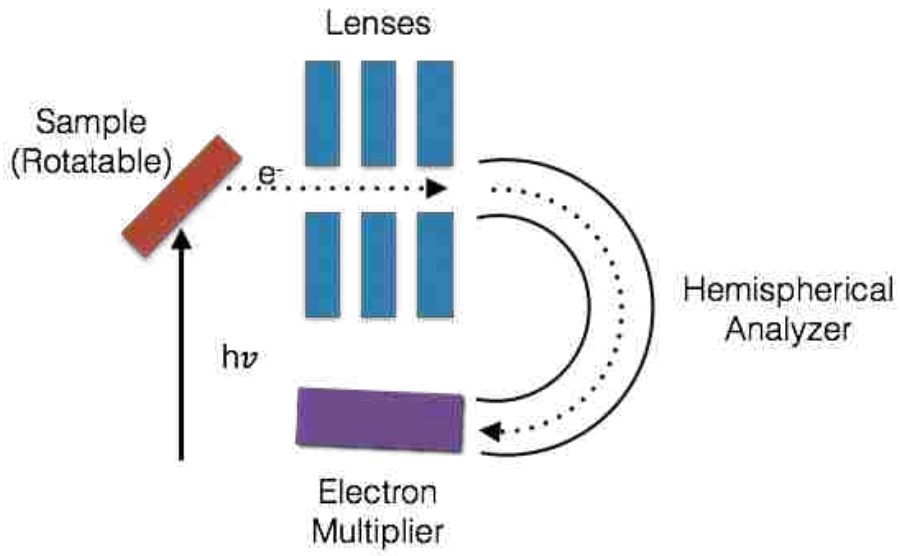

Figure 2.14 A diagram of a hemispherical electron energy analyzer with a lens system.

The third parameter for a solid-state photoelectron spectroscopy experiment is the work function. The work function again is the minimum amount of energy required to eject an electron from a material. Looking at equation 2.14,

it is easy to assume that the work function in question is the sample's (Φ_s). Therefore, we need to measure the work function of every sample to have a successful experiment. However, this is not true [18, 20]. The channeltron inside the analyzer also has a work function simply called the analyzer work function (Φ_a). These two work functions are connected electrically through the sample holder and cables of the system producing a contact potential of Φ_s - Φ_a. The two Fermi levels become equilibrated. As a consequence of the contact potential, the kinetic energy of the electrons rushing through the analyzer are accelerated by the same magnitude as the potential. This means that equation 2.14 can be rewritten as follows:

$$KE = h\nu - BE - \Phi_s + \Phi_s - \Phi_a \qquad (2.15)$$

$$KE = h\nu - BE - \Phi_a$$

Equation 2.15 illustrates that only the analyzer work function is needed and not the sample work function. This holds true if the sample and analyzer Fermi levels are aligned. If a potential difference exists between the two, then this simplistic picture will no longer be true. This is especially the case if samples are not conductive enough and cannot regenerate the lost charge when electrons are ejected. This results in inaccurate binding energies [3].

Since we are doing surface science experiments, a question may arise about the surface sensitivity of UPS or of electron spectroscopies in general. Electron spectroscopies including UPS obtain surface sensitivity from the short mean free path of electrons [18]. Generally speaking, the electron's mean free path

is determined mainly by its kinetic energy. In figure 2.15 is a plot of the "universal" mean free path of the electrons in a solid for several elements.

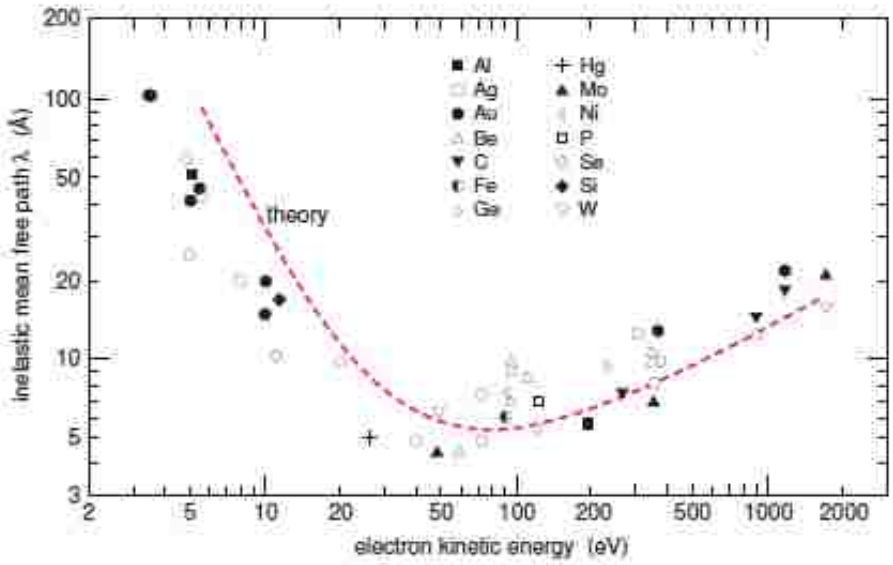

Figure 2.15 The universal mean free path of electrons in a solid [18].

As shown in figure 2.15, the mean free path has a broad minimum centered at approximately 70 eV kinetic energy. This means if an electron escapes the material with this amount of kinetic energy, then it originated from the first few atomic layers (<10 Å). Most photoemission experiments access kinetic energies anywhere between 10 – 2000 eV. This means that we can change the surface sensitivity just by changing the kinetic energy of the electrons.

Another consequence of the mean free path is that electrons that escape the surface before a scattering event takes place will originate within the first tens of angstroms of the material's surface. Electrons located in the bulk will undergo scattering events thereby losing energy. They still escape the surface, but rather

than having distinct peaks, the electrons from the bulk give rise to a broad background referred to as a secondary electron background.

2.6.3 Electron Energy Loss Spectroscopy

In our experiments we used EELS to measure interband transitions of adsorbate molecules on the surface of metal oxides. The LK2000 spectrometer used for our experiments has been described in detail elsewhere [21]. The spectrometer has the capability of providing beam energies from 1-240 eV. In this work we consistently used a beam energy of 30 eV with a resolution of ~15 meV. The incident and exit angles of electrons were both held constant (30°) with respect to the sample normal.

Electron energy loss spectroscopy (EELS) is another highly surface sensitive technique that can be employed to probe the physical and chemical properties of surfaces. EELS can be used to measure both vibrational and electronic transitions. The technique uses a monoenergetic beam of electrons strike the surface at a fixed angle. The electrons scatter in various ways at the surface with most electrons undergoing elastic scattering meaning no energy is lost. Some of the electrons undergo inelastic scattering and transfer some of their energy to excitations at the surface (phonons, vibrations of adsorbed molecules, electronic transitions, etc.) [2]. The kinetic energy of the electrons scattered in a certain direction are then measured and plotted as intensity of electrons that are scattered versus the energy loss. A schematic of an EELS spectrometer is shown in figure 2.16.

In an EELS experiment, the incident electron energies can be adjusted depending on the transitions of interest. Beam energies can range from a few eV to hundreds of eV with energy losses measured between meV to eV. Two mechanisms are generally considered when discussing EELS. These are the dipole scattering (long-range) and impact scattering (short range). These two mechanisms apply to vibrational EELS, which was not used in our experiments. The electron energy is enough to only penetrate the first few layers of the material [2]. This makes it a valuable surface science technique. Unlike UPS, which only measures occupied states below the Fermi level, EELS examines the energy gap between occupied states and unoccupied states. Using UPS in conjunction with EELS can give valuable information regarding the complete electronic structure of EPFRs as they interact with surfaces.

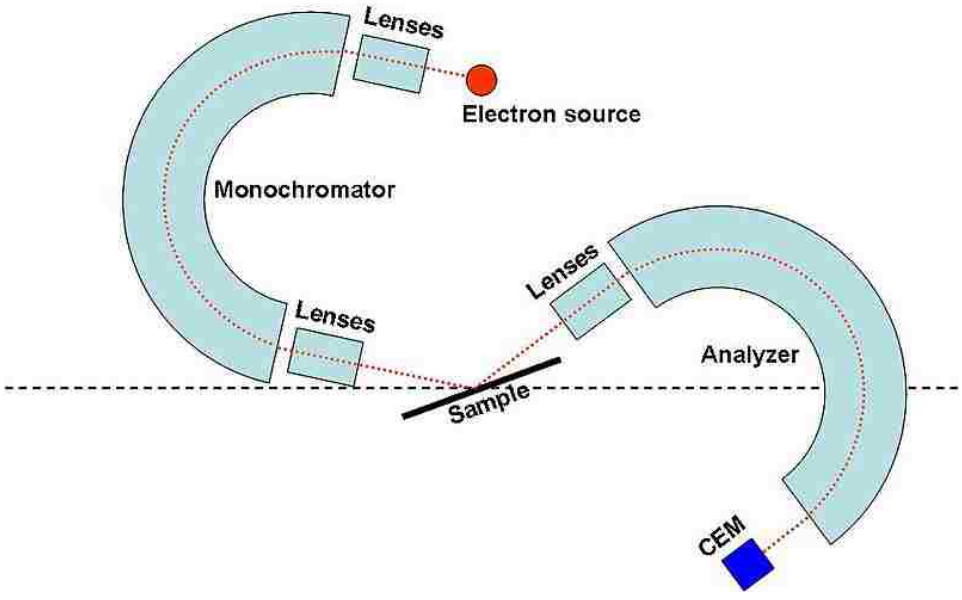

Figure 2.16 A schematic of an EELS spectrometer.

2.7 References

(1) Atkins, P.; de Paula, J. *Physical Chemistry,* 7th ed.; New York, 2002.

(2) Ibach, H. *Physics of Surfaces and Interfaces*; Springer: New York, 2003.

(3) Patterson, M. C. Single-Crystal Metal Oxides and Supported Metal Nanoclusters as Model Catalyst Systems. Ph.D. Dissertation [Online], Louisiana State University, Baton Rouge, LA, April 2013. http://etd.lsu.edu/docs/available/etd-04072014-160705/ (accessed Jun 2, 2014).

(4) Lomnicki, S. M.; Wu, H.; Osborne, S. N.; Pruett, J. M.; McCarley, R. L.; Poliakoff, E.; Dellinger, B. Size-Selective Synthesis of Immobilized Copper Oxide Nanoclusters on Silica. *Mat. Sci. Eng. B* **2010**,175(2), 136–142.

(5) Rodrigo, U. I. Geometrical and Electronic Structure of Metal Oxide Nanoparticles on Silica and Alumina. Ph. D. Dissertation, Louisiana State University, Baton Rouge, LA, 2012.

(6) EPR: Introduction. http://chemwiki.ucdavis.edu/Physical_Chemistry/Spectroscopy/Magnetic_Resonance_Spectroscopies/Electron_Paramagnetic_Resonance/EPR%3A_Introduction. (accessed April 9, 2014).

(7) EPR Facility. http://epr.cm.utexas.edu/WhatIsEPR.html. (accessed April 9, 2014).

(8) Lomnicki, S.; Truong, H.; Vejerano, E.; Dellinger, B. Copper Oxide-Based Model of Persistent Free Radical Formation on Combustion-Derived Particulate Matter. *Environ. Sci. Technol.* **2008**, *42*, 4982–4988.

(9) Kelly, S. D.; Hesterberg, D.; Ravel, B. In Methods of soil analysis, Part 5: Mineralogical methods; Ulery, A. L.; Drees, L. R., Eds.; Soil Science Society of America: Madison, WI, 2008, p 367− 463.

(10) University of California, Davis, XAS: Application. http://chemwiki.ucdavis.edu/Physical_Chemistry/Spectroscopy/X-ray_Spectroscopy/XAS%3A_Theory (accessed April 11, 2014)

(11) Kuzmany, H. *Solid-State Spectroscopy: An Introduction*. Springer-Verlag: Berlin, 1998.

(12) Glossary of Nanotechnology and Related Terms. Auger Electron Spectroscopy. http://eng.thesaurus.rusnano.com/wiki/article2003 (accessed March 9, 2015).

(13) Medjo, R. E. Characterization of Carbon Nanotubes. In *Physical and Chemical Properties of Carbon Nanotubes*; Suzuki, S., Ed.; InTech: 2013.

(14) Kau, L.-S.; Spira-Solomon, D.; Penner-Hahn, J. E.; Hodgson, K. O.; Solomon, E. I. X-Ray Absorption Edge Determination of the Oxidation State and Coordination Number of Copper: Application to the Type 3 Site in *Rhus Vernicifera* Laccase and Its Reaction with Oxygen. *J. Am. Chem. Soc.* **1987**, *109*, 6433–6442.

(15) Farquar, G. R.; Alderman, S. L.; Poliakoff, E. D.; Dellinger, B. X-Ray Spectroscopic Studies of the High Temperature Reduction of Cu(II)O by 2-Chlorophenol on a Simulated Fly Ash Surface. *Environ. Sci. Technol.* **2003**, *37*, 931–935.

(16) Gaur, A.; Shrivastava, B. D. A Comparative Study of the Methods of Speciation Using X-Ray Absorption Fine Structure. *Acta. Physica Polonica A* **2012**, *121*, 647–652.

(17) Woll, C. The Chemistry and Physics of Zinc Oxide Surfaces. *Progress in Surface Science* **2007**, *82*, 55–120.

(18) Hofmann, P. *Surface Physics: An Introduction*; Wiley-VCH: Weinheim, 2013.

(19) Kizilkaya, O.; Jiles, R. W.; Patterson, M. C.; Thibodeaux, C. A.; Poliakoff, E. D.; Sprunger, P. T.; Kurtz, R. L.; Morikawa, E. High-Throughput Toroidal Grating Beamline for Photoelectron Spectroscopy at CAMD. *J. Phys.: Conf. Ser.* **2014**, *493*, 012024.

(20) Chusuei, C.; Goodman, D. X-ray Photoelectron Spectroscopy. In *Excyclopedia of Physical Science and Technology,* 3rd edition.;Meyers, R., Eds.; Academic Press: New York, 2002; 921-938.

(21) Wang, F. Structural and Electronic Properties of Noble Metals on Metal Oxide Surfaces. Ph.D. Dissertation [Online], Louisiana State University, Baton Rouge, LA, August 2011. http://etd.lsu.edu/docs/available/etd-07052011-104558/unrestricted/wangdiss.pdf (accessed Nov 3, 2014).

Chapter 3
Probing Environmentally Significant Surface Radicals: Crystallographic and Temperature Dependent Adsorption of Phenol on ZnO

3.1 Introduction

The adsorption of aromatic molecules on metal oxide surfaces continues to attract attention due to their potentially significant environmental impacts [1-4]. In particular, recent experiments have demonstrated that when certain classes of substituted benzenes chemisorb to metal oxide surfaces, such as ZnO, environmentally persistent free radicals (EPFRs) are formed. EPFRs are thermally activated radicals with half-lives of hours to days under ambient conditions and indefinitely under vacuum [5-9]. The term EPFR refers to these composite organic/metal oxide pollutant particles. Specifically, ZnO is known to form the longest-lived EPFRs with half-lives up to 73 days based on EPR results where g-values are consistent with aromatic type radicals [7]. Previous *ab initio* calculations associate this exceptional stability and low reactivity to a resonance stabilization including both oxygen and carbon-centered radicals [10]. The association of EPFRs with toxic airborne particulate matter is important because they pose serious health consequences to humans [11-20]. Developing a detailed model of the mechanism of EPFR formation on metal oxides is a necessary first step in understanding their toxicity and in guiding strategies for remediation.

To gain key insights into real world systems we employ a model system to mimic a key step in EPFR formation, namely, the temperature-dependent chemisorption of phenol on well-defined ZnO surfaces. Because single crystal ZnO has few low-energy crystallographic faces, [21, 22] this is an ideal model system to obtain comprehensive information that closely represents nanoparticle powder samples, which have been used in previous studies [4-8].This study aims to understand the detailed atomic and electronic structure of EPFRs formed on two differing ZnO crystallographic faces namely the (10$\underline{1}$0) and (000$\underline{1}$)-Zn surfaces. Our experimental data strongly suggests that upon adsorption of phenol, a known EPFR precursor, there is a charge transfer away from both ZnO surfaces toward the phenol, which is inconsistent with a previously proposed mechanism of EPFR formation [23]. Moreover, surface spectroscopic data, which probe the electronic properties of the adsorbed phenol, reveal that there is a significant difference between adsorption at room temperature versus elevated temperatures for the (000$\underline{1}$) surface only. Additionally, employing surface diffraction, we show that the adsorption of phenol (10$\underline{1}$0) surface results in a semi-ordered atomic superstructure.

To date, only generic mechanisms that lack atomistic details have been proposed for EPFR formation on metal oxide surfaces [5, 6, 24]. The mechanisms consist of an initial chemisorption of the EPFR precursor molecule, typically alcohol or halogenated aromatic systems, to the surface followed by elimination of water or HCl and consequent charge transfer between the molecule and metal oxide surface.

During this latter activated process, a concurrent reduction of the metal and EPFR formation occurs. In this context, interactions between phenol and ZnO become interesting because of the limited stable oxidation states of Zn (a +1 state is non-existent). This motivates the importance to understand the atomic and electronic structure in detail. Furthermore, our studies can be used by theorists as a guidepost to aid in developing a clearer picture of the interactions between aromatic organics and transition metal oxides taking into account both morphology/symmetry and electronic details.

In this study, we perform low energy electron diffraction (LEED), electron energy loss spectroscopy (EELS), and ultraviolet photoelectron spectroscopy (UPS), of phenol adsorbed at low temperature (90 K), room temperature, and at 220 °C on non-polar ZnO(10$\underline{1}$0) and polar ZnO(000$\underline{1}$)-Zn/(0001)-O single crystal surfaces as surrogate model systems for EPFR formation. Using UPS we were able to observe band bending toward the Fermi level indicating charge transfer from the ZnO surfaces to the phenol at both room temperature and 220 °C, which differs from previously proposed EPFR formation mechanisms. Moreover, EELS measurements are used to probe low-energy electronic transitions of chemisorbed phenol as a function of temperature to complement the UPS measurements. The UPS and EELS measurements together reveal that the phenyl ring of phenol chemisorbed on (10$\underline{1}$0) likely remains intact and the phenol chemisorbed to the (000$\underline{1}$)-Zn shows significant changes that indicate that EPFR formation may favor the Zn-terminated surfaces.

The LEED measurements also show significant differences between the adsorbate atomic structure arrangements on surfaces. On the (10$\underline{1}$0) surface chemisorbed phenol forms a semi-ordered superstructure while phenol on the (000$\underline{1}$)-Zn surface is completely disordered.

This investigation is part of a larger program to study EPFR precursors on transition metal oxides. It is clear from the results that will be presented that the simple unverified mechanism does not describe all systems where EPFRs are known to form, although recent experimental studies have demonstrated charge transfer from the adsorbed organic species to the metal oxide in the direction proposed by the generic mechanism [23]. Experimental and theoretical studies are required to generate insights into other EPFR/metal oxide systems and this study can help those who are interested in such systems. By performing detailed studies of the atomic and electronic structure of such systems a clearer picture maybe obtained to understand how each system behaves individually, highlighting their similarities and their differences.

3.2 Materials and Methods

All experiments were performed in ultra-high vacuum (UHV) systems with base pressures below 2×10^{-10} Torr. ZnO(10$\underline{1}$0) and ZnO(000$\underline{1}$)-Zn samples (10x10x1 mm) were purchased from MTI Corporation and cleaned in UHV by several cycles of 1.5 keV Ne ion bombardment at 5×10^{-5} Torr for 45 min. followed by 30 min. annealing at 650 °C.

EELS spectra were taken before dosing with phenol to ensure cleanliness of the sample wherein only phonons and bulk band gap (~3.7 eV) features were identified. Adsorption of the EPFR precursor was accomplished by introducing phenol vapor into the vacuum chamber using a standard leak valve. The phenol was purified by several freeze-pump-thaw cycles. For dosing at elevated temperatures, the respective crystal was brought to a given temperature in vacuum as measured with a type K thermocouple. After cooling to room temperature, the data was acquired. The EELS measurements, using a LK2000 EELS spectrometer employed a primary beam energy of 30 eV with a resolution of ~ 15 meV (measured by the FWHM of the elastically scattered electron beam in the specular direction) in specular geometry. When dosing at low temperature, the samples were exposed and spectra were collected while the sample was held at ~ 90 K. All EELS spectra were normalized to the height of the elastic peak.

All UPS measurements were performed using the 5-meter toroidal grating monochromator (5m-TGM) beamline and UPS endstation at the Center for Advanced Microstructures and Devices (CAMD) at Louisiana State University, which is described in detail elsewhere [25]. A 50mm hemispherical analyzer was used to acquire the normal emission spectra with 40 eV photon energy and 45 degree incident light. The Fermi edge was determined from the sputtered copper sample holder.

The electronic structure of phenol was calculated using WIEN2k with a unit cell of 15x14x10 Å, ensuring enough vacuum space that the molecules are essentially isolated. Exchange-correlation potential was used and the revised GGA of Perdew–Burke–Ernzerhof and the molecule was allowed to fully relax [26].

3.3 Results

Figure 3.1 shows the photoelectron spectra of phenol dosed at 220 °C on non-polar ZnO(10$\underline{1}$0) (Fig. 3.1e), polar (000$\underline{1}$)-Zn (Fig. 3.1b), and polar (0001)-O (Fig. 3c) terminated surfaces. On both clean ZnO surfaces we see a clear photoemission peak center around 10.8 eV binding energy (BE) due to the Zn 3*d* emission. The remaining intensity between 4 and 8 eV BE is attributed to the O 2*p* and the Zn 4*s* electrons, respectively. The (10$\underline{1}$0) surface has an additional peak at approximately 6 eV, which has been attributed to a hybridization of the Zn 4*s*-O 2*p* orbitals [27]. Upon deposition of 100 L of phenol at 220 °C, a shoulder appears on the upper edge of the O *2p* band at binding energy of approximately 2.5 eV on the (10$\underline{1}$0) surface, 3.0 eV on the (000$\underline{1}$)-Zn surface, and 2.3 eV on the (0001)-O surface. We assign this shoulder structure at the edge of the valence band maximum (3.7 BE) to be the phenol HOMO band, which primarily lies in the band gap of ZnO. This assignment is consistent with other aromatics on ZnO [28, 29]. In addition, another peak emerges at approximately 14 eV that has been assigned to the phenol sigma orbitals [30]. The spectra for room temperature doses (not shown) were also obtained and the same spectral features appeared for all surfaces at the same binding energies as their higher temperature counterparts.

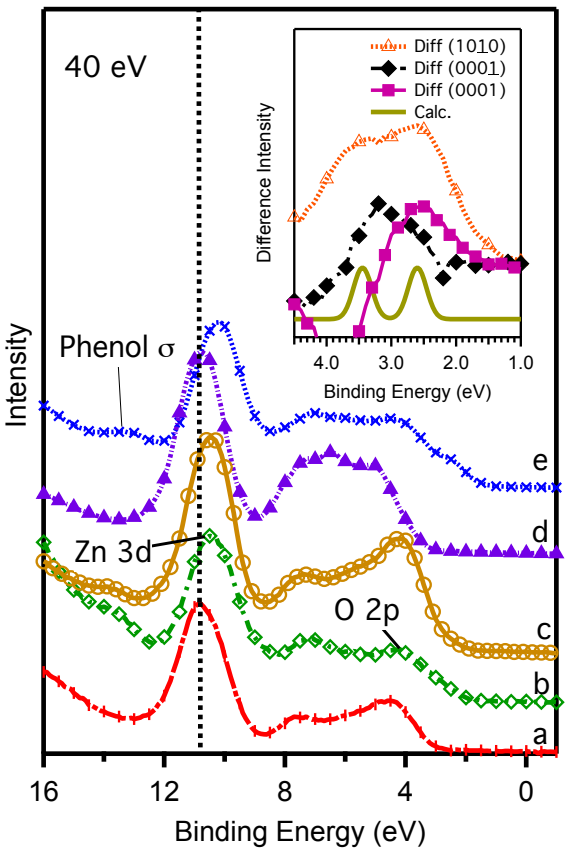

Figure 3.1 Room temperature photoelectron spectra of clean and 100 L of phenol dosed ZnO surfaces at 220 °C: (a) clean (000$\bar{1}$)-Zn; (b) phenol dosed on (000$\bar{1}$)-Zn; (c) phenol dosed on (0001)-O; (d) clean (10$\bar{1}$0) (e) phenol dosed on (10$\bar{1}$0). The dashed line at 10.8 eV indicates the center of the Zn *3d* peak on the clean surfaces and consequent band bending of the phenol dosed surfaces. The inset shows the difference spectra in the region between 1 and 4.5 eV (see text for details) as well as calculated spectrum of a fully relaxed phenol molecule (HOMO and HOMO-1) for comparison.

The inset of figure 3.1 shows difference spectra between both clean and adsorbed surfaces. The difference spectra were obtained after a correction for band bending was performed (see discussion below) and after normalization to the hybrid peak for the (10$\bar{1}$0) surface, the Zn 3*d* peak for the (000$\bar{1}$)-Zn surface, and O *2p* for (0001)-O surface. A comparison of the difference spectrum between the surfaces reveals a 0.5 eV shift to higher binding energy in the Zn

terminated spectrum. The line shape of the phenol HOMO on the Zn terminated surface is also quite different. For the non-polar surface, two peaks are present that appear to be in good agreement with the calculated spectrum that are assigned to the HOMO at 2.5 eV and HOMO-1 at 3.5 eV (see bottom spectrum of the inset). The O-terminated spectrum shows only a peak at 2.5 eV that matches the phenol HOMO peak. However, the Zn-terminated spectrum shows a clear difference with the calculation; specifically, it appears that either one peak has disappeared or that the two peaks are merged together. Another significant difference between the clean and dosed photoelectron spectra is the 0.6 eV, 0.4 eV, and 0.2 eV Zn *3d* band bending for the (10$\underline{1}$0), (000$\underline{1}$)-Zn, and (0001)-O surfaces respectively. This near surface, upward shift toward the Fermi edge (decreasing BE) is consistent with a charge transfer from the surface to the phenol [31, 32].

Although UPS yields information of the near-surface valence structure, EELS provides a surface sensitive method to examine low energy electronic excitations. In combination with UPS, EELS measurements allow us to infer additional key details of the electronic structure of the phenol/ZnO system, specifically the excitations of ZnO and phenol. Figure 3.2 shows EELS spectra of clean and dosed (10$\underline{1}$0) and (000$\underline{1}$)-Zn at the same conditions as figure 3.1. The spectral range of 0.2 - 9 eV loss energy yields direct information on the the ZnO low energy band gap, interband transition at 3.6 eV (as shown in Fig. 3.2a and indicated by the dash-dot vertical line) and the low energy corresponding HOMO-LUMO transitions of phenol [33, 34]. Included is the spectrum from a non-polar

surface with physisorbed phenol at -177 °C (b). At this low temperature multiple layers of phenol are condensed, effectively forming “phenol ice”. Figure 3.2b shows condensed phenol transitions at 3.7, 4.5, 5.7, and 6.5 eV, which are due to π-π* transitions and consistent with previous gas phase measurements of phenol [34]. These excitations specifically are between the HOMO/HOMO-1 and LUMO/LUMO+1/LUMO+2 orbitals of phenol. The intense peak at 6.5 eV (indicated by a dotted vertical line in Fig. 3.2) is similar to that of benzene, but is perturbed by the lone pair of electrons located on the oxygen causing a shift to lower energy [34].

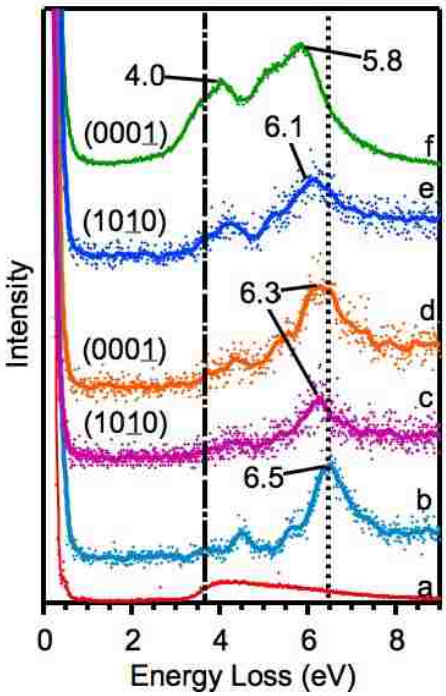

Figure 3.2 EELS spectra of 100 L phenol adsorbed to the (10$\bar{1}$0) and the (000$\bar{1}$)-Zn surfaces at various temperatures. The spectra are as follows: (a) clean (000$\bar{1}$)-Zn: (b) adsorption at -177 °C on (10$\bar{1}$0); (c) adsorption on (10$\bar{1}$0) at room temperature; (d) adsorption on (000$\bar{1}$)-Zn at room temperature; (e) adsorption on (10$\bar{1}$0) at 220 °C; and (f) adsorption on (000$\bar{1}$)-Zn at 220 °C. The dotted vertical line is aligned to the 6.5 eV loss peak of the thick physisorbed phenol layer at -177 °C . The dot-dash vertical line on the left is aligned with the midpoint of the ZnO band gap at approximately 3.6 eV (a). All spectra are normalized to the elastic peak.

Comparing spectra of 100 L adsorbed phenol on the (10$\underline{1}$0) surface at room temperature and 220 °C (c and e), only small differences are observed. The room temperature spectrum (c) is shifted to lower loss energy from the "phenol ice" (b) by 0.2 eV while the 220 °C (e) spectrum is shifted even further to lower energy by 0.4 eV. Other than these shifts in loss energy, overall the spectra for the (10$\underline{1}$0) surface looks like slightly perturbed, but phenol. This corroborates well with the UPS data shown in figure 3.1. There appears to be some temperature dependence on the adsorption of phenol on the non-polar surface. However, this only shifts the spectra to lower energy.

The (000$\underline{1}$)-Zn surface, however, is significantly different from the (10$\underline{1}$0) surface. Figure 3.2d, room temperature adsorption (100 L phenol) very closely resembles the non-polar surface (Fig. 3.2c) under the same conditions. However, when the adsorption occurs at elevated temperature (220 °C) the spectrum (Fig. 3.2f) shifts significantly to lower loss energy by 0.7 eV compared to the Figure 3.2b. More importantly, EELS shows the intensity feature at 2.3 eV which is presumably due to additional transitions from the HOMO of phenol to the conduction band minimum (CB_{min}) of ZnO similar to the nitrocatechol system studied by Arnaud *et. al.*[29] Also, two very prominent peaks are observed at excitation energies of approximately 4.0 and 5.8 eV. These new peaks at 4.0 and 5.8 eV were also observed with nitrocatechol adsorbed to ZnO and were assigned to be the HOMO to LUMO and HOMO to LUMO+1 transitions respectively. Overall, EELS reveals that for the Zn-terminated surface, substantial changes occur between the phenol chemisorbed states at room

temperature and 220 °C, while the non-polar surface shows slight changes between temperatures.

In addition to the electronic information yielded by UPS and EELS, information regarding the surface atomic structure is inferred from LEED. Figure 3.3 shows LEED patterns for the (10$\bar{1}$0) and the (000$\bar{1}$)-Zn surfaces before and after adsorption of 25 L of phenol at room temperature. The non-polar (10$\bar{1}$0) surface is characterized by rows of zinc and oxygen dimers at top of the structural model in Fig. 3.3e. As shown, equal numbers of zinc and oxygen atoms are present in the surface plane making it non-polar. This is in contrast to the polar (0001) surfaces, indicated by sides of the structural model in Fig. 3.3e, which can be terminated with either all zinc (left) or oxygen atoms (right). A typical unreconstructed LEED pattern of ZnO(10$\bar{1}$0) yields a (1x1) rectangular pattern (figure 3.3a). The polar (000$\bar{1}$)-Zn surface (figure 3.3c) also yields a (1x1) pattern with six-fold symmetry, as previously reported in the literature [22, 35]. When the (10$\bar{1}$0) surface is exposed to 25 L of phenol at room temperature, as shown figure 3.3b, a c(2x2) superstructure is observed with streaking along the (0001) direction. This indicates that the phenol is ordered in the (1$\bar{2}$10) direction but lacks long-range coherence, or order, along the (0001) direction. As seen in the structural ZnO model in figure 3.3e, this (0001) direction is perpendicular to the Zn-O dimer rows. When the sample temperature is elevated to 220 °C, the same streaking pattern appears (not shown). Upon additional exposure to phenol (beyond 25 L) the LEED pattern does not change indicating the surface is fully saturated at approximately 0.5 ML.

Unlike the non-polar surface that shows a streaking pattern upon exposure to 25 L phenol, LEED indicates that on the polar (0001)-Zn surface only exhibits an overall increase in diffuse background, as shown in figure 3.3d. This suggests a clear distinction between bonding on the two crystallographic surfaces. When the sample temperature is raised to 220 °C, the same diffuse background appears. For both surfaces there is a lack of temperature dependence with regard to LEED measurements.

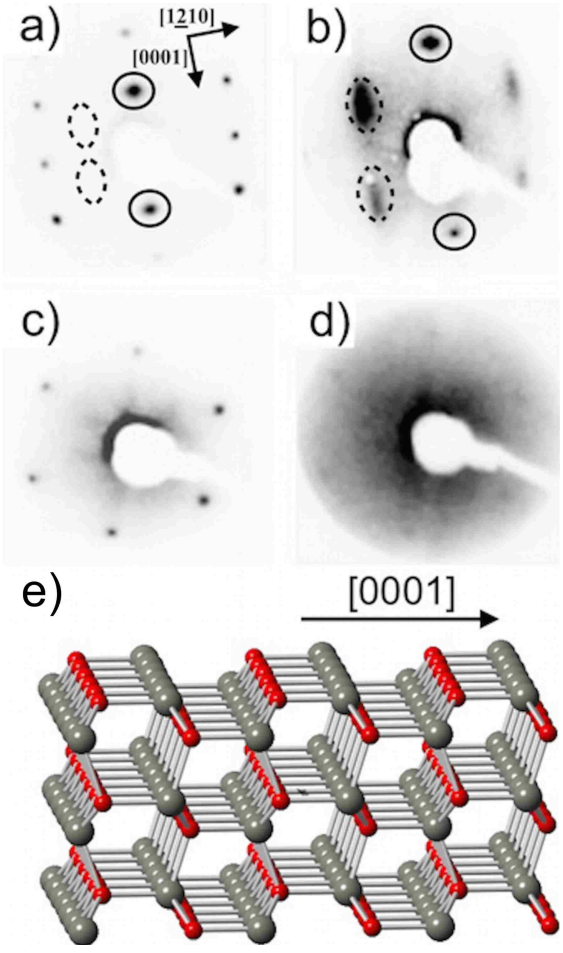

Figure 3.3 LEED patterns of : (a) clean (10$\bar{1}$0), 69 eV; (b) exposed (10$\bar{1}$0) to 25 L phenol at room temperature, 25 eV; (c) clean (000$\bar{1}$)-Zn at 69 eV; (d) exposed (000$\bar{1}$)-Zn to 25 L phenol at room temperature, 69 eV; (e) structural model of ZnO with arrow indicating the (0001) direction The circles in a and b indicate equivalent diffraction spot positions.

3.4 Discussion

A significant observation in figure 3.1 is the 0.6 eV, 0.4 eV, and 0.2 eV band bending on the (10$\bar{1}$0), (000$\bar{1}$)-Zn, and (0001)-O surfaces respectively upon adsorption of phenol. This type of behavior is not an uncommon phenomenon with ZnO, especially when molecules containing oxygen such as carbon monoxide, ethylene oxide, and methanol are adsorbed [32]. This type of band bending occurs when a molecule adsorbs to a weakly screened (non-metallic) surface. The molecular orbitals can either 1) accept charge from the surface, forming an electric field that pulls the bands “upward” (toward the Fermi level) causing a shift to lower binding energy in photoelectron spectra, or 2) donate charge to the surface, forming an electric field that pulls the bands “downward” (away from the Fermi level), shifting the photoelectron spectra to higher binding energy. Based on this idea, our PES results suggest direct evidence of a charge transfer from the ZnO to the phenol [31]. This observation has significant impact on the proposed mechanism of EPFR formation described earlier and that has been previously observed in other metal oxide systems [23]. This previously proposed mechanism indicates that charge is transferred from the adsorbate to metal oxide causing a partial reduction of the metal cation, however, the PES data of all the phenol/ZnO systems indicate the reverse occurs. This could explain why EPFRs form on ZnO while no +1 oxidation state of Zn exists.

The UPS data adds additional insight into phenol bonding, namely the details of the HOMO structure near 2.5 eV. The inset in figure 3.1 shows the difference spectra of both surfaces compared to a WIEN2k calculation of a single

phenol molecule. The (10$\underline{1}$0) surface closely matches the calculation suggesting that the phenyl ring of chemisorbed phenol remains intact on the (10$\underline{1}$0) surface. However, details of the HOMO band(s) on the Zn and O-terminated surfaces are clearly different. It is not clear if a state is being depopulated or if degeneracy is being added to the phenol. Although EELS shows a temperature dependent structure for both non-polar and Zn-terminated surfaces, there is a lack of temperature dependence on both surfaces with respect to the occupied states.

A comparison of the temperature dependent EELS spectra between the two surfaces shows significantly differences. Comparing spectra in Fig. 3.2b with 3.2c, 3.2d, and 3.2e, there is only a slight shift to lower loss energy by 0.2 and 0.4 eV. The dominant feature remains the π-π* transitions at 6.5, 6.3, and 6.1 eV [34]. Spectra seen in Fig. 3.2c, 3.2d, and 3.2e seem to reflect the presence of intact chemisorbed phenol on both surfaces since no spectral features change except for slight shifts in loss energy. Since the UPS shows no HOMO shifts with regard to temperature for each surface, yet the EELS does show shifts to lower loss energies as a function of temperature, this implies that the LUMOs decrease in energy as a function of temperature for both surfaces. Both UPS and EELS data support the observation that the phenyl ring of chemisorbed phenol is indeed intact on the (10$\underline{1}$0) surface.

The high temperature adsorption of phenol on the polar surface (Figure 3.2f) is significantly different than any other spectrum in figure 3.2. Not only does this spectrum have the largest π-π* transition shift of 0.7 eV compared to the “phenol ice”, but also shows a low energy onset excitation at 2.3 eV. No other

spectrum has this as an obvious feature and suggests the presence of a HOMO to metal oxide CB_{min} transition. This means that the phenol HOMO is inserted into the ZnO band gap. While it may be present in the (10$\underline{1}$0) spectra, it is very low in intensity by comparison. The shift to lower energy also implies that the HOMO-LUMO gap has narrowed far more than on the other surface at the elevated temperature adsorption. This significant collapse could suggest that the polar Zn-terminated surface is more conducive for EPFR formation, which corroborates with the UPS data in figure 3.1.

Very few LEED patterns of aromatic organics on ZnO have been recorded [22]. Benzene on ZnO(10$\underline{1}$0) was investigated using LEED by Poss *et al.*[36] The authors found that benzene formed a well ordered c(2x2) superstructure with very sharp diffraction spots. Upon further adsorption, the LEED pattern changed to a c(4x3) structure indicating multilayer growth of benzene which is in contrast to phenol on the same (10$\underline{1}$0) surface wherein no additional superstructures were observed at higher coverages. Moreover, the streaked c(2x2) superstructure remains upon dosing at higher temperatures (220 °C). As a comparison, benzene is believed to lay flat on the surface of ZnO(10$\underline{1}$0) [22, 36], however, it is suspected that phenol binds to the surface through the oxygen atom leaving the phenyl ring to orient itself in a random fashion leading to no long range coherence.

LEED indicates that phenol prefers to bond in a semi-ordered c(2x2) fashion on the (10$\underline{1}$0) surface rather than on the (000$\underline{1}$)- Zn. Since increasing the dosage of phenol beyond 25 L did not change the LEED pattern, this means that

the (10$\underline{1}$0) surface becomes fully saturated near 0.5 ML. This is of great importance for simulations since the bonding geometry can be quite different for both surfaces, which could have impacts on the electronic structure of the adsorbed phenol.

3.5 Conclusion

We have studied the electronic structure and adsorption ordering of the phenol/ZnO model system as a function of both crystallographic face dependence and temperature. We find that upon saturation doses of phenol at room temperature and 220 °C the resulting photoelectron spectra shift to lower binding energy due to band bending, suggesting a charge transfer away from the ZnO toward the chemisorbed phenol. This is contradictory to a previously proposed EPFR formation mechanism based on phenol chemisorbed to rutile TiO_2(110) [23]. Our combined UPS with EELS experimental evidence shows evidence of intact phenyl ring of chemisorbed phenol on the ZnO(10$\underline{1}$0) surface even at elevated temperatures. However, phenol chemisorbed to polar Zn-terminated surface shows significant differences that could suggest EPFR formation is more favorable on that surface. UPS data also showed no temperature differences indicating similar occupied states structure for phenol at both RT and 220 °C. On the other hand, EELS consistently showed excitation shifts to lower loss energy. This means that the HOMO-LUMO gap decreases or collapses and hence only the LUMO states decrease in energy. LEED measurements also showed significant long-range structural differences between adsorption on the two surfaces. Whereas, phenol forms a semi-ordered c(2x2)

superstructure on the (10$\underline{1}$0) surface, it is disordered on the polar Zn-terminated surface. The LEED experiments also showed that phenol is fully saturated near 0.5 ML of phenol on the non-polar surface. This study should serve as guideposts for future computational studies that wish to attempt to model radical formation on ZnO or other metal oxide systems.

3.6 References

(1) Sun, Q.; Altarawneh, M.; Dlugogorski, B. Z.; Kennedy, E. M.; Mackie, J. C. Catalytic Effect of CuO and Other Transition Metal Oxides in Formation of Dioxins: Theoretical Investigation of Reaction Between 2,4,5-Trichlorophenol and CuO. *Environ. Sci. Technol.* **2007**, *41*, 5708–5715.

(2) Evans, C. S.; Dellinger, B. Surface-Mediated Formation of PBDD/Fs From the High-Temperature Oxidation of 2-Bromophenol on a CuO/Silica Surface. *Chemosphere* **2006**, *63*, 1291–1299.

(3) Milligan, M. S.; Altwicker, E. R. Chlorophenol Reactions on Fly Ash. 2. Equilibrium Surface Coverage and Global Kinetics. *Environ. Sci. Technol.* **1996**, *30*, 230–236.

(4) Bandara, J.; Mielczarski, J. A.; Kiwi, J. I. Adsorption Mechanism of Chlorophenols on Iron Oxides, Titanium Oxide and Aluminum Oxide as Detected by Infrared Spectroscopy. *Appl. Catal. B-Environ.* **2001**, *34*, 307–320.

(5) Lomnicki, S.; Truong, H.; Vejerano, E.; Dellinger, B. Copper Oxide-Based Model of Persistent Free Radical Formation on Combustion-Derived Particulate Matter. *Environ. Sci. Technol.* **2008**, *42*, 4982–4988.

(6) Vejerano, E.; Lomnicki, S.; Dellinger, B. Formation and Stabilization of Combustion-Generated Environmentally Persistent Free Radicals on an Fe(III) 2O 3/Silica Surface. *Environ. Sci. Technol.* **2011**, *45*, 589–594.

(7) Vejerano, E.; Lomnicki, S. M.; Dellinger, B. Formation and Stabilization of Combustion-Generated, Environmentally Persistent Radicals on Ni(II)O Supported on a Silica Surface. *Environ. Sci. Technol.* **2012**, *46*, 9406–9411.

(8) Vejerano, E.; Lomnicki, S.; Dellinger, B. Lifetime of Combustion-Generated Environmentally Persistent Free Radicals on Zn(Ii)O and Other Transition Metal Oxides. *J. Environ. Monit.* **2012**, *14*, 2803.

(9) Kiruri, L. W.; Khachatryan, L.; Dellinger, B.; Lomnicki, S. Effect of Copper Oxide Concentration on the Formation and Persistency of Environmentally Persistent Free Radicals (EPFRs) in Particulates. *Environ. Sci. Technol.* **2014**, 2212–2217.

(10) McFerrin, C. A.; Hall, R. W.; Dellinger, B. Ab Initio Study of the Formation and Degradation Reactions of Semiquinone and Phenoxyl Radicals. *J. of Mol. Struct.: Theochem.* **2008**, *848*, 16–23.

(11) Wichmann, H. E.; Peters, A. Epidemiological Evidence of the Effects of Ultrafine Particle Exposure. *Philos. Trans. R. Soc. London, A.* **2000**, *358*, 2751–2769.

(12) Laden, F.; Neas, L. M.; Dockery, D. W.; Schwartz, J. E. Association of Fine Particulate Matter From Different Sources with Daily Mortality in Six U.S. Cities. *Environ Health Persp* **2000**, *108*, 941–947.

(13) Dellinger, B.; Pryor, W. A.; Cueto, R.; Squadrito, G. L.; Hegde, V.; Deutsch, W. A. Role of Free Radicals in the Toxicity of Airborne Fine Particulate Matter. *Chem. Res. Toxicol.* **2001**, *14*, 1371–1377.

(14) Pope, C. A.;Burnett, R. T.; Thun, M. J.; Calle E. E.; Krewski, D.; Ito, K.; Thurston G. D. Lung Cancer, Cardiopulmonary Mortality, and Long-Term Exposure to Fine Particulate Air Pollution. *J. Am. Med. Assoc.* **2002**, 287(9), 1132-1141.

(15) Cruz, dela, A. L. N.; Gehling, W.; Lomnicki, S.; Cook, R.; Dellinger, B. Detection of Environmentally Persistent Free Radicals at a Superfund Wood Treating Site. *Environ. Sci. Technol.* **2011**, *45*, 6356–6365.

(16) Balakrishna, S.; Lomnicki, S.; McAvey, K. M.; Cole, R. B.; Dellinger, B.; Cormier, S. A. Environmentally Persistent Free Radicals Amplify Ultrafine Particle Mediated Cellular Oxidative Stress and Cytotoxicity. *Part. Fibre Toxicol.* **2009**, *6:11*.

(17) Balakrishna, S.; Saravia, J.; Thevenot, P.; Ahlert, T.; Lominiki, S.; Dellinger, B.; Cormier, S. A. Environmentally Persistent Free Radicals Induce Airway Hyperresponsiveness in Neonatal Rat Lungs. *Part. Fibre Toxicol.* **2011**, *8:11*.

(18) Fahmy, B.; Ding, L.; You, D.; Lomnicki, S.; Dellinger, B.; Cormier, S. A. In Vitro and in Vivo Assessment of Pulmonary Risk Associated with Exposure to Combustion Generated Fine Particles. *Environ.Toxicol. Pharmacol.* **2010**, *29*, 173–182.

(19) Mahne, S.; Chuang, G. C.; Pankey, E.; Kiruri, L.; Kadowitz, P. J.; Dellinger, B.; Varner, K. J. Environmentally Persistent Free Radicals Decrease Cardiac Function and Increase Pulmonary Artery Pressure. *Am. J. Physiol. Heart Circ. Physiol.* **2012**, *303*, H1135–H1142.

(20) Lord, K.; Moll, D.; Lindsey, J. K.; Mahne, S.; Raman, G.; Dugas, T.; Cormier, S. A.; Troxlair, D.; Lominiki, S.; Dellinger, B.; et al. Environmentally Persistant Free Radicals Decrease Cardiac Function Before and After Ischemia/Reperfusion Injury in Vivo. *J. Recept. Signal Transduct. Res.* **2011**, *31*, 157–167.

(21) Dulub, O.; Diebold, U.; Kresse, G. Novel Stabilization Mechanism on Polar Surfaces: ZnO(0001)-Zn. *Phys. Rev. Lett.* **2003**, *90*, 016102.

(22) Woll, C. The Chemistry and Physics of Zinc Oxide Surfaces. *Progress in Surface Science* **2007**, *82*, 55–120.

(23) Patterson, M. C.; Thibodeaux, C. A.; Kizilkaya, O.; Kurtz, R. L.; Poliakoff, E. D.; Sprunger, P. T. Electronic Signatures of a Model Pollutant–Particle System: Chemisorbed Phenol on TiO_2(110). *Langmuir* **2015**, *31*, 3869–3875.

(24) Patterson, M. C.; Keilbart, N. D.; Kiruri, L. W.; Thibodeaux, C. A.; Lomnicki, S.; Kurtz, R. L.; Poliakoff, E. D.; Dellinger, B.; Sprunger, P. T. EPFR Formation From Phenol Adsorption on $A_{l2}O_3$ and TiO_2: EPR and EELS Studies. *J. Chem. Phys.* **2013**, *422*, 277–282.

(25) Kizilkaya, O.; Jiles, R. W.; Patterson, M. C.; Thibodeaux, C. A.; Poliakoff, E. D.; Sprunger, P. T.; Kurtz, R. L.; Morikawa, E. High-Throughput Toroidal Grating Beamline for Photoelectron Spectroscopy at CAMD. *J. Phys.: Conf. Ser.* **2014**, *493*, 012024.

(26) P. Blaha, K. Schwarz, G. K. H. Madsen, D. Kvasnicka and J. Luitz, *WIEN2k*, An Augmented Plane Wave + Local Orbitals Program for Calculating Crystal Properties (Karlheinz Schwarz, Techn. Universität Wien, Austria), 2001. ISBN 3-9501031-1-2.

(27) Gopel, W.; Pollman, J.; Ivanov, I.; Reihl, B. Angle-Resolved Photoemission From Polar and Non-Polar Zinc Oxide Surfaces. *Phys. Rev. B* **2011**, *26*, 3144–3150.

(28) Rangan, S.; Theisen, J.-P.; Bersch, E.; Bartynski, R. A. Energy Level Alignment of Catechol Molecular Orbitals on ZnO(11$\underline{2}$0) and TiO_2(110) Surfaces. *Appl. Surf. Sci.* **2010**, *256*, 4829–4833.

(29) Arnaud, G. F.; De Renzi, V.; del Pennino, U.; Biagi, R.; Corradini, V.; Calzolari, A.; Ruini, A.; Catellani, A. Nitrocatechol/ZnO Interface: the Role of Dipole in a Dye/Metal-Oxide Model System. *J. Phys. Chem. C* **2014**, *118*, 3910–3917.

(30) Debies, T. P.; Rabalais, J. W. Photoelectron Spectra of Substituted Benzenes II. Seven Valence Electron Substituents. *J. Electron Spectrosc.* **1972**, *1*, 355–370.

(31) Zhang, Z.; Yates, J. T., Jr. Band Bending in Semiconductors: Chemical and Physical Consequences at Surfaces and Interfaces. *Chem. Rev.* **2012**, *112*, 5520–5551.

(32) Rubloff, G. W.; Luth, H.; Grobman, W. D. Orbital Energy Shifts Associated with Chemical Bonding of Organic Molecules on ZnO Nonpolar Surfaces. *Chem. Phys. Lett.* **1976**, *39*, 493–496.

(33) Jones, D. B.; da Silva, G. B.; Neves, R. F. C.; Duque, H. V.; Chiari, L.; de Oliveiria, E. M.; Lopes, M. C. A.; da Costa, R. F.; do N Varella, M. T.; Bettega, M. H. F.; et al. An Experimental and Theoretical Investigation Into the Excited Electronic States of Phenol. *J. Chem. Phys.* **2014**, *141*, 074314–074318.

(34) Ari, T.; Guven, H.; Ecevit, N. Electron Energy-Loss Spectroscopy of Monosubstituted Benzenes. *J. Electron Spectrosc.* **1995**, *73*, 13–23.

(35) Dulub, O.; Boatner, L. A.; Diebold, U. STM Study of the Geometric and Electronic Structure of. *Surface Science* **2002**, *519*, 201–217.

(36) Poss, D.; Ranke, W.; Jacobi, K.; Adsorption and Epitaxial Growth of Benzene on ZnO(10$\underline{1}$0). *Surf. Sci.* **1981**,105(1), 77-94.

Chapter 4
Adsorption of EPFR Precursors on Silica Supported Cu(II)O Nanoparticles

4.1 Introduction

Environmentally persistent free radicals (EPFRs) develop as a result of the adsorption of substituted benzenes to metal oxide surfaces such as NiO, Fe_2O_3, ZnO, and Cu(II)O [1-4]. EPFRs are known to persist for hours to days under ambient conditions and indefinitely under vacuum. The term EPFR refers to the composite organic/metal oxide particles. Specifically, Cu(II)O is known to be a metal oxide that is very active in forming EPFRs, producing on the order of 10^{18} radicals/g of sample [5]. The 1/e half-lives for radicals formed on Cu(II)O range from 1 to 24 hrs. depending on the concentration of the nanoparticles [1,4,5]. The formation of EPFRs is believed to occur in the cool zone regions of combustion systems. In this combustion region, temperatures range anywhere from 100 – 450 °C [1, 6,7]. EPFRs are also associated with airborne particulate matter (PM). Epidemiological studies have well documented a correlation between increased levels of PM and mortality/morbidity [8-12]. This association poses serious health risks to humans. EPFRs associated PM has been shown to specifically affect the heart, lungs, and cause DNA damage [13-15]. Not only are EPFRs themselves potentially toxic, but they are suspected to be stable intermediates that eventually form dioxins and furans [16-18].

This study aims to understand the electronic structure of the EPFRs, as well as the nature of the nanoparticle surface and reactivity as a function of size and temperature. This study also wishes to examine the 3D structure of the nanoparticles to discern if they have significant height (interior Cu atoms) or if they are essentially 2D "flat" structures. This is to see if the EPFR precursors have access to the majority of Cu of the nanoparticles. Specifically, we used X-ray absorption near edge structure (XANES) to examine the electronic structure of the EPFR by probing the metal sites on the nanoparticles, namely the oxidation state of the Cu. This gives more details about the electronics of the EPFRs and to see which direction charge transfer flows. To probe the Cu(II)O surface even further, chlorinated EPFR precursors were adsorbed to the surface as a tag to examine the structure and reactivity of the nanoparticles as a function of size and temperature by looking at the ratio of halogen (i. e. Cl) to Cu using x-ray fluorescence (XRF).

Previous x-ray studies of EPFR precursors adsorbed Cu(II)O have taken place using micron size particles [7,17,19]. One of the x-ray studies did focus on synthetic nanoparticles, but was mainly concerned with the geometrical and electronic structure of nanoparticles prepared by dendrimers using extended x-ray absorption fine structure (EXAFS). The EXAFS measurements revealed no long range ordering of the nanoparticles suggesting a flat "pancake" structure [19]. Other EPFR studies involving nanoparticles have mainly been carried out using EPR [1-4]. The use of nanoparticles, especially synthetic nanoparticles, is used to mimic fly ash from combustion systems. Real combustion system fly ash

contains several different materials with the largest percentage being silica [20-24]. The concentration of metals can vary widely from place to place and depends heavily on the conditions of the combustion reaction itself [24-26]. Therefore, surrogates are synthesized to understand an individual metal oxide's role in EPFR formation.

There is little direct evidence of the structure of the EPFR system. Most previous studies have been done using EPR. Only an unverified and probably not generally applicable mechanism has been proposed [1,2,27]. The mechanism consists of physisorption of the molecule, typically aromatic systems with alcohols or Cl bonded to the aromatic ring, to the surface followed by elimination of water or HCl (depending on the precursor used) and chemisorption to the surface. During the chemisorption process, electron transfer occurs, reducing the metal and forming the EPFR. This essentially turns the Cu(II)O into Cu_2(I)O making it a suitable study for XANES.

In this study, we used XANES to probe the oxidation state of Cu when exposed to the EPFR precursor phenol to examine the electronic structure of the EPFR. XRF was used to examine the ratio of Cl to Cu when chlorinated precursors were adsorbed to the nanoparticle surface. By examining this ratio, information regarding the number of radicals per metal atom can be obtained. This gives additional information regarding the reactivity and 3D structure of the nanoparticles. We have obtained results regarding the nanoparticles themselves that have to be taken into account when doing similar studies, namely, the oxidation state of the metal when heated without any EPFR precursor present.

The XRF results presented also may have significant consequences regarding previous health science studies, which used chlorinated aromatics as EPFR precursors [14-16].

This investigation is part of a larger program to study EPFR precursors on transition metal oxides. The results will show that other factors have to be taken into account when studying similar systems. By performing detailed studies of the atomistic and electronic structure of such systems a more detailed picture maybe obtained to understand how each system behaves individually, highlighting their similarities and their differences. The results of these studies can also help in determining future remediation strategies to curb EPFR formation in combustion systems.

4.2 Materials and Methods

XANES experiments were carried out using the double crystal monochromator (DCM) located at the Center for Advanced Microstructures and Devices (CAMD). The monochromator was equipped with Ge(220) crystals to select the appropriate wavelengths. The beamline was also equipped with a silicon drift detector (SSD) to operate in fluorescence mode. The beamline has the capability to access the energies between the Cu L_{III} edge at 932.5 eV and the Mo K edge at 20,000 eV. The energies are dependent upon the crystals used. The schematic of the beamline is shown if figure 4.1.

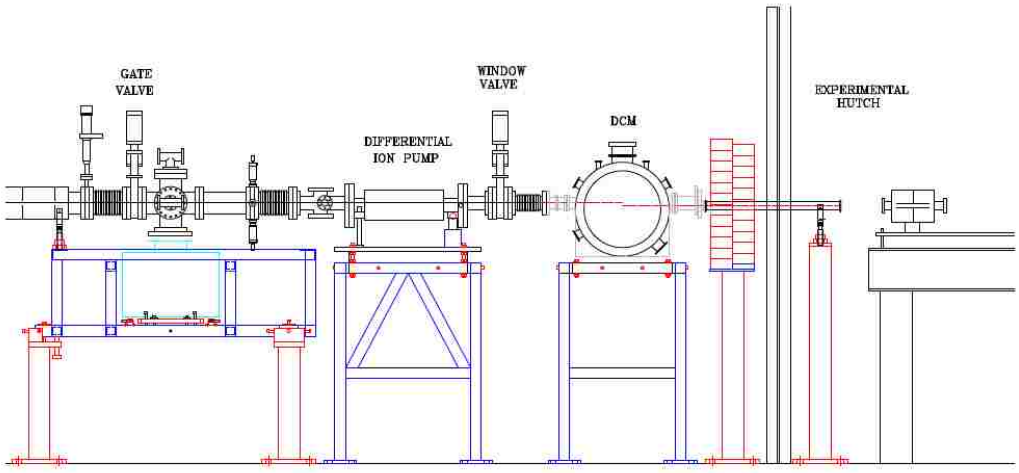

Figure 4.1 Schematic drawing of the DCM beamline [28].

To obtain the best results it was necessary to construct an *in-situ* chamber so that the nanoparticles can be exposed to phenol (99% from Sigma-Aldrich) and immediately measured afterward at the beamline.. The chamber is equipped with a tungsten mesh sample holder that samples were pressed onto. This allows samples to be rapidly heated and cooled to quench the reaction. The temperature was measured with a k-type thermocouple attached to the mesh. Also the chamber is equipped with a turbo molecular pump to achieve a pressure of 10^{-6} Torr. To protect the SSD, a fluorescence window made of Kapton was added to the chamber itself allowing the detector to remain on the outside and allowing 99% transmission of the x-rays of interest to pass and strike the detector. Once the data was obtained, it was processed and analyzed using principle component analysis (PCA) and linear combination fitting with the Demeter software package [29]. A schematic of the chamber is shown in figure 4.2.

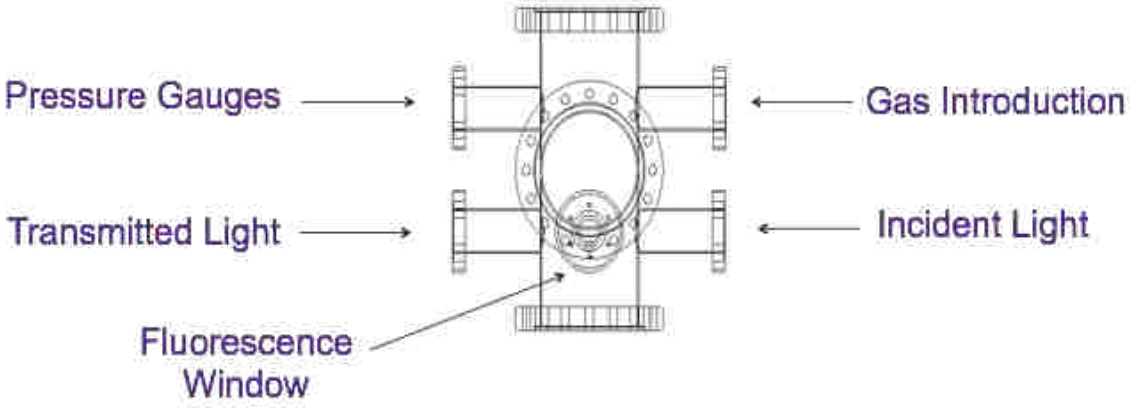

Figure 4.2 A schematic of the *in-situ* chamber for the DCM beamline.

XRF measurements were carried out using the FEI Quanta 3D FEG Dual Beam SEM/FIB microscope with an energy dispersive spectrometer (EDS) attachment, which is equipped with a SSD detector located at the LSU Materials Characterization Center (MCC). Temperature dependent adsorption experiments were measured with a Bruker S2 Picofox XRF spectrometer. Dosing with EPFR precursors was done in Dr. Dellinger's laboratory using a custom-made glass setup and transported under vacuum to the MCC. Experiments using the Picofox were submitted to Bruker for analysis under N_2. The custom made dosing setup in the Dellinger lab allows for temperature controlled dosing and is equipped with a roughing pump achieving pressures on the order of 10^{-2} Torr. A schematic of the dosing setup is shown in figure 4.3. Samples were exposed to vapors of 1,4-Dichlorobenzene (1,4-DCB) (99%), 1,2-dichlorobenzene (1,2-DCB) (99%), and pentachlorophenol (PCP) (97%) purchased from Sigma-Aldrich for 5 min. Pentachlorophenol was further used in other experiments varying the size of the nanoparticles and exposures at different temperatures.

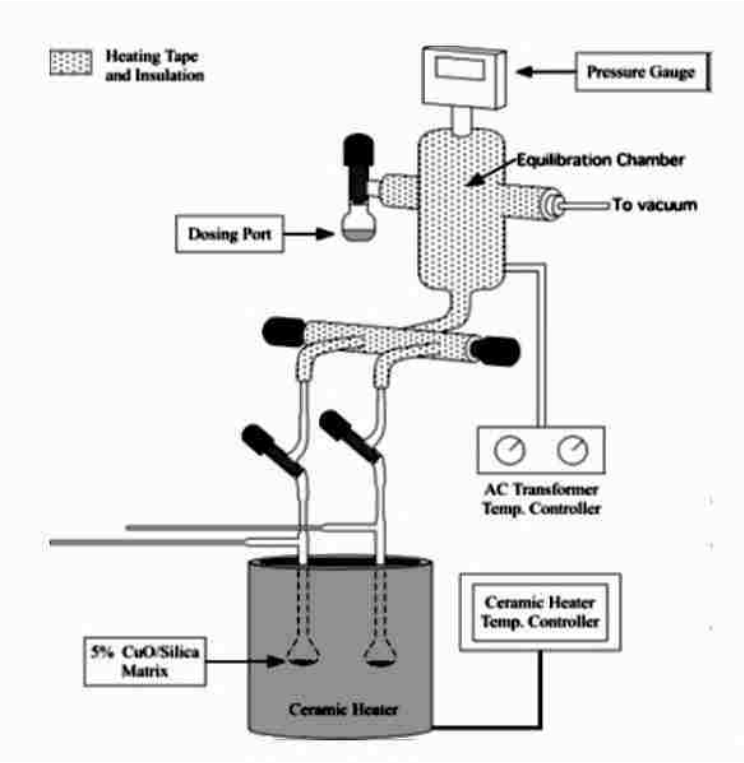

Figure 4.3 A schematic of the custom glass setup used for XRF experiments [19].

4.3 Results

Figure 4.4 shows the size distributions for Cu(II)O nanoparticles on cab-o-sil SiO_2 using the incipient wetness method as described previously. The weight percent measured was 5, 3, and 1%. As expected the 5% yielded the largest particles with an average diameter of 6.43 nm while the 1% were the smallest with an average diameter of 1.67 nm. These sizes are comparable to nanoparticles previously made using dendrimeric preparations [30]. Interestingly, the 5% sample also had the largest overall width while the 1% had the smallest. It is far to say that as the weight percent decreases (smaller particle sizes) the particles become more monodispersed.

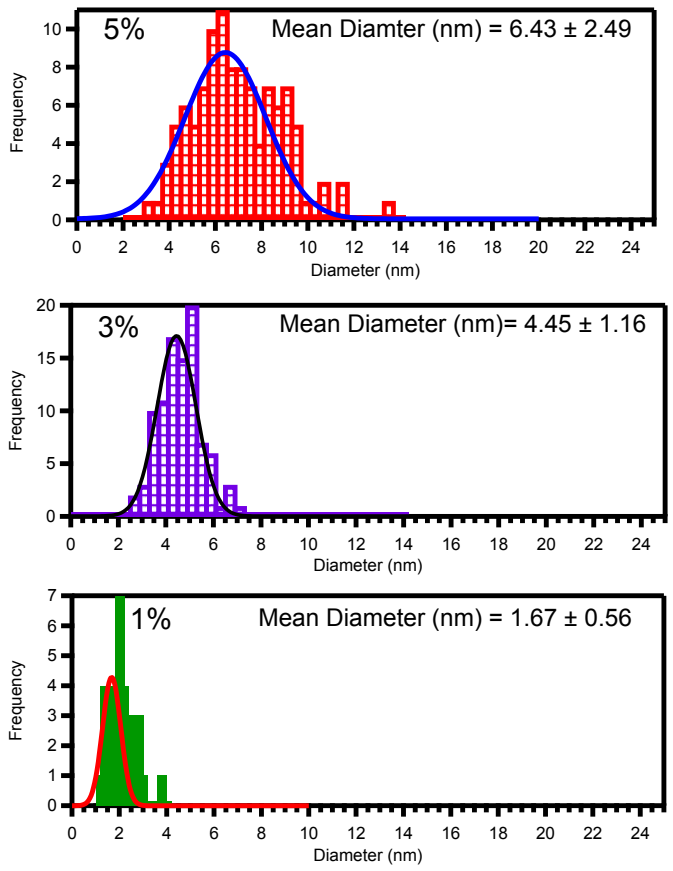

Figure 4.4 Size distributions of Cu(II)O nanoparticles on cab-o-sil.

To ensure that only the phenol will affect the nanoparticles a temperature study was performed. The nanoparticles (3% wt.) were heated without phenol present from 60 °C – 400 °C and held for 5 min and the oxidation state of Cu was measured. Figure 4.5 shows the XANES measurements. The samples start as Cu(II)O as expected. However, when the temperature reaches approximately 260 °C the spectra begin to shift to lower photon energy. When the temperature reaches 300 °C, a peak associated with the 1s ➔ 4p transition appears at 8983 eV which is indicative of Cu(I) formation [31]. The Cu(0) edge peak appears at ~8980 eV. This clearly shows a reduction without any phenol present to Cu(I).

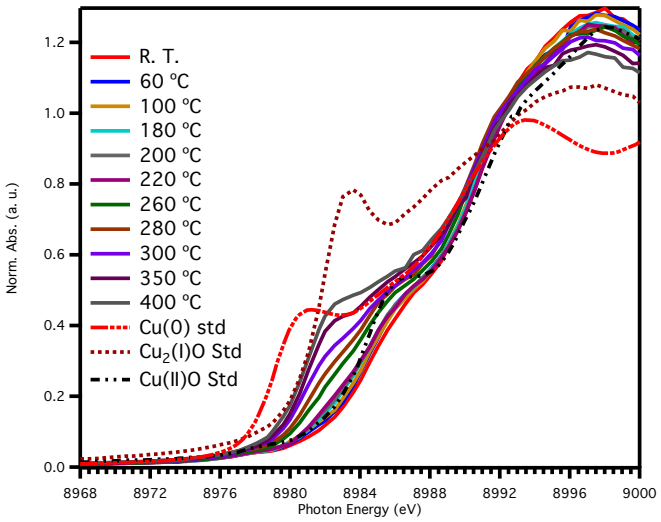

Figure 4.5 XANES spectra of 3% wt. silica supported Cu(II)O at various temperatures.

Using PCA it was determined that no Cu(0) had formed even at 400 °C. The only two Cu compounds present was determined to be Cu(II)O and Cu_2(I)O. Additional linear combination fitting was performed on the spectra at 400 °C. The fit in figure 4.6 shows that at 400 °C 51% of the Cu(II)O is reduced to Cu_2(I)O.

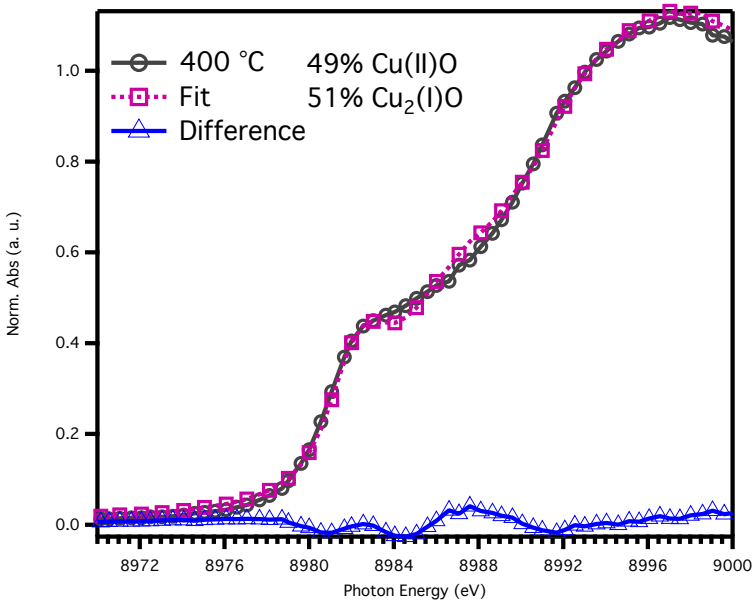

Figure 4.6 Linear combination fit of 3% wt. silica supported Cu(II)O nanoparticles heated at 400 °C for 5 min.

Since Cu(II)O can reduce to $Cu(I)_2O$ just by heating the sample, the adsorption experiments with phenol have to be in a certain temperature range. For our experiments we wished to have a comparable temperature to previous Cu(II)O studies (maximize EPFRs) while minimizing the reduction by heating as much as possible. Therefore, 190 °C and 220 °C was chosen. Also, the 1% wt. sample was chosen to react with the phenol. This was due to their smaller size and more percent Cu of the total Cu present are on the surface available for reduction by the phenol. Shown in figure 4.7 are the spectra for 1% wt. Cu(II)O at 220 °C exposed to phenol for various of amounts of time. This was to see how long it took for most of the Cu to react with the phenol. Included in the spectra are the linear combination fits. Again, PCA excluded Cu metal as being apart of the samples.

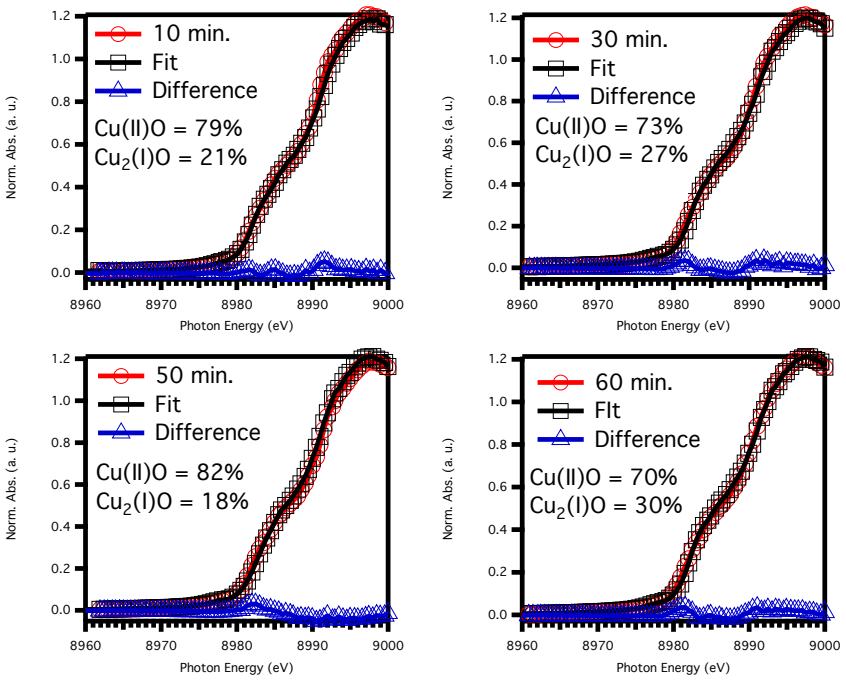

Figure 4.7 XANES spectra of 1% wt. Cu(II)O reacted with phenol at 220 °C for various amounts of time. Included are the linear combination fits and the amounts of Cu(II)O and $Cu_2(I)O$ present in the samples.

Figure 4.7 shows that some of the Cu(II) reduces to Cu(I). The maximum amount of reduction is roughly 30% after 60 min. of exposure. However, it is also noticeable that the amount of reduction varies significantly between different times of exposure. For example, after 30 min. of exposure the amount of Cu(II) reduced is 27% before lowering to 18% after 50 min. After 60 min. of exposure the amount of reduction goes back up to 30%. This is certainly not to be expected. If the nanoparticles are left to react with phenol for longer periods of time then the amount of reduction to Cu(I) should steadily increase. However, this is not what is observed. The same is true for 190 °C (not shown). In other experiments no reduction was observed at all. This raised significant questions about the experimental setup.

To understand the reactivity and 3D structure of the Cu(II)O nanoparticles chlorinated EPFR precursors were adsorbed under various conditions. The first measurements were to adsorb different precursors to see if the Cl to Cu ratios could indicate how many radicals were formed on the surface per metal atom. This essentially would give an indication of how many surface metals would be available for reduction and the 3D structure could be discerned. Figure 4.8 shows XRF measurements of 1,4-DCB, 1,2-DCB, and PCP adsorbed to silica supported 2% wt. Cu(II)O at 230 °C using the custom glass setup in Dr. Dellinger's lab for exposing the nanoparticles to the proper precursor.

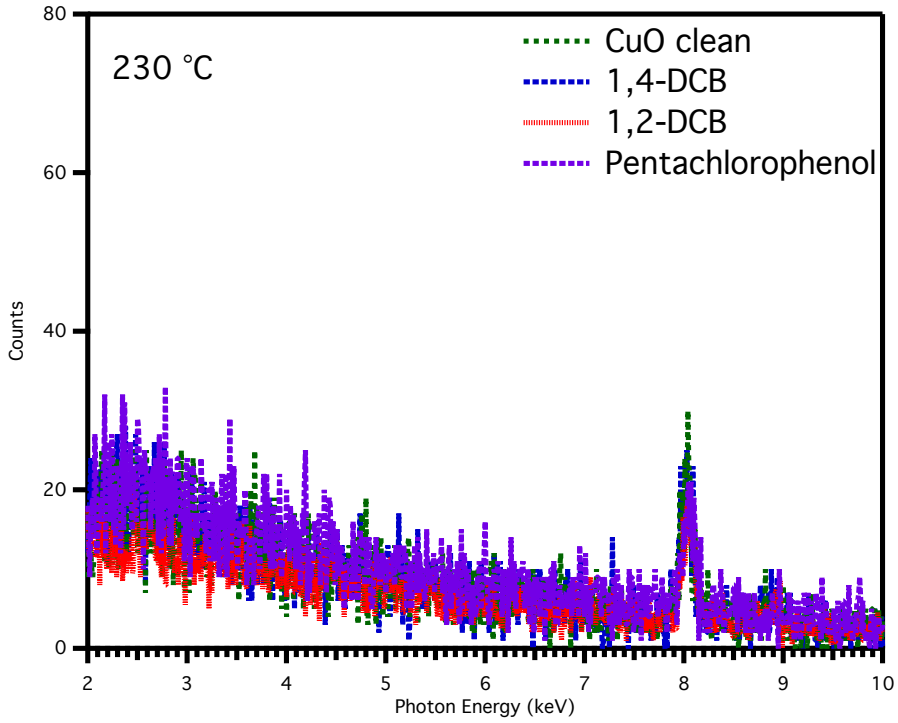

Figure 4.8 XRF spectra of various EPFR precursors adsorbed to 2% wt. Cu(II)O nanoparticles at 230 °C.

The XRF data in figure 4.8 clearly shows a Cu peak at 8 keV. However, surprisingly there is no Cl peak that should appear at 2.62 keV. No chlorine was observed for any of the chlorinated precursors that were adsorbed to the Cu(II)O nanoparticles.

Since PCP does have five Cl bonded to the phenyl ring, it was chosen as the EPFR precursor for two other XRF experiments. Also, the orientation of phenols on metal oxides tends to favor a more perpendicular orientation relative to the surface rather than a flat orientation like benzenes [32, 33]. These experiments involved adsorbing PCP to different sizes of nanoparticles and a temperature dependent experiment. Figure 4.9 shows the XRF spectra of PCP adsorbed to different sizes of Cu(II)O nanoparticles.

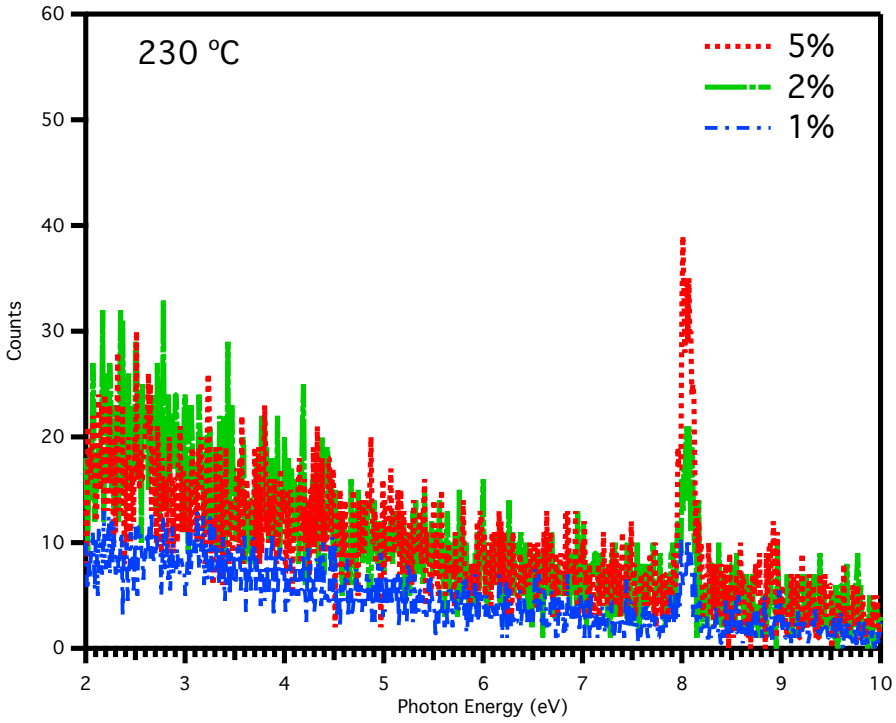

Figure 4.9 XRF spectra of various sizes (% wt.) of Cu(II)O nanoparticles exposed to PCP for 5 min. at 230 °C.

Since nanoparticles get smaller as the percent by weight decreases, this causes a greater percentage of the total Cu to be present on the surface and available for reactions with PCP. The expected result was to eventually see the Cl peak that was absent in figure 4.8. In figure 4.9 a clear Cu peak was again seen at 8 keV. As expected, when the size of the nanoparticles decrease, so does the intensity of the Cu peak. However, no matter the size of the nanoparticle no Cl peak was observed.

The last XRF experiment performed was done by dosing the Cu(II)O nanoparticles at different temperatures. By adjusting the temperature, the point at which the most EPFRs formed can be obtained. Figure 4.10 shows the XRF spectra taken by Bruker of 2% wt. Cu(II)O exposed to PCP at various

temperatures (230 °C, 190 °C, and 150 °C). 2% wt. nanoparticles were chosen because they offered a middle ground between having sufficient size to obtain a good Cu signal and potential for having plenty of surface Cu available for reduction.

Figure 4.10 shows the intense Cu peak at 8 keV in the top graph from 7 keV to 12 keV and no Cl was observed under any temperature condition in the bottom graph. Unexpectedly there seems to be no conditions that we have tried that yield EPFRs with Cl still attached to the phenyl ring. This does not mean that the Cl is not present is some form, but that it was not detected by our experiments. To make sure EPFRs were present, EPR measurements were performed and phenoxy type radical signals were observed ruling out the possibility of no EPFR formation at all

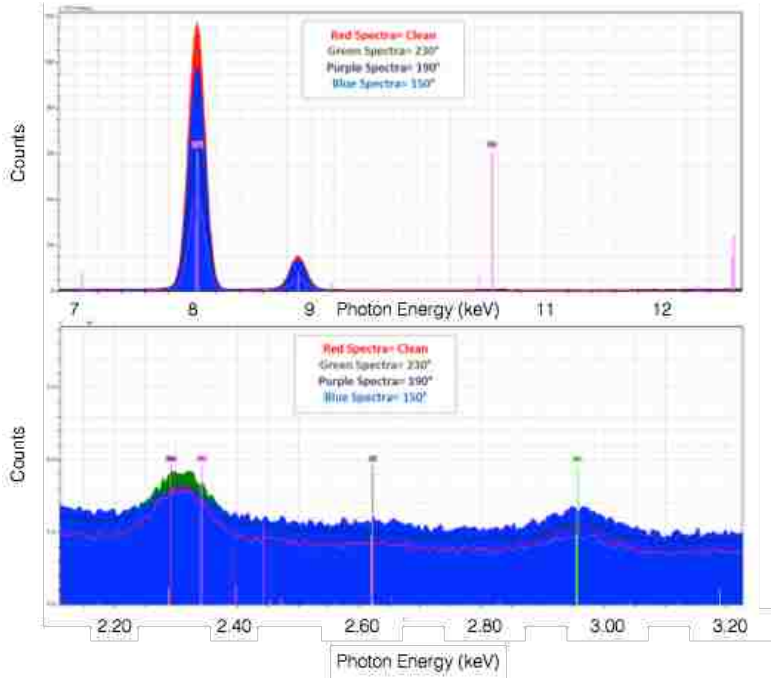

Figure 4.10 XRF spectra of 2% wt. Cu(II)O nanoparticles exposed to PCP at different temperatures.

4.4 Discussion

The XANES data shown in figure 4.5 clearly shows that the Cu(II)O nanoparticles can be reduced to $Cu(I)_2O$ just by heating under high vacuum. This phenomenon has been observed before in other experiments, which we were not aware of at the time of these studies [34-38]. One of the experiments used bulk Cu(II)O powders and were able to see reduction to Cu(I) at 800 K [34]. Other studies with different transition metal oxides show that a possible reason for the reduction is due to adventitious carbon. When heated the carbon reacts with oxygen to form carbon monoxide and reduces the metals. This has been observed in other transition metal oxides such as NiO and CoO [35-37]. Reduction by heating should also be examined for other metal oxides, which may undergo this same phenomenon.

Exposing Cu(II)O nanoparticles to phenol at 220 °C and 190 °C in principle should maximize the amount of EFPRs and minimize the amount of reduction by heating. Figure 4.7 does show reduction by phenol at 220 °C in agreement with the proposed mechanism of EPFR formation. The amount of reduction suggests that there is a large fraction of metal atoms on the interior of the nanoparticles that are unable to be reduced to Cu(I). However, the amount of reduction varies wildly at 220 °C and the same was true for 190 °C. There are two potential reasons for this result. First, since the samples had to be pressed onto the tungsten mesh this could have covered potential reactive sites. The phenol was simply unable to diffuse through the powder and access the interior Cu sites. The other potential reason is that since heating had to be done by

supplying current through a tungsten mesh, which is composed of several fine wires, a heat gradient resulted. This would effectively cause some Cu to reach the proper temperature and react and others go unreacted. Both of the scenarios are possible individually and both could have occurred simultaneously. In the end this means that a redesign of the sample holder is in order for future experiments. The sample holder should in principle heat the samples evenly, heat in air to reoxidize samples, and if possible hold multiple samples for more efficient measurements.

The XRF measurements were surprising. In each case the Cu peak was present but no Cl was visible no matter the size of the nanoparticles or the temperature when dosing with PCP. The carbon chlorine bond is a weak bond and elimination of some chlorine is expected. This is especially true for the adsorbents with only two chlorines. PCP however has five Cl atoms and some were expected to have remained on the phenyl ring. This is not what was observed. The literature has reported that fly ashes and specifically metal oxides can be very effective in dechlorinating aromatics. Specifically, Cu(II)O was identified as having the best results of any metal oxide tested [38-40]. Another possible explanation for the dechlorination of PCP and other precursors is the sources of the measurements themselves. Since the SEM and X-ray fluorometer output high-energy particles this could cause dechlorination of the precursors. This is certainly a concern for our purposes of studying EPFRs on metal oxides. This may also have impacts with previous and future health science studies. Many of the previous studies done in the health sciences with EPFRs have used

either 2-monochlorophenol or 1,2-dichlorobenzene as precursors [13-15]. According to our results the chlorine does not remain with the EPFR. Therefore, this changes the chemistry of the EPFR itself. The results they have observed may more closely match phenol or benzene produced EPFRs rather than chlorinated EPFRs.

Future studies are currently being planned to vary the conditions for both XANES and XRF measurements. The chamber‘s sample holder is being redesigned. XRF measurements are currently being planned to include other metal oxides such as ZnO and Fe_2O_3 that are also known to form EPFRs and are not as efficient for dechlorination. Other preparations of nanoparticles such as nanoparticles prepared with dendrimers are also being used for XRF measurements to see if they differ from the incipient wetness prepared nanoparticles.

4.5 Conclusion

We have studied the electronic structure of phenol and chlorinated EPFR precursors chemisorbed to Cu(II)O nanoparticles using XANES and XRF. The results presented do have some agreement with the proposed mechanism of EPFR formation by showing a reduction of Cu(II) to Cu(I) after adsorption. The small amount of reduction by phenol of Cu(II)O to $Cu(I)_2O$ nanoparticles suggests a large fraction of metal atoms are on the interior of the nanoparticles. This makes them unavailable for reaction with phenol therefore they stay Cu(II). However, the amount of reduction is very inconsistent with reductions ranging from 0% to 30% Cu(I). This could be a consequence of equipment design. Also,

the reduction of Cu(II) to Cu(I) can be achieved just by heating Cu(II)O nanoparticles to 260 °C under vacuum without the EPFR precursor present. This phenomenon, potentially due to adventitious carbon, has to be taken into account when studying similar systems in case this occurs for other transition metal oxides. The XRF results also show that Cu(II)O can potentially dechlorinate EPFR precursors. This was demonstrated by varying the precursors, the nanoparticle sizes, and temperature of exposure. In each set of XRF measurements no Cl was observed. This may have significant impacts on past and future health science studies. By dechlorinating the EPFR precursor the species changes which could altar certain results. Future studies are currently underway to examine more closely this dechlorination phenomenon and determine where the Cl is going.

4.6 References

(1) Lomnicki, S.; Truong, H.; Vejerano, E.; Dellinger, B. Copper Oxide-Based Model of Persistent Free Radical Formation on Combustion-Derived Particulate Matter. *Environ. Sci. Technol.* **2008**, *42*, 4982–4988.

(2) Vejerano, E.; Lomnicki, S.; Dellinger, B. Formation and Stabilization of Combustion-Generated Environmentally Persistent Free Radicals on an $Fe(III)_2O_3$/Silica Surface. *Environ. Sci. Technol.* **2011**, *45*, 589–594.

(3) Vejerano, E.; Lomnicki, S. M.; Dellinger, B. Formation and Stabilization of Combustion-Generated, Environmentally Persistent Radicals on Ni(II)O Supported on a Silica Surface. *Environ. Sci. Technol.* **2012**, *46*, 9406–9411.

(4) Vejerano, E.; Lomnicki, S.; Dellinger, B. Lifetime of Combustion-Generated Environmentally Persistent Free Radicals on Zn(II)O and Other Transition Metal Oxides. *J. Environ. Monit.* **2012**, *14*, 2803–2806.

(5) Kiruri, L. W.; Khachatryan, L.; Dellinger, B.; Lomnicki, S. Effect of Copper Oxide Concentration on the Formation and Persistency of Environmentally Persistent Free Radicals (EPFRs) in Particulates. *Environ. Sci. Technol.* **2014**, *48,* 2212–2217.

(6) Dellinger, B.; Lomnicki, S.; Khachatryan, L.; Maskos, Z.; Hall, R. W.; Adounkpe, J.; McFerrin, C.; Truong, H. Formation and Stabilization of Persistent Free Radicals. *P. Combust. Inst.* **2007**, *31*, 521–528.

(7) Farquar, G. R.; Alderman, S. L.; Poliakoff, E. D.; Dellinger, B. X-Ray Spectroscopic Studies of the High Temperature Reduction of Cu(II)O by 2-Chlorophenol on a Simulated Fly Ash Surface. *Environ. Sci. Technol.* **2003**, *37*, 931–935.

(8) Laden, F.; Neas, L. M.; Dockery, D. W.; Schwartz, J. E. Association of Fine Particulate Matter From Different Sources with Daily Mortality in Six U.S. Cities. *Environ. Health Persp.* **2000**, *108(10),* 941–947.

(9) Dockery, D.W.; Pope, C.A.; Xu, X.; Spengler, J.D.; Ware, J.H.; Fay, M.E.; Ferris, B.G.; Speizer, F.E. An Association Between Air Pollution and Mortality in Six US Cities. *N. Engl. J. Med.* **1993**, *329*, 1753–1759.

(10) Pope III, C.A.; Burnett, R.T.; Thun, M.J.; Calle, E.E.; Krewski, D.; Ito, K.; Thurston, G.D. Lung Cancer, Cardiopulmonary Mortality, and Long-Term Exposure to Fine Particulate Air Pollution. JAMA **2002**, *287(9),* 1132–1141.

(11) Ibald-Mulli, A.; Wichmann, H.E.; Kreyling, W.; Peters, A., Epidemiological Evidence on Health Effects of Ultrafine Particles. J. Aerosol. Med**. 2002**, *15,*189–201.

(12) Cormier, S. A.; Lomnicki, S.; Backes, W.; Dellinger, B. Origin and Health Impacts of Emissions of Toxic by-Products and Fine Particles From Combustion and Thermal Treatment of Hazardous Wastes and Materials. *Environ. Health Perspect.* **2006**, *114*, 810–817.

(13) Dellinger, B.; Pryor, W. A.; Cueto, R.; Squadrito, G. L.; Hegde, V.; Deutsch, W. A. Role of Free Radicals in the Toxicity of Airborne Fine Particulate Matter. *Chem. Res. Toxicol.* **2001**, *14*, 1371–1377.

(14) Balakrishna, S.; Saravia, J.; Thevenot, P.; Ahlert, T.; Lominiki, S.; Dellinger, B.; Cormier, S. A. Environmentally Persistent Free Radicals Induce Airway Hyperresponsiveness in Neonatal Rat Lungs. *Part. and Fibre Toxicol.* **2011**, *8:11*.

(15) Mahne, S.; Chuang, G. C.; Pankey, E.; Kiruri, L.; Kadowitz, P. J.; Dellinger, B.; Varner, K. J. Environmentally Persistent Free Radicals Decrease Cardiac Function and Increase Pulmonary Artery Pressure. *Am. J. Physiol. Heart Circ. Physiol.* **2012**, *303*, H1135–H1142.

(16) Lomnicki, S.; Dellinger, B. A Detailed Mechanism of the Surface-Mediated Formation of PCDD/F From the Oxidation of 2-Chlorophenol on a CuO/Silica Surface. *J. Phys. Chem. A* **2003**, *107*, 4387–4395.

(17) Alderman, S. L.; Farquar, G. R.; Poliakoff, E. D.; Dellinger, B. An Infrared and X-Ray Spectroscopic Study of the Reactions of 2-Chlorophenol, 1,2-Dichlorobenzene, and Chlorobenzene with Model CuO/Silica Fly Ash Surfaces. *Environ. Sci. Technol.* **2005**, *39*, 7396–7401.

(18) Nganai, S.; Lomnicki, S.; Dellinger, B. Ferric Oxide Mediated Formation of PCDD/Fs From 2-Monochlorophenol. *Environ. Sci. Technol.* **2009***, 43(2),* 368–373.

(19) Rodrigo, U. I. Geometrical and Electronic Structure of Metal Oxide Nanoparticles on Silica and Alumina. Ph. D. Dissertation, Louisiana State University, Baton Rouge, LA, 2012.

(20) Rogge, W. F.; Hlldemann, L. M.; Mazurek, M. A.; Cass, G. R. Sources of Fine Organic Aerosol. 2. Noncatalyst and Catalyst-EquippedAutomobiles and Heavy-Duty Diesel Trucks. *Environ. Sci. Technol.* **1993**, *27*, 636–651.

(21) Fine, P. M.; Cass, G. R.; Simoneit, B. R. T. Chemical Characterization of Fine Particle Emissions From Fireplace Combustion of Woods Grown in the Northeastern United States. *Environ. Sci. Technol.* **2001**, *35*, 2665–2675.

(22) Nelson, P. F. Trace Metal Emissions in Fine Particles From Coal Combustion. *Energy Fuels.* **2007**, *21*, 477–484.

(23) Fine, P. M.; Cass, G. R.; Simoneit, B. R. T. Chemical Characterization of Fine Particle Emissions From the Fireplace Combustion of Woods Grown in the Southern United States. *Environ. Sci. Technol.* **2002**, *36*, 1442–1451.

(24) Murillo, J. H.; Ramos, A. C.; García, F. Á.; Jiménez, S. B.; Cárdenas, B.; Mizohata, A. Chemical Composition of $PM_{2.5}$ Particles in Salamanca, Guanajuato Mexico: Source Apportionment with Receptor Models. *Atmos. Res.* **2012**, *107*, 31–41.

(25) Qureshi, S.; Dutkiewicz, V. A.; Khan, A. R.; Swami, K.; Yang, K. X.; Husain, L.; Schwab, J. J.; Demerjian, K. L. Elemental Composition of PM2.5 Aerosols in Queens, New York: Solubility and Temporal Trends. *Atmos. Environ.* **2006**, *40*, 238–251.

(26) Yongjie, Y.; Yuesi, W.; Tianxue, W.; Wei, L.; Ya'nan, Z.; Liang, L. Elemental composition of $PM_{2.5}$ and PM_{10} at Mount Gongga in China during 2006. *Atmos. Res.* **2009**, *93*, 801–810.

(27) Patterson, M. C.; Keilbart, N. D.; Kiruri, L. W.; Thibodeaux, C. A.; Lomnicki, S.; Kurtz, R. L.; Poliakoff, E. D.; Dellinger, B.; Sprunger, P. T. EPFR Formation From Phenol Adsorption on Al_2O_3 and TiO_2: EPR and EELS Studies. *J. Chem. Phys.* **2013**, *422*, 277–282.

(28) Center for Advanced Microstructures and Devices. Double Crystal Monochromator.http://www.camd.lsu.edu/beamline_info/DCM_beamline_2008.pdf (accessed Mar. 24, 2015).

(29) B. Ravel and M. Newville, ATHENA, ARTEMIS, HEPHAESTUS: data analysis for X-ray absorption spectroscopy using IFEFFIT, Journal of Synchrotron Radiation **12**, 537–541 (2005).

(30) Lomnicki, S. M.; Wu, H.; Osborne, S. N.; Pruett, J. M.; McCarley, R. L.; Poliakoff, E.; Dellinger, B. Size-Selective Synthesis of Immobilized Copper Oxide Nanoclusters on Silica. *Mat. Sci. Eng. B* **2010**,175(2), 136–142.

(31) Kau, L.-S.; Spira-Solomon, D.; Penner-Hahn, J. E.; Hodgson, K. O.; Solomon, E. I. X-Ray Absorption Edge Determination of the Oxidation State and Coordination Number of Copper: Application to the Type 3 Site in *Rhus Vernicifera* Laccase and Its Reaction with Oxygen. *J. Am. Chem. Soc.* **1987**, *109*, 6433–6442.

(32) Sosa, G. A.; Evans, T. M.; Parker, S. C.; Campbell, C. T.; Thornton, G. Quantum-Chemical Investigations of Phenol and Larger Aromatic Molecules at the TiO_2 Anatase (101) Surface. *J. Phys. Chem. B* **2008**, *105*, 3783–3785.

(33) Poss, D.; Ranke, W.; Jacobi, K.; Adsorption and Epitaxial Growth of Benzene on ZnO(10$\underline{1}$0). *Surf. Sci.* **1981**,105(1), 77-94.

(34) Poulston, S.; Parlett, P. M.; Stone, P.; Bowker, M.; Surface Oxidation and Reduction of CuO and Cu_2O Studied using XPS and XAES. *Surf. Interface Anal.* **1996**, 24, 811-820.

(35) Cochran, S. J.; Larkins, F. P., *J. Chem. Soc. Faraday T. 1: Phys. Chem. Cond. Phases* **1985,** *81*, 2179-2190.

(36) Roberts, M. W.; Smart, R. S. C., *J. Chem. Soc. Faraday T. 1: Phys. Chem. Cond. Phases* **1984,** *80*, 2957-2968.

(37) Négrier, F.; Marceau, E.; Che, M.; Giraudon, J.-M.; Gengembre, L.; Löfberg, A., *Catal. Lett.* **2008,** *124*, 18-23.

(38) Stach, J.; Pekarek, V.; Grabic, R.; Lojkasek, M.; Pacakova, V. Dechlorination of Polychlorinated Biphenyls, Dibenzo-P-Dioxins and Dibenzofurans on Fly Ash. *Chemosphere* **2000**, *41*, 1881–1887.

(39) Stach, J.; Pekarek, V.; Endrst, R.; Hetflejs, J. Dechlorination of Hexachlorobenzene on MWI Fly Ash. *Chemosphere* **2003**, *39*, 2391–2399.

(40) Weber, R.; Nagai, K.; Nishino, J.; Shiraishi, H.; Ishida, M.; Taksuga, T.; Konndo, K.; Hiraoka, M. Effects of Selected Metal Oxides on the Dechlorination and Destruction of PCDD and PCDF. *Chemosphere* **2002**, *46*, 1247–1253.

Chapter 5
Summary and Future Studies

5.1 Summary

The goals of our studies were to gain a better understanding of the hypothesized mechanism of EPFR formation and how it may be better refined with different metal oxides. In order to achieve our goals we examined the atomistic and electronic structure of EPFR precursors on metal oxide nanoparticles and single crystals, studied the interactions between EPFR precursors and metal oxides as a function of temperature and crystallographic face, and examined surrogate nanoparticle reactivity and 3D structure using chlorinated EPFR precursors. Our studies can also be used to develop possible future remediation strategies of these toxic pollutants.

All of our studies focused on two metal oxides in particular: Cu(II)O and ZnO. Cu(II)O is very active in forming EPFRs, while ZnO produces the longest lived EPFRs according to previous EPR results [1, 2]. To obtain the silica supported Cu(II)O nanoparticles of varying sizes, the incipient wetness impregnation method was used. The nanoparticle sizes were controlled by varying the percent by weight (% wt.) of Cu(II)O. The sizes of the nanoparticles were measured using TEM. The sizes ranged from ~1.5 - 6.5 nm which is roughly the same as the Cu(II)O nanoparticles prepared by dendrimeric methods [3]. ZnO single crystals of different crystallographic faces were also used as a model system. Specifically, the non-polar (10$\underline{1}$0), polar (0001)-O, and polar (000$\underline{1}$)-Zn surfaces were examined.

One aspect our studies involved chemisorbing phenol to single crystal surfaces of ZnO including the (10$\underline{1}$0), (0001)-O, and (000$\underline{1}$)-Zn surfaces at room temperature and 220 °C. This was to mimic a key step in the EPFR formation process. ZnO is interesting since it produces the longest live EPFRs with half-lives up to 73 days as observed by EPR experiments [1]. The interactions between phenol and ZnO are also interesting because Zn only has two stable oxidation states with the +1 state non-existent. Additionally, ZnO single crystals only have a few stable crystallographic faces [3]. Therefore, this is an ideal model system to obtain comprehensive information that closely represents nanoparticle powder samples, which have been used in previous studies. In this study we used UPS and EELS to examine the electronic structure of phenol chemisorbed to ZnO and LEED to examine the ordering of phenol on the surface.

The UPS data showed significant shifts to lower binding energy on the (10$\underline{1}$0) and (000$\underline{1}$)-Zn. This was a direct observation of band bending toward the Fermi level. The observation of band bending (to lower binding energies) is direct evidence of charge transfer away from the ZnO to the phenol [4]. This differs from previous investigations of EPFR precursors on metal oxides such as TiO_2, which observed charge transfer to the metal oxide [5]. This also differs with the EPFR formation mechanism previously described. Very little shifts were observed for the (0001)-O. The UPS difference spectra also showed that the phenol chemisorbed to (10$\underline{1}$0) likely remained intact. A comparison with a calculation of a single phenol molecule at approximately 2.5 eV supported this observation.

The Zn and O terminated surfaces were significantly different from the calculation. The data suggests that either occupied states are being depopulated or degeneracy is being added to the phenol on both surfaces.

The EELS data of the (10$\underline{1}$0) and the (000$\underline{1}$)-Zn surfaces corroborates largely with the UPS data. The EELS data showed little differences between the (10$\underline{1}$0) and physisorbed “phenol ice”. The spectral features were the same just shifted to lower excitation energies. The (000$\underline{1}$)-Zn, however, shifted significantly to lower loss energy by 0.7 eV and a transition between the HOMO to conduction band minimum was observed. This has been observed with other aromatics on ZnO [6]. The EELS and UPS measurements support the observation that the phenyl ring of chemisorbed phenol remains intact on the (10$\underline{1}$0) surface, but the Zn terminated surface may be more conductive to EPFR formation. If EPFR formation does favor the Zn terminated surface, this finding may have implications on the nanoparticle studies of EFPRs on ZnO. Namely, the nanoparticles maybe Zn terminated since EPFRs are observed on the nanoparticles.

LEED data also showed significant differences between the non-polar and polar surfaces. Namely, that phenol forms a semi-ordered c(2x2) superstructure along the (0001) direction on the (10$\underline{1}$0) surface. The LEED also showed that full saturation of the (10$\underline{1}$0) surface by phenol occurs at 0.5 ML. On the Zn terminated surface the ordering of phenol is completely disordered, which could have impacts on the electronic structure of the adsorbed phenol.

To examine the atomistic and electronic structure and interactions of the Cu(II)O nanoparticle formed EPFRs XANES was employed. The Cu(II)O nanoparticles were first heated to various temperatures to make sure that whatever happens to the Cu(II)O would be from the EPFR precursor and not by simple heating. The temperatures ranged from 60–400 °C. At room temperature the Cu started as expected in the +2 oxidation state. This is consistent with previously synthesized Cu(II)O nanoparticles prepared by other methods [7]. However, after heating to 260 °C the XANES spectra begin to shift further to lower energy. When the temperature reaches 300 °C, a peak associated with the 1s ➔ 4p transition begins to appear at 8982.6 eV which is indicative of Cu(I) formation [8, 9]. The peak increases in intensity as the temperature increases indicating that more Cu(I)O is forming. This could be due to adventitious carbon on the surface. After heating under vacuum this carbon reacts with oxygen to produce carbon monoxide and reduces the metal. This phenomenon has been observed with other metal oxides such as NiO and CoO and could explain our results [10-12]. With this in mind other experiments were performed to minimize this reduction. Therefore, 190 °C and 220 °C were selected based on the temperature results and other previous results from Dr. Dellinger's group that show maximum EPFR formation at those temperatures.

Other XANES measurements featured the Cu(II)O nanoparticles exposed to the EPFR precursor phenol for various time lengths (10 min. – 60 min.). The Cu(II)O was reduced to Cu(I)O which corroborates with the mechanism of EPFR formation. This also suggested that the Cu(II)O nanoparticles have interior Cu

atoms that are unavailable for reduction. However, the amount of reduction fluctuated between 0% - 30% Cu(I). This indicated a flaw in the experimental setup. Two possible reasons exist for such fluctuations. One is that since the samples had to be pressed onto a tungsten mesh this could have blocked active sites and not allowed the phenol to diffuse through the powder. The second reason may be that since a tungsten mesh was used, which is composed of several different wires, a heat gradient formed. This effectively could have caused some parts of the sample to reach a different temperature than another part of the sample. This would create adsorption on some parts and not others resulting in the fluctuations.

To probe the reactivity and 3D structure of the Cu(II)O nanoparticles, XRF measurements were employed. Chlorinated EPFR precursors were adsorbed to silica supported Cu(II)O nanoparticles under various conditions with the hope of measuring the Cl to Cu ratio. By doing this measurement we hoped to measure how many radicals formed per metal ion. This would in turn give information regarding the nature of the surface and if the nanoparticles were flat or had height with Cu unavailable for adsorption on the interior.

First, different precursors such as 1,2-dichlorobenzene (1,2-DCB), 1,4-dichlorobenzene (1,4-DCB), and pentachlorophenol (PCP) were adsorbed to the 2% wt. Cu(II)O surface at 230 °C. While a peak for Cu was visible, no peak for Cl was observed. The second XRF measurement was perform on Cu(II)O nanoparticles of vary sizes (1 wt. %, 2 wt. %, and 5 wt. %) exposed to PCP at 230 °C. Again no Cl was observed. Lastly, 2% wt. Cu(II)O nanoparticles were

dosed with PCP at 230 °C, 190 °C, and 150 °C. No Cl was observed at any temperature. Cu(II)O has been observed to be effective at dechlorinating organic compounds, which we were not aware of at the time of these studies [13-15]. Another possible explanation for the missing Cl is the sources for the measurements. Since the sources output high-energy particles this could cause dechlorination of the precursors. Since the Cl may not remain with the EPFR, this has significant impacts on other studies being performed with chlorinated EPFRs.

5.2 Future Studies

The results presented for both Cu(II)O and ZnO have opened new avenues for studying EPFR precursors adsorbed to metal oxides. Due to the resent instillation of a new multi-pole wiggler at CAMD XANES experiments were postponed. Now that CAMD is back to supplying reliable light more XANES experiments are being planned. Since XANES experiments showed drastic inconsistency, a new sample holder is being built for the *in-situ* chamber. This new sample holder consists of a single tantalum plate with a light bulb attached to the back. The light bulb is wrapped with tantalum foil to help heat the sample holder more effectively. With this new improvement multiple samples can be placed on the plate increasing efficiency of the experiments. Another advantage of the design is that samples can be heated in air. By doing this the nanoparticles can be reoxidized to the original oxidation state. This will allow studies to understand if the history of the nanoparticles affects EPFR formation.

With this new sample holder other experiments are to be performed such as EPFR precursors adsorbed to ZnO, Fe_2O_3, or NiO nanoparticles of varying sizes. Bimetallic nanoparticles can also be exposed to EPFR precursors to understand how EPFRs form in the presence of more than one metal.

The XRF measurements were indeed surprising. By not observing any Cl, this highlighted a gap in our understanding of adsorbing halogenated precursors on metal oxides. The question still remains if the measurements sources (x-ray/electrons) or the metal oxides themselves are responsible for dehalogenation. Three new experiments are currently being explored. One is to dose Cu(II)O nanoparticles with PCP and examine the system with temperature programmed desorption (TPD). TPD involves heating the dosed sample at a constant rate. A mass spectrometer is then used to measure the products that desorb from the sample surface. This will give information regarding the products that adsorbed to the sample surface. Not only can PCP be analyzed, but other chlorinated products can be observed and quantified which would give better insights into other reactions that maybe taking place. The second experiment is to use wet chemistry and perform an extraction with isobutanol or some other solvent followed by examination of the products with GC/MS. In principle the only chlorine that would be observed comes from the adsorbates on the nanoparticle surfaces. The GC/MS would allow a product distribution to be constructed. Like TPD not only would PCP be potentially observed, but other chlorinated products as well. The GC/MS would also allow us to quantify each product. This information will also allow us to examine possible side reactions that are taking

place involving the chlorine from PCP. The last experiment is to use our *in-situ* chamber at CAMD to dose nanoparticles with chlorinated precursors and examine them with XANES at the Cl edge. This would give us information regarding if Cl is present on the nanoparticles and in what form the Cl is in (either organic chloride or metal chloride). Each of the previously described experiments are not limited to Cu(II)O nanoparticles. Other metal oxide nanoparticles such as NiO and ZnO can and should be used to examine how they behave with chlorinated EPFR precursors. This part of the project has been handed to Dr. Matthew Patterson who will perform these studies.

Another study is underway by Dr. Matthew Patterson and others to synthesize metal oxide nanoparticles on atomically flat surfaces such as oxidized silicon. These studies are designed to further unite the nanoparticle work with the single crystal work. Nanoparticles such as Cu(II)O, Fe_2O_3, and NiO will be deposited on surfaces such as oxidized Si(111) and exposed to EPFR precursors. These samples can then be examined with surface science techniques such as EELS, UPS, and XPS. Not only are nanoparticles on flat surfaces being examined, but also other single crystal samples as well such as Fe_2O_3 that have extensively studied nanoparticle counterparts. Like ZnO we can use surface science techniques to examine the interactions and electronic structures of EPFR precursors adsorbed to metal oxides that would be difficult to obtain in other ways.

The ZnO single crystal work is also continuing. Dr. Randall Hall's group is performing computational studies to examine the orbitals that are participating when charge is transferred from the ZnO to the phenol. Dr. Hall's group is constructing small ZnO clusters (containing 4 to 5 Zn atoms) with phenol bonded to them and calculating the electronic structures using density functional theory (DFT). Using computational methods such as natural bond order analysis, charge transfers can be calculated and compared to our experimental results. Experimental studies regarding the oxygen-terminated surface are also being explored. The UPS data showed little charge transfer to the phenol and the difference spectrum showed one peak that matches with the phenol HOMO.

EELS studies will be performed to examine the low energy excitations and surface interactions that UPS can not measure. Finally, LEED will also be done to examine if any ordering takes place when phenol is chemisorbed to the surface.

5.3 References

(1) Vejerano, E.; Lomnicki, S.; Dellinger, B. Lifetime of Combustion-Generated Environmentally Persistent Free Radicals on Zn(II)O and Other Transition Metal Oxides. *J. Environ. Monit.* **2012**, *14*, 2803–2806.

(2) Kiruri, L. W.; Khachatryan, L.; Dellinger, B.; Lomnicki, S. Effect of Copper Oxide Concentration on the Formation and Persistency of Environmentally Persistent Free Radicals (EPFRs) in Particulates. *Environ. Sci. Technol.* **2014**, *48,* 2212–2217.

(3) Woll, C. The Chemistry and Physics of Zinc Oxide Surfaces. *Progress in Surface Science* **2007**, *82*, 55–120.

(4) Zhang, Z.; Yates, J. T., Jr. Band Bending in Semiconductors: Chemical and Physical Consequences at Surfaces and Interfaces. *Chem. Rev.* **2012**, *112*, 5520–5551.

(5) Patterson, M. C.; Thibodeaux, C. A.; Kizilkaya, O.; Kurtz, R. L.; Poliakoff, E. D.; Sprunger, P. T. Electronic Signatures of a Model Pollutant–Particle System: Chemisorbed Phenol on TiO_2(110). *Langmuir* **2015**, *31*, 3869–3875.

(6) Arnaud, G. F.; De Renzi, V.; del Pennino, U.; Biagi, R.; Corradini, V.; Calzolari, A.; Ruini, A.; Catellani, A. Nitrocatechol/ZnO Interface: the Role of Dipole in a Dye/Metal-Oxide Model System. *J. Phys. Chem. C* **2014**, *118*, 3910–3917.

(7) Lomnicki, S. M.; Wu, H.; Osborne, S. N.; Pruett, J. M.; McCarley, R. L.; Poliakoff, E.; Dellinger, B. Size-Selective Synthesis of Immobilized Copper Oxide Nanoclusters on Silica. *Mat. Sci. Eng. B* **2010**,175(2), 136–142.

(8) Kau, L.-S.; Spira-Solomon, D.; Penner-Hahn, J. E.; Hodgson, K. O.; Solomon, E. I. X-Ray Absorption Edge Determination of the Oxidation State and Coordination Number of Copper: Application to the Type 3 Site in *Rhus Vernicifera* Laccase and Its Reaction with Oxygen. *J. Am. Chem. Soc.* **1987**, *109*, 6433–6442.

(9) Gaur, A.; Shrivastava, B. D.; Joshi, S. K. Copper K-Edge XANES of Cu(I) and Cu(II) Oxide Mixtures. *J. Phys.: Conf. Ser.* **2009**, *190*, 012084.

(10) Cochran, S. J.; Larkins, F. P., *J. Chem. Soc. Faraday T. 1: Phys. Chem. Cond. Phases* **1985,** *81*, 2179-2190.

(11) Roberts, M. W.; Smart, R. S. C., *J. Chem. Soc. Faraday T. 1: Phys. Chem. Cond. Phases* **1984,** *80*, 2957-2968.

(12) Négrier, F.; Marceau, E.; Che, M.; Giraudon, J.-M.; Gengembre, L.; Löfberg, A., *Catal. Lett.* **2008,** *124*, 18-23.

(13) Stach, J.; Pekarek, V.; Grabic, R.; Lojkasek, M.; Pacakova, V. Dechlorination of Polychlorinated Biphenyls, Dibenzo-P-Dioxins and Dibenzofurans on Fly Ash. *Chemosphere* **2000**, *41*, 1881–1887.

(14) Stach, J.; Pekarek, V.; Endrst, R.; Hetflejs, J. Dechlorination of Hexachlorobenzene on MWI Fly Ash. *Chemosphere* **2003**, *39*, 2391–2399.

(15) Weber, R.; Nagai, K.; Nishino, J.; Shiraishi, H.; Ishida, M.; Taksuga, T.; Konndo, K.; Hiraoka, M. Effects of Selected Metal Oxides on the Dechlorination and Destruction of PCDD and PCDF. *Chemosphere* **2002**, *46*, 1247–1253.

Appendix: Statements of Permission

Chapter 3 has been submitted to Chemical Physics Letters published by Elsevier. This work is not yet published and is undergoing the review process. Elsevier gives reprinted permission per their Author's Rights document (http://www.elsevier.com/book-authors/science-and-technology-book-publishing/author-rights): "Authors can use either their accepted author manuscript or final published article for… inclusion in a thesis or dissertation"

Vitae

Chad Thibodeaux was born in Lake Charles, Louisiana. He received his Bachelor's of Science degree with a concentration in Biochemistry from McNeese State University. He entered Louisiana State University to pursue his Ph.D. in Chemistry in 2008 under the direction of Professor Erwin D. Poliakoff.